SCALE DEPENDENCE OF ROCK MASS DEFORMABILITY MEASURED BY FIBER-OPTIC STRAIN GAGES

By

JoAnn R. Gage

A dissertation submitted in partial fulfillment of

the requirements for the degree of

Doctor of Philosophy

(Geoscience)

at the

UNIVERSITY OF WISCONSIN – MADISON

2012

Date of final oral examination: 05/16/2012

The dissertation is approved by the following members of the Final Oral Committee:

Herbert F. Wang, Professor, Geoscience
Laurel B. Goodwin, Professor, Geoscience
Harold J. Tobin, Professor, Geoscience
David J. Hart, Affiliated Professor, Geoscience
Dante O. Fratta, Professor, Civil Engineering; Geological Engineering Program

UMI Abstract

We use fiber-optic strain and temperature sensors to measure *in situ* strain in rock masses to examine how the mechanical properties of rock vary from the cm^3 to m^3-scale. We have installed a dense array of Fiber Bragg Grating (FBG) sensors underground on the 1250 m (4100 ft.) level of the Sanford Underground Research Facility (SURF) Lead, SD. We use this sensor array in two loading experiments to determine the modulus of deformation (E_m) of the rock mass.

We have developed three sensor attachment methods. We use 1 m gage-length OS3600 temperature-compensated FBG strain gages that were installed in two ways: surface-mounted and embedded. Ambient temperature changes in the mine bias strain measurements from the surface-mounted sensors. Because of the temperature effects on the surface-mounted sensors, embedded sensors are preferable for measuring *in situ* strain in rock masses.

In order to measure a more detailed strain and temperature profile within a rock mass, we have developed Fiber-optically Instrumented Rock Strain and Temperature Strips (FROSTS). FROSTS are embedded in the rock mass and have six fiber-optic strain and temperature gages installed along specially designed strips of 304-stainless steel. We have also developed a pretensioning method for the FROSTS so that the FROSTS can measure both shortening and elongation. Our laboratory experiments show that the FROSTS accurately measure strain, are more compliant than the rock mass, and thoroughly couple to the rock mass.

We performed two field point-loading tests using 89 kN and 890 kN loads and the fiber-optic strain sensors array to evaluate *in situ* rock mass deformability and examine how the mechanical properties of rock vary over spatial scales. The *in situ* modulus of deformation

increases with depth into the rock mass. We interpret this increase in stiffness to be a result of the differences in mechanical properties due to the effect of excavation of the underground space. If done properly, *in situ* measurements of rock stiffness are a valuable tool to fully characterize the gradient in stiffness of a rock mass, which single point measurements, such as laboratory tests or geotechnical classification systems, do not fully capture.

Abstract

We use fiber-optic strain and temperature sensors to measure *in situ* strain in rock masses to examine how the mechanical properties of rock vary from the cm^3 to m^3-scale. We have installed a dense array of Fiber Bragg Grating (FBG) sensors underground in the Poorman formation on the 1250 m (4100 ft.) level of the Sanford Underground Research Facility (SURF), at the site of the former Homestake gold mine in Lead, SD. We utilize this sensor array in two loading experiments to determine the modulus of deformation (E_m) of the rock mass.

Because fiber-optic sensors have not previously been implemented underground, we have developed several sensor attachment methods for rock masses. We use 1 m gage-length OS3600 temperature-compensated FBG strain sensors built by Micron Optics Inc. that were installed in two ways: surface-mounted and embedded. Ambient temperature changes in the mine bias strain measurements from the surface-mounted sensors. For our sensors located on the 1250 m (4100 ft.) level in SURF, there is no mechanical strain recorded above the resolution of our sensors. Because of the temperature effects on the surface-mounted sensors, embedded sensors are preferable for measuring *in situ* strain in rock masses.

In order to measure a more detailed strain and temperature profile within an intact rock mass, we have developed Fiber-optically Instrumented Rock Strain and Temperature Strips (FROSTS). FROSTS are embedded in the rock mass and have six fiber-optic strain and temperature gages installed at 30 cm intervals along specially designed strips of 304-stainless steel. FROSTS are modified Rock Strain Strips (ROSS), developed by Signer and Sunderman (2003). We have also developed a pretensioning method for the FROSTS so that the FROSTS can measure both shortening and elongation within the rock mass. Our laboratory experiments

show that the FROSTS accurately measure strain, are more compliant than the rock mass they are embedded into, and thoroughly couple to the rock mass. FROSTS provide an accurate and detailed record of *in situ* strain and temperature in intact rock masses and are useful for the structural health monitoring of underground spaces.

We performed two field point-loading tests using 10 ton (89 kN) and 100 ton (890 kN) loads and the fiber-optic strain sensors array to evaluate *in situ* rock mass deformability of the Poorman formation and examine how the mechanical properties of rock vary over spatial scales. The *in situ* modulus of deformation increases with depth into the rock mass. We interpret this increase in stiffness to be a result of the differences in mechanical properties due to the effect of excavation of the underground space. Near the surface (0 – 1.2 m depth), the rock is weakened due to damage from blasting; beyond the damaged zone is the stress-relief zone (1.2 – 1.5 m depth) where open joint sets affect rock stiffness, and in the undisturbed zone (>1.5 m depth), the rock is the stiffest. If done properly, *in situ* measurements of rock stiffness are a valuable tool to fully characterize the gradient in stiffness of a rock mass, which single point measurements, such as laboratory tests or geotechnical classification systems, do not fully capture.

Acknowledgments

First and foremost, I wish to thank Herb for taking me on as a PhD student. Thanks for giving me the freedom to pursue my interests while keeping me focused. Thank you for your mentoring and support. Words really are not enough to show how grateful I am for this opportunity.

I also wish to thank the other members of my committee: Laurel Goodwin, Dante Fratta, Dave Hart, and Harold Tobin. I am lucky to have such a supportive committee where each individual has had an impact on my research and development as a scientist.

I am extremely fortunate to have worked work a wonderful, generous, and diverse group of scientists as collaborators on this project. I could not have done this project without the support of Alan Turner from Micron Optics Inc., Steve Gabriel, from Spearfish High School, Mary MacLaughlin from Montana Tech, and Neal Lord from UW-Madison. I am also grateful for everyone who assisted us on our numerous underground trips including Rich Barry, Branko Glisic, Matt Kogle, Noni, and Kevin Hachmeister.

I also with to thank the scientists and staff at the South Dakota Science and Technology Authority that facilitated our underground trips and helped keep us safe while we performed our work, especially: Jaret Heise, Tom Trancynger, Wendy Zawada, Connie Giroux, Pat Kinghorn, Luke Scott, Fritz, and Mike Oates.

I am grateful for the numerous funding sources that supported my research including: NSF grant CMMI-0900351, the Morgridge fellowship from the UW-Madison Department of Geoscience, ConocoPhillips, ExxonMobil, and the American Philosophical Society.

The number of graduate students, both current and past, that have helped me along the way and made my time in Wisconsin enjoyable are too numerous to name, but know that I appreciate your friendship and support! I also want to thank the departmental staff, especially Michelle, Shirley, Jane, Judy, Brian, Mary, and Jansi.

Finally, completing my degree would not have been possible without my parents, family, and husband. Thank you for your love and support and believing in me when I did not think I could finish.

Table of Contents

List of Figures and Tables

Chapter 4

Chapter 1: Introduction

On all scales, from the structure and strength of the lithosphere (Bürgmann and Dresen, 2008) to earthquake mechanics (Lockner and Beeler, 2002), slope stability for landslide hazards (Günther and Thiel, 2009), and the safety of underground spaces (Obert et al., 1960) the mechanical properties of rocks are integral to many important processes that occur within the earth. Thus, it is important to understand and predict the mechanical properties of large volumes of intact rock. Typically, rock properties are measured on the cm^3-scale in laboratory experiments and extrapolated to larger scales (e.g. Hoek and Brown, 1980). However, the results of laboratory mechanical tests typically cannot be used to accurately predict the behavior of an intact rock mass. Small (cm^3) laboratory samples cannot capture the effect of structural heterogeneities, such as joints and fractures, on the mechanical behavior of a larger-scale rock mass (Hu and Huang, 1993; Scott et al. 1998).

On the m^3-scale, geoscientists and geological engineers commonly perform *in situ* deformation experiments or utilize geotechnical classification systems (e.g. Rock Mass Rating from Bieniawski (1973) or Geological Strength Index from Hoek and Brown (1997) to estimate the mechanical properties of a rock mass. *In situ* measurements are costly, time-consuming, and have been shown to provide unreliable results (Bieniawski, 1978; Hoek and Diederichs, 2006). Similarly, geotechnical classifications and empirical approaches for estimating rock stiffness do not fully characterize the properties of a rock mass. My research utilizes fiber-optic strain gages in an embedded multipoint borehole extensometer with a refined *in situ* testing procedure to examine how the mechanical properties of rock vary from

the cm^3 to the m^3-scale. My experiments produce accurate deformability results that characterize how and why the stiffness varies within an intact rock mass.

On the m^3-scale, artificially induced fractures from blasting or hydraulic fracturing create a zone of damaged rock around the deformation source (Palmström and Singh, 2001; Hoek et al., 2002). However, it is difficult to quantify the extent of the damaged zone and how the mechanical properties of the rock are affected by the deformation (Hoek and Diederichs, 2006). This damaged zone has important implications for ground control and mine safety (Signer et al., 1997) and can be exploited in groundwater and petroleum reservoirs. Hydraulic fracturing is used to stimulate groundwater flow and low-permeability hydrocarbon reservoirs (Banks et al., 1996). For both applications, the spatial extent of the induced fracture network is not well understood (King, 2010). Additionally, the blasting and hydraulic fracturing modify the stiffness of the intact rock mass (Palmström and Singh, 2001), which can have important implications for the production and long-term stability of the reservoir rock (Hettema et al., 2000). On a regional scale, induced fractures around large underground openings, such as mines, can significantly modify the hydrogeology of an area on the km^3-scale (Murdoch et al., 2012). My research provides one of the first quantitative analyses of the extent of a damaged zone around an underground excavation and examines the effect of blasting on the stiffness of an intact rock mass.

Fiber-optic strain and temperature sensors are an emerging technology that has been used successfully for structural health monitoring in civil engineering applications (Rao, 1999; Glisic and Inaudi, 2007). These sensors have the potential to be powerful monitoring tools for increasing the safety and longevity of underground spaces. Although this potential

has been recognized (Yang et al., 2008; Matsui et al., 2009), fiber-optic strain gages and temperature sensors have not been extensively implemented for structural health monitoring underground. One major obstacle in the implementation of fiber-optic sensors in geotechnical applications is attachment methods. It is critical that the fiber-optic sensors are coupled to the rock mass to accurately measure deformation. However, all current installation methods are optimized for civil applications (e.g. adhering to the surface of a structure or embedding into concrete) and not installation in an intact rock mass to measure *in situ* strain at depth.

My sensor installations and field experiments were done on the 1250 m (4100 ft.) level of the Sanford Underground Research Facility (SURF), located at the site of the former Homestake gold mine in Lead, SD. SURF is an underground laboratory that will house physics neutrino and dark matter experiments, as well as provide some space for underground biology, geology, and engineering research (Kramer, 2011).

In chapter 2, I use "off-the-shelf" fiber-optic strain and temperature sensors and design installation methods for attaching Fiber Bragg Grating (FBG) strain gages to an intact rock mass. These gages are 1 m gage-length temperature compensated FBG sensors. I use two installation methods: 1) surface-mounted and 2) embedded (Gage et al., 2010). Each installation technique proved problematic for measuring small-magnitude *in situ* strains. Strain recorded by the surface-mounted sensors is biased by ambient temperature changes within the mine. These temperature swings swamp the strain signal on the surface-mounted sensors. I developed a data analysis method to isolate the mechanical strain and remove these unwanted temperature effects; however the ambient temperature effects could not fully be removed because the mechanical strain in the system is so small. The embedded sensors do

not experience this temperature effect; however the 1 m gage-length proved too long to measure the magnitude of rock deformation of interest.

In chapter 3, I develop a new method for monitoring real-time *in situ* strain and temperature in rock masses. Fiber-optically Instrumented Rock Strain and Temperature Strips (FROSTS), improve on the Rock Strain Strip (ROSS) design of Signer and Sunderman (2003). ROSS are ~2 m (6 ft.) long strips of stainless steel that are cut into a specific design to control the compliancy of the strip and anchor it to the rock mass. My development of Signer and Sunderman's ROSS design involves using fiber-optic strain and temperature gages, instead of electrical resistance strain gages, to produce a slimmer design, simplify data collection, improve longevity of the monitoring device, and provide a detailed temperature profile with depth in the rock mass. The temperature profile is useful for determining the thermal properties of the rock mass. Additionally, I developed a method to pretension the FROSTS prior to installation, so that the strips can measure both shortening and elongation (Gage et al., 2011). The previous ROSS design can only measure elongation (Signer and Sunderman, 2003).

In chapter 4, I utilize the OS3600 FBG array (Gage et al., 2010) and the FROSTS (Gage et al., 2011) installed on the 1250 m (4100 ft.) level of SURF to measure the modulus of deformation of an intact rock mass. I performed two point-loading tests that are analogous to plate-jacking tests (Palmström and Singh, 2001), except using a point load, instead of a disturbed load. I use the stress at each FROSTS sensor from 10 ton (89 kN) and 100 ton (890 kN) experiments and the recorded strains to determine the modulus of deformation (E_m) along a depth profile in the rock mass. I also determine the Young's modulus from laboratory

testing and the E_m from the Geological Strength Index (GSI) geotechnical classification system (Hoek and Brown, 1997) calculated for a series of disturbance factors (D) (Hoek et al., 2002; Hoek and Diederichs, 2006). By comparing the *in situ* E_m measurement, the laboratory Young's modulus, and the empirical Em calculations, I have shown how the stiffness of a rock mass increases with depth and correlated that gradient with the effects of excavation of an underground opening. This stiffness gradient shows that no single measurement, either *in situ*, lab, or empirical is sufficient to characterize the behavior of an intact rock mass, and is an example of how the mechanical properties of a m^3-scale rock mass changes over spatial scales.

References

D. Banks, Odling, N.E., Skarphagen, H., and Rohr-Torp, E. (1996) Permeability and stress in crystalline rocks. *Terra Nova*. 8: 223–235.

Bieniawski, Z.T. (1973) Engineering Classification of rock masses. *Transactions of the Society of African Institute for Civil Engineers*. 15: 335-344.

Bieniawski, Z.T. (1978) Determining rock mass deformability: Experience from case histories. *International Journal of Rock Mechanics, Mining Sciences, & Geomechanics Abstracts*. 15: 237-247.

Bürgmann, R. and Dresen, G. (2009) Rheology of the lower crust and upper mantle: Evidence from rock mechanics, geodesy, and field observations. *The Annual Reviews in Earth and Planetary Sciences.* 36: 531-567.

Gage, J.R., Noni, N., Turner, A., MacLaughlin, M., and Wang, H.F. (2010) Fiber optic strain and temperature monitoring in crystalline rock at the Sanford Underground Science and Engineering Laboratory (SUSEL), Lead, South Dakota, *44th U. S. Rock Mechanics Symposium and 5th U.S- Canadian Rock Mechanics Symposium*, *Salt Lake City, 27 – 30 June.* 8 pp.

Gage, J.R., Wang, H.F., MacLaughlin, M., Turner, A., and Fratta, D. (2011) A new method for measuring in situ strain in intact rock masses: Fiber optically instrumented rock strain and temperature strips (FROSTS). *45th US Rock Mechanics Symposium, San Francisco, CA June 26-29*. 10 pp.

Günther, A. and Thiel, C. (2009) Combined rock slope stability and shallow landslide susceptibility assessment of the Jasmund cliff area (Rügen Island, Germany). *Natural Hazards and Earth Systems Sciences*. 9: 687-698.

Glisic, B. and Inaudi, D. (2007) *Fibre Optic Methods for Structural Health Monitoring.* 1st ed. Sussex: Chinchester. 276 pp.

Hettema, M.H.H., Schutjens, P.M.T.M, Verboom, B.J.M., and Gussinklo, H.J. (2000) Production-induced compaction of a sandstone reservoir: the strong influence of stress path. *SPE Reservoir Evaluation Engineering*. 3: 342–7.

Hoek, E. and Brown, E.T. (1980) Empirical strength criterion for rock masses. *Journal of the Geotechnical Engineering Division ASCE*. 106 (GT9): 1013-1035.

Hoek, E. and Brown, E.T. (1997) Practical estimates of rock mass strength. *International Journal of Rock Mechanics & Mining Sciences*. 34: 1165-1186.

Hoek, E., Caranza-Torres, C.T., and Corcum, B. (2002) Hoek–Brown failure criterion- 2002 edition. *In: Bawden HRW, Curran J, Telsenicki M (eds) Proceedings of the North American Rock Mechanics Society (NARMS-TAC 2002). Mining Innovation and Technology, Toronto*. 267–273.

Hoek, E. and Diederichs, M.S. (2006) Empirical Estimation of rock mass modulus. *International Journal of Rock Mechanics & Mining Sciences*. 43: 203-215.

Hu, K.X. and Huang, Y. (1993) Estimation of the elastic properties of fractures rock masses. *International Journal of Rock Mechanics, Mining Sciences, & Geomechanics Abstracts*. 30: 381-394.

King, G.E. (2010) Thirty years of gas shale fracturing: What have we learned? *SPE Annual Technical Conference and Exhibition, 19-22 September Florence, Italy*. 50 pp.

Lockner, D.A. and Beeler, N.M. (2002) Rock failure and Earthquakes. *International Handbook of Earthquake and Engineering Seismology.* 81A: 505-537.

Murdoch, L.C., Germanovich, L.N., Wang, H., Onstott, T.C., Elsworth, D., Stetler, L., and Boutt, D. (2012) Hydrogeology of the vicinity of Homestake mine, South Dakota, USA. *Hydrogeology Journal*. 20: 27-43.

Matsui, H., Kashiwai, Y., Sano, O., Tokunaga, T., He, Z., Mogi, K., and Wang, H.F. (2009) Evaluation of the applicability of optical fiber strain sensors for monitoring rock deformation caused by ocean tide – A case study at the Aburatsubo site, Japan. *EOS Trans. AGU. 2009;* 90:Abstract H23E-1010.

Obert, L., Duvall, W.I., and Merrill, R.H. (1960) Design of underground openings in competent rock. *United States Department of the Interior Bureau of Mines Bulletin*. 587: 1-40.

Palmström, A. and Singh, R. (2001) The deformation modulus of rock masses – comparisons between in situ tests and indirect measurements. *Tunneling and Underground Space Technology*. 16: 115-131.

Rao, Y.J. (1999) Recent progress in applications of in-fibre Bragg grating sensors. *Optics and Lasers in Engineering*. 31: 297-324.

Signer, S.P., Cox, D., and Johnston, J. (1997) A method for the selection of rock support based on bolt loading measurements. *16th Conference on Ground control in mining. Morgantown*:183-190.

Scott, D.F., Girard, J.M., Williams, T.J., and Denton, D.K. (1998) Comparison of seismic tomography, strain relief, and ultrasonic velocity measurements to evaluate stress in an underground pillar. *NIOSH*. 7 pp.

Yang, Y., Annamdas, V.G.M., Wang, C., and Zhou, Y. (2008) Application of multiplexed FBG and PZT impedance sensors for health monitoring of rocks. *Sensors*. 8: 271- 289.

Chapter 2: Fiber-optic strain and temperature monitoring in crystalline rock at the Sanford Underground Research Facility (SURF), Lead, South Dakota

J. R. Gage, N. Noni, A. Turner, M. L. MacLaughlin, H. F. Wang

Published as: Gage, J.R., Noni, N., Turner, A., MacLaughlin, M., and Wang, H.F. (2010) Fiber optic strain and temperature monitoring in crystalline rock at the Sanford Underground Science and Engineering Laboratory (SUSEL), Lead, South Dakota, *44th U. S. Rock Mechanics Symposium and 5th U.S- Canadian Rock Mechanics Symposium*, *Salt Lake City, 27 – 30 June.* 8 pp.

ABSTRACT

We are monitoring temperature and rock deformation at the 1250 m (4100 ft.) level of the Sanford Underground Research Facility (SURF) in Lead, SD. In July 2009, we installed six 1 m gage-length Micron Optics Inc. OS3600 temperature compensated Fiber Bragg Grating (FBG) strain gages. The sensors were installed in two ways: surface-mounted and embedded. Strain and temperature data have been collected continuously at one-minute intervals since October 1, 2009. Strain data from sensors mounted on the rock surface correlate with changes in air temperature within the mine. In order to isolate the mechanical strain signal, we use a least squares linear thermal expansion analysis to fit the temperature and strain data. The least squares analysis is a reasonable first-pass method for separating the thermal effects from mechanical strain. For temperatures below ~35.5 ºC there is a good linear fit between strain and temperature, which produces a coefficient of thermal expansion of ~16 x 10^{-6}/ºC. The residual of the least squares analysis should represent the mechanical strain. For our sensors located on the 1250 m (4100 ft.) level in SURF, there is no mechanical strain recorded above the resolution of our sensors.

2.1 INTRODUCTION

Reliable structural health monitoring is essential for safe operation of civil infrastructure systems. Fiber-optic strain and temperature sensors have gained popularity in civil engineering for structural health monitoring of bridges, highways, dams, and buildings (Zhang et al., 2006; Glisic and Inaudi, 2007). They are recognized as a relatively inexpensive, lightweight, versatile, and long-lasting way to monitor structures (Rao, 1999). The primary advantages of fiber-optic sensors are their accuracy, sensitivity, and suitability for long-term monitoring (Kincade, 2006). Fiber-optic sensors also have great geotechnical monitoring potential for the safety and stability of mines, tunnels, and caverns (Matsui et al., 2009). Although this potential has been recognized (Yang et al., 2008), the sensors have not been extensively implemented underground.

We have installed six Micron Optics Inc. OS3600 Fiber Bragg Grating (FBG) strain sensors at the 1250 m (4100 ft.) level in the Sanford Underground Research Facility (SURF), which is located at the site of the former Homestake gold mine in Lead, SD. SURF is an underground laboratory that will house physics experiments as well as provide some space for underground biology, geology, and engineering research. SURF is being constructed by the Department of Energy (DOE) and the South Dakota Science and Technology Authority (SDSTA) (Kramer, 2011). Monitoring of the rock surrounding laboratory spaces is critical for the safety and longevity of SURF. Homestake mine had a history of rock movement due to mining activities (Pariseau et al., 1995a; Pariseau et al., 1995b; Girard et al., 1997), and fiber-optic strain gages could be an excellent tool for monitoring potential future rock movement.

This paper presents our strain and temperature data from six OS3600 FBG sensors installed 1250 m underground at SURF. Our goal is to measure the long-term rock response to mechanical deformation. Most of the strain recorded by our sensors is a result of changes in air temperature within the mine. We present a least square analysis of the data to isolate the air temperature effect and separate strain due to thermal expansion and contraction of the rock mass and mechanical strain.

2.2 GEOLOGY

The former Homestake gold mine is located in the northern Black Hills of South Dakota (Fig. 2.1). The area of the Homestake gold mine was subjected to several periods of deformation during the Precambrian Trans-Hudson orogeny resulting in complex fold patterns and localized shear zones (Dahl et al., 1999). Fluid influx during Precambrian deformation and metamorphism produced economic gold deposits along the structures (Nabelek, 1992). Uplift during the Laramide orogeny caused brittle deformation in the area of the Lead Window (Lisenbee and DeWitt, 1993) and created several joint sets obliquely orientated to our sensors, which are located in the Precambrian Poorman formation. The Poorman formation consists of metamorphosed tholeiitic basalt and metasedimentary rocks, which include the metamorphosed equivalents of dolomite, carbonate-rich claystone, siltstone, marl, and interbedded tuffs (Harder and Noble, 1948). In the area of our sensors the Poorman formation consists of a strongly foliated and lineated amphibolite-grade mica schist.

2.3 FIBER-OPTIC SENSOR INSTALLATION

In July 2009, we installed six Micron Optics Inc. OS3600 Fiber Bragg Grating (FBG) temperature compensated strain sensors. FBG sensors are wavelength dependent fiber-optic

sensors that consist of a 7 μm diameter cylindrical glass filament core contained in a protective cladding. A refractive grating is written into the core of the fiber. Broad-spectrum light is transmitted down the fiber from an optical laser interrogation box. The grating will reflect a wavelength of light corresponding to its Bragg wavelength, and all other light will be transmitted down the fiber (Fig. 2.2) (Hasse, 2007). Strain and temperature introduce a change in the spacing of the grating, which results in a shift of the Bragg wavelength. This change in the reflected wavelength of light from the FBG sensor directly corresponds to changes in strain or temperature.

The Micron Optic Inc. OS3600 gages have a sensitivity of 1 μstrain and a thermal resolution of 0.1 °C. The gages consist of a Fiber Bragg Grating (FBG) sensor housed in a 1 m long Teflon tube (Fig. 2.3). The FBG is attached to a steel anchor at each end of the sensor. The gages measure one-dimensional shortening and elongation between the anchor points at the ends of the sensor. Each sensor also contains a temperature compensation gage mounted on a metal tab at one end inside the Teflon tube. Because FBG gages are sensitive to both temperature and mechanical strain, this temperature compensation gage is used to subtract thermal effects from the total strain in order to isolate the strain due to movement of the rock mass (i.e. the mechanical strain).

Because FBG sensors have not been extensively used for the monitoring of intact rock masses, there are not established installation methods to ensure that the gage measures rock movement and not surface or attachment method effects. Micron Optics provides several accessories for sensor attachment, but the accessories are intended for civil engineering applications, such as surface adhesion (e.g. for bridges and buildings) or embedding into

concrete that can be poured around them. Underground strain measurements are only useful if they measure the movement within the rock mass. Therefore, we designed and implemented two different methods for installing OS3600 FBG gages in intact rock.

We installed the FBG sensors in two ways: 1) surface-mounted and 2) embedded. The two ends of each surface-mounted sensor sit in steel u-shaped brackets welded to the heads of rock bolts (Fig. 2.3). The rock bolts (DYWIDAGs) were drilled approximately two meters deep into the rock mass and secured in place with resin epoxy. Although the sensor sits above the surface of the rock, we expect that the rock bolts extend deep enough into the rock to measure strain within the rock mass and not just at the surface.

The embedded sensors are grouted into the rock mass. The sensors were placed into approximately 2 m deep holes drilled 10-15º down-dip and reamed to a 6.25 cm diameter. The embedded sensors have a manufacturer-supplied 5 cm diameter disk-shaped bracket on each end to help the sensor grip the rock (Fig. 2.3). Once the sensor was in place, the drill hole was filled with non-shrinking grout. The grout was mixed to a watery consistency and poured into the drill hole to surround the sensor and fill the borehole to the rock surface.

The six FBG sensors were installed in two sets of three approximately perpendicular gages (triplets) mounted on two perpendicular walls of an alcove measuring 2 m deep by 3 m wide and 2 m high. For simplicity, the triplets are called array A and array B. The triplets consist of two mutually perpendicular surface-mounted sensors and one sensor embedded sub-perpendicular to the surface of the rock (Fig. 2.4). The surface-mounted sensors measure the vertical and one horizontal direction of strain and the embedded sensor measures a third, nearly horizontal, strain direction. In addition to the six OS3600 strain gages, we installed an

OS4300 temperature gage on the surface of the Array B wall to measure the air temperature in the mine for comparison to the temperature compensation gages within the OS3600 gages. In October 2009, we installed a Micron Optics sm130 laser interrogation box controlled by an sp130 industrial computer mounted in an environmental box located in an instrument room about 10 meters from the sensor arrays. Data are recorded continuously at one-minute intervals. The Micron Optics Enlight software allows us to access and control the data acquisition over the internet using SURF's virtual private network (vpn).

2.4 RESULTS

2.4.1 Strain and temperature data

From the geometry of our sensor arrays, each triplet has one FBG gage parallel to one of the three Cartesian directions. Thus, for each direction there are two correlative gages, one from each triplet array (Fig. 2.3; 2.4). The Array A vertical gage and the Array B vertical gage both measure strain in the vertical direction. Similarly, the Array A horizontal sensor and the Array B embedded sensor measure strain in northwest-southeast direction, and the Array A embedded sensor and the Array B horizontal sensor measure strain in the northeast-southwest direction. For all strain data, elongation is positive and shortening is negative.

Because the OS3600 FBG sensors both measure and are affected by temperature, we must separate the thermal effects out of the raw strain data before we can examine mechanical strain in the rock mass. The raw strain data are obtained from the change in Bragg wavelength of the FBG mounted on the steel rod between the anchors of the sensor. Raw strain is calculated by:

$$\varepsilon_{raw} = (\Delta WL/WL0) / F_g \quad (2.1)$$

Where ε_{raw} is the raw strain and ΔWL is the change in the Bragg Wavelength. WL_0 and F_G are the reference wavelength and the gage factor respectively. Strain calculated using equation 2.1, without any thermal correction, is referred to as the uncorrected strain.

The uncorrected strain values of the two vertically oriented sensors are similar for the entire record (Fig. 2.5a). Uncorrected strain in the vertical sensors is nearly equal in both magnitude and direction. The two surface-mounted vertical sensors also show rapid, short-lived spikes in uncorrected strain that directly correlate to rapid changes in air temperature in the drift of the mine (Fig. 2.5a).

The correlative pairs of embedded and horizontal surface-mounted sensors measure strain in the northwest-southeast and the northeast-southwest directions. For the surface-mounted horizontal sensors, there are rapid and short-lived spikes in uncorrected strain that correlate with changes in air temperature at the rock surface (Fig. 2.5b & c). Similar to the two surface-mounted vertical sensors, the surface-mounted horizontal sensors are highly sensitive to changes in air temperature.

The embedded sensors, however, do not show the same correlation between uncorrected strain and rapid changes in air temperature. However, during sustained temperature anomalies (e.g. Fig. 2.5b; November 6 to December 20, 2009) the uncorrected strain recorded in the embedded sensors does respond to the temperature change, but the response is not immediate. The response of the embedded strain sensor lags behind the surface sensor and has a longer decay time (Fig. 2.5b). Additionally, the uncorrected strain recorded by the embedded sensor has a smaller amplitude than the surface-mounted sensors.

2.4.2 Data analysis

In order to examine mechanical strain in the rock mass, we must first compensate for the temperature effects in the uncorrected strain data. The sensor manufacturer provides an empirical method to remove the thermal effects from the mechanical strain (Micron Optics, 2010). However, because there is very little mechanical strain measured by our sensors, the recommended method did not satisfactorily remove the temperature effect. Thus, we attempted to devise a better method.

The uncorrected strain from the four surface-mounted sensors, visually appears to correlate directly to changes in air temperature in the mine (Fig. 2.5). To determine if there is any mechanical strain signal, we use a least squares linear analysis to compare the correlation between temperature and uncorrected strain in the surface-mounted sensors. This analysis is based on a conceptual model of linear elastic thermal expansion of the rock/gage system (i.e. the epoxy, the rebar that the surface-mounted sensors are welded to, the Teflon tube surrounding the fiber, and the glass filament of the fiber-optic wire).

For each of the four surface-mounted sensors we fit a least squares line to the strain data using the air temperature measurement and compute the residual strain. For all four sensors this simple linear analysis produces a reasonable fit (Fig. 2.6). At temperatures below ~35.5 ºC the best-fit line is a good approximation of the uncorrected strain and temperature data. Above 35.5 ºC, the slope of the fit for the data shallows dramatically for all four surface-mounted sensors.

With elastic thermal expansion, the slope of the line represents an approximation of the coefficient of thermal expansion for the rock and sensor system. For three of the four

surface-mounted sensors, the modeled coefficient of thermal expansion is within the range of 15 – 17 x 10^{-6}/ºC (Fig. 2.6). For the Array A horizontal sensor the coefficient of thermal expansion is 8.27 x 10^{-6}/ºC, which is significantly lower than the other three surface-mounted sensors.

Assuming a linear thermal expansion model, the residual of this analysis represents the mechanical strain in the rock mass with the effects of ambient temperature change on the surface-mounted gages removed. When the residual is compared to the embedded sensor (Fig. 2.7), it resembles the shape of uncorrected strain curve from the embedded sensor. The amplitude of the residual is significantly smaller than the uncorrected data for the sensor and the embedded sensor. Also, some, but not all, rapid and short-lived spikes in uncorrected strain are removed.

2.5 DISCUSSION

2.5.1 Temperature effects on surface-mounted FBG sensors

The correlation of uncorrected strain in the surface-mounted gages with the air temperature record suggests that the strain signal in the surface-mounted sensors is dominated by ambient temperature change in the mine and is not primarily a result of mechanical strain. However, the least squares analysis shows that the sensors are measuring some actual thermal expansion of the rock and not just responding to surface air temperature.

The estimated coefficient of thermal expansion of ~16 x 10^{-6}/ºC is reasonable for both steel (the rebar material) and a mica-rich rock. The Poorman Formation at the sensor site is a mica schist with a well-developed foliation. The coefficient of thermal expansion for mica perpendicular to cleavage is 15 – 25 x 10^{-6}/ºC in the range of 20 – 100 ºC (Holland and

Powell, 1998). The coefficient of thermal expansion for steel is 11 - 13 x 10^{-6}/ºC at 20 ºC (DeHoff, 2006). Because the surface-mounted sensors are welded to rock bolts, the coefficient of thermal expansion approximated by the least squares method measures linear thermal expansion for the rock/gage system. The estimated coefficient of thermal expansion of ~16 x 10^{-6}/ºC is within the range for both mica and steel, the main components of the rock/gage system.

At temperatures above ~35.5 ºC, the linear relationship between temperature and uncorrected strain breaks down for all four surface-mounted sensors (Fig. 2.6). Temperatures above 36 ºC occur primarily as rapid and short-lived temperature spikes (Fig. 2.5a). We interpret the change in slope of the linear analysis above ~35.5 ºC to represent the response of the sensors in the air and not any response from the rock or the mounting system. This instantaneous response to surface temperature change is too rapid to be thermal expansion of the rock and sensor system because the thermal diffusivity of the system is too low (Hanley et al., 1978). Thus, the instantaneous increase in uncorrected strain at high temperature suggests that the sensor housing in which the FBG gage is contained is bending between the fixed ends of the sensors as it thermally expands and creating strain in the system. This strain is neither the thermal expansion of the rock, nor mechanical strain, and is what we wish to filter out of the data set.

A second explanation for the change the linear relationship between temperature and uncorrected strain over ~35.5 °C is the thermal expansion of Teflon. The FBG strain sensor of the OS3600 is contained in a Teflon tube. The coefficient of thermal expansion of Teflon has two significant, non-linear increases between 20 – 35 °C due to first-order phase transitions in

the polymer (Kirby, 1956). The change in the uncorrected strain – temperature relationship at temperatures above 35 °C, could be a result of the nonlinear behavior of the coefficient of thermal expansion of Teflon. The empirically determined coefficients of thermal expansion for the rock/gage system, determined above, take into account all the elements of the sensor attachment method including the Teflon tube. It is possible that a significant change in the coefficient of thermal expansion of even one element in the system could affect the uncorrected strain – temperature relationship.

2.5.2 Thermal and mechanical strain

Because the embedded sensors are installed approximately 1.5 m deep into the rock mass, they are not exposed to the rapid air temperature changes and thus do not show any large spikes in strain correlative with temperature change. The embedded sensors are not affected by the surface air temperature changes; thus, in future FBG installations, embedded sensors are deemed preferable to any surface-mounted FBG attachment method.

The embedded sensors measure strain due to the thermal expansion of the rock. For periods of time when there is a sustained increase in surface temperature of two weeks or longer the strain in the embedded sensors also changes in response to the changing temperature gradient and thermal expansion in the rock. For example, in response to an increase in temperature beginning November 6, 2009 (Fig. 2.5b), the strain in the surface sensor decreased instantaneously with the temperature change. Strain in the embedded sensor also decreased, but did so over a longer time period. This delayed strain response appears to represent thermal diffusion through the rock. The rock mass surrounding the embedded

sensors essentially acted as a low pass filter for the changes in surface temperature, and the sensors record the thermal strain in the rock due to thermal expansion and contraction.

The residual computed for the surface-mounted sensors after the linear analysis can be interpreted as the strain remaining after the removal of the thermal effects. Thus, the residual represents a simple first-order look at the mechanical strain in the system. There are some long wavelength increases and decreases in strain throughout the recorded time period (Fig. 2.7c), however these changes are very small in magnitude (<10 με). Although there is active construction on the 1748 m (4850 ft.) level within SURF, the lack of recorded mechanical strain indicates that the sensors installation is too far from the source to measure any meaningful deformation. Over longer periods of time, deformation due to mine-wide dewatering may produce measurable mechanical strain.

Although the FBG sensors installed underground on the 1250 m (4100 ft.) level of SURF do not record any significant mechanical deformation, they are recording useful data. The sensors are sensitive enough to measure strain due to the thermal expansion of the rock mass. The data are also internally consistent. The three sets of correlative sensors (Array A vertical – Array B vertical; Array A horizontal – Array B embedded; Array B horizontal – Array A embedded) are measuring strain with similar magnitudes and the same directions for the entire length of the record.

2.6 CONCLUSIONS

1) Linear regression analysis between the uncorrected strain of surface-mounted gages and air temperature produces a method for separating thermal effects from the mechanical strain.

2) The coefficient of thermal expansion of the rock/gage system is ~16 x 10^{-6}/ºC, which is reasonable for the rock/gage system we have installed.

3) Fiber-optic FBG sensors produce internally consistent data and are useful for monitoring strain and temperature in intact rock.

4) Because of the temperature effects on the surface-mounted FBG sensors, embedded sensors are preferable for measuring *in situ* strain in intact rock masses.

2.7 ACKNOWLEDGMENTS

The work was supported by National Science Foundation Grants to Wang (CMMI-0900351) and MacLaughlin (CMMI-0821788) and funding from the American Philosophical Society and ConocoPhillips to Gage. The authors wish to thank the Sanford Underground Research Facility, especially Jaret Heise, Tom Trancynger, and Connie Giroux, for logistical support throughout the project.

References

Dahl, P.S., Holm, D.K., Gardner, E.T., Hubacher, F.A., and Foland, K.A. New constraints on the timing of Early Proterozoic tectonism in the Black Hills (South Dakota), with implications for docking of the Wyoming Province with Laurentia. *Geology.* 111: 1335-1349.

DeHoff, R. (2006) *Thermodynamics in Materials Science.* 2nd ed. Boca Raton: Taylor & Francis.

Girard, J.M., McKibbin, R.W., Seymour, J.B., and Jones, F.M. (1997) Characterization of in situ stress conditions at depth – Homestake mine, Lead, South Dakota. *International Journal of Rock Mechanics & Mining Sci*ences. 34: Paper No. 104.

Glisic, B. and Inaudi, D. (2007) *Fibre Optic Methods for Structural Health Monitoring.* 1st ed. Sussex: Chinchester.

Hanley, E.J., DeWitt, D.P., and Roy, R.F. (1978) The thermal diffusivity of eight well-characterized rocks for the temperature range 300-1000K. *Engineering Geoogy.*. 12: 31-47.

Harder, J.A. and Noble, J.O. (1948) Stratigraphy and metamorphism in a part of the northern Black Hills and the Homestake mine, Lead, South Dakota. *Geological Society of America Bulletin.* 59: 941-976.

Hasse, K. (2007) Strain sensors based on Bragg gratings. *In: IMEKO 20th TC3, 3rd TC16 and 1st TC22 International Conference Cultivating metrological knowledge, 27 – 30 November, 2007.*

Holland, T.J.B. and Powell, R. (1998) An internally consistent thermodynamic data set for phases of petrological interest. *J. Metamorphic Geology.* 16: 309-343.

Kincade, K. (2006) Optoelectric applications: Fiberoptic sensing – Fiber sensors lay groundwork for structural health monitoring. *Laser Focus World*. 42.

Kirby, R.K. (1956) Thermal expansion of Polytetrafluoroethylene (Teflon) from -190° to +300 °C. *Research of the National Bureau of Standards*. 57; 91-94.

Kramer D. (2011) Funding for NSF underground laboratory is rejected. *Physics Today*. 21.

Lisenbee, A.L. and DeWitt, E. (1993) Laramide evolution of the Black Hills Uplift. *Geological Survey of Wyoming Memoir.*

Matsui, H., Kashiwai, Y., Sano, O., Tokunaga, T., He, Z., Mogi, K., and Wang, H.F. (2009) Evaluation of the applicability of optical fiber strain sensors for monitoring rock deformation caused by ocean tide – A case study at the Aburatsubo site, Japan. *EOS Trans. AGU.* 90: Fall Meet. Suppl., Abstract H23E-1010.

Micron Optics Inc. (2010) Optical Fiber Sensors Guide: Fundamentals & applications. http://www.micronoptics.com/uploads/library/documents/Micron%20Optics%20Optical%20Sensing%20Guide.pdf. Accessed February 19, 2012.

Nabelek, P.I., Sirbescu, M., and Liu, M. (1999) Petrogenesis and tectonic context of the Harney Peak Granite, Black Hills, South Dakota. *Rocky Mountain Geololgy*. 34: 165-181.

Pariseau, W.G., Johnson, J.C., McDonald, M.M., and Poad, M.E. (1995a) Rock mechanics study of shaft stability and pillar mining, Homestake Mine, Lead, SD: 1. Premining geomechanical modeling using UTAH2. *United States Department of the Interior Report of Investigations.* RI 9531: 1-20.

Pariseau, W.G., Johnson, J.C., McDonald, M.M., and Poad, M.E. (1995b) Rock mechanics study of shaft stability and pillar mining, Homestake Mine, Lead, SD: 2. Mine measurements and confirmation of premining results. *United States Department of the Interior Report of Investigations.* RI 9576: 1-13.

Rao Y.J. (1999) Recent progress in applications of in-fibre Bragg grating sensors. *Optics and Lasers in Eng.* 31:297-324.

Yang, Y., Annamdas, V.G.M., Wang, C., and Zhou, Y. (2008) Application of multiplexed FBG and PZT impedance sensors for health monitoring of rocks. *Sensors*. 8: 271- 289.

Zhang, W., Gao J., Shi, B. Cui, H., and Zhu, H. (2006) Health monitoring of rehabilitated concrete bridges using distributed optical fiber sensing. *Computer Aided Civil and Infrastructure Engineering.* 21: 411-424.

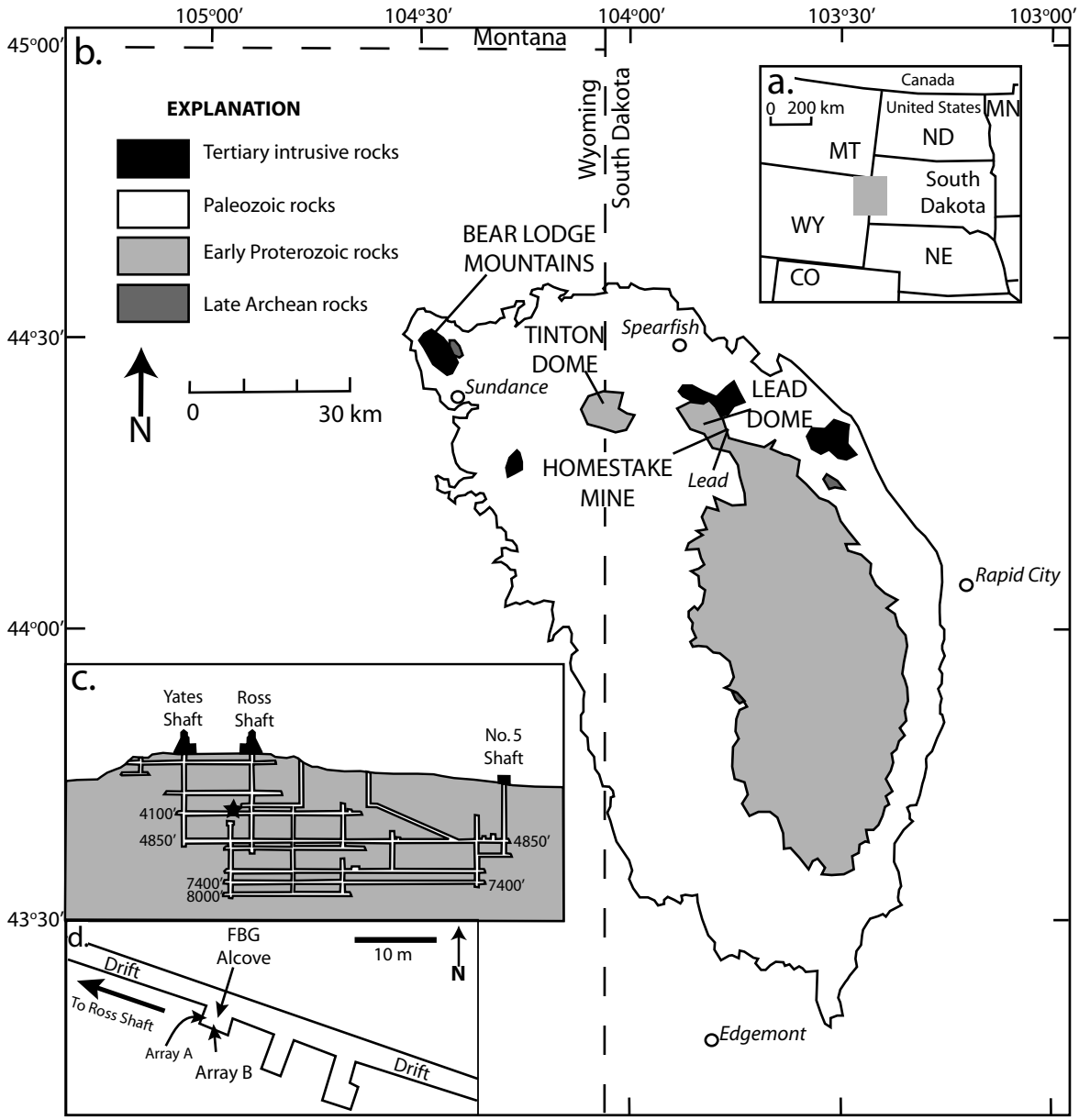

Figure 2.1. Location of SURF in Lead, South Dakota. a.) Gray box shows location of the Black Hills; b.) Simplified geologic map of the Black Hills Uplift. The Homestake gold mine is located in the Lead Dome of the northern Black Hills. Modified from Pariseau (1995b); c.) Schematic cross section of SURF showing major science levels. Black star denotes approximate experiment location; d.) Map view of experiment alcove on the 1250 m (4100 ft.) level. Array A and Array B denote the two FBG sensor arrays.

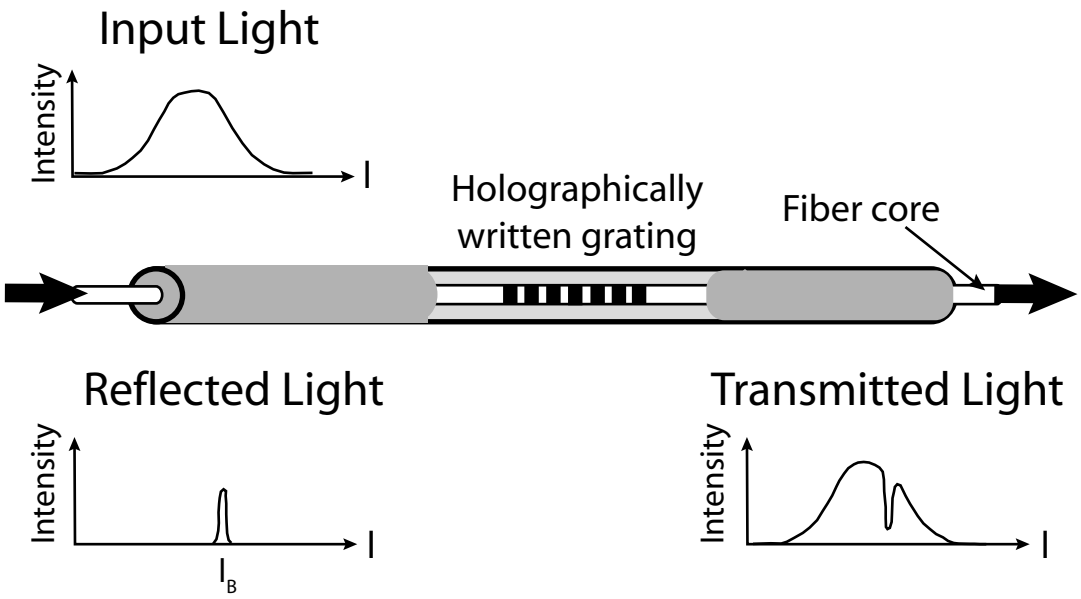

Figure 2.2. Diagram of a Fiber Bragg Grating with input, reflected, and transmitted light spectra. Light with the wavelength of the Bragg grating (I_B) is reflected. The Bragg wavelength changes with strain and temperature. After Hasse (2007).

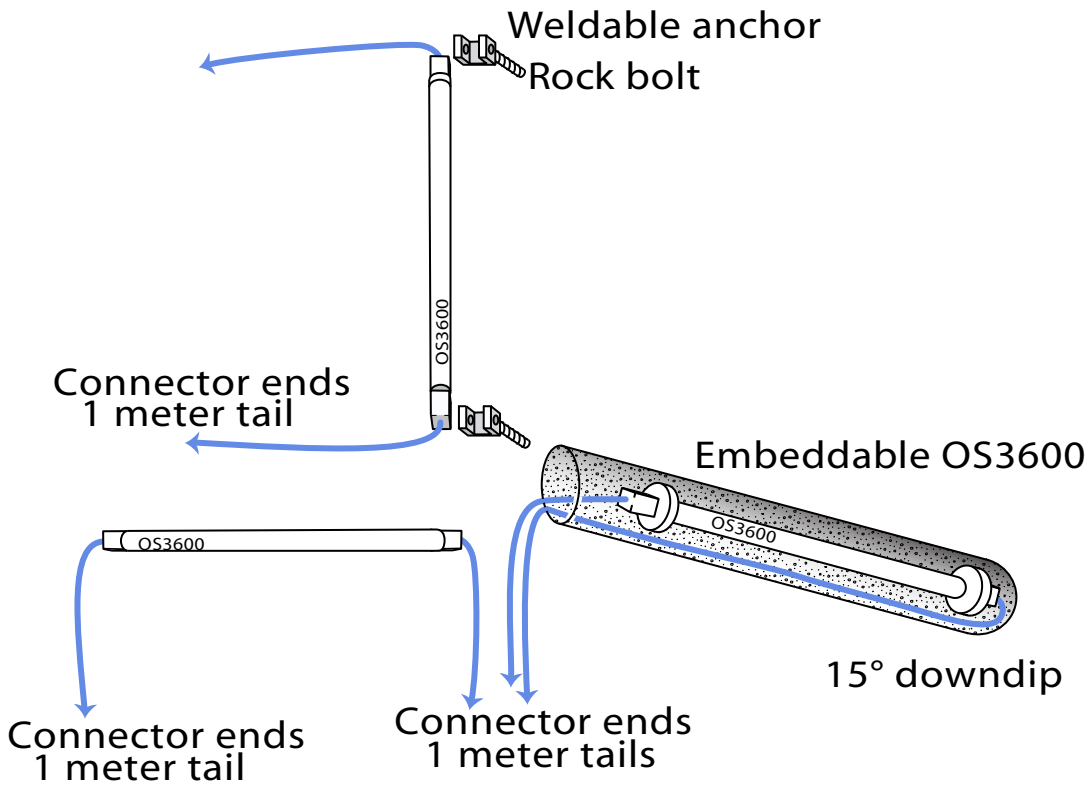

Figure 2.3. Drawing of OS3600 FBG triplet configuration. The two surface-mounted gages are oriented vertically and horizontally. Their anchors sit in metal u-shaped brackets welded to the heads of two rock bolts. The embedded sensor is grouted into a hole drilled 10-15° downdip. The embedded sensors have 5-cm diameter metal disks on each end.

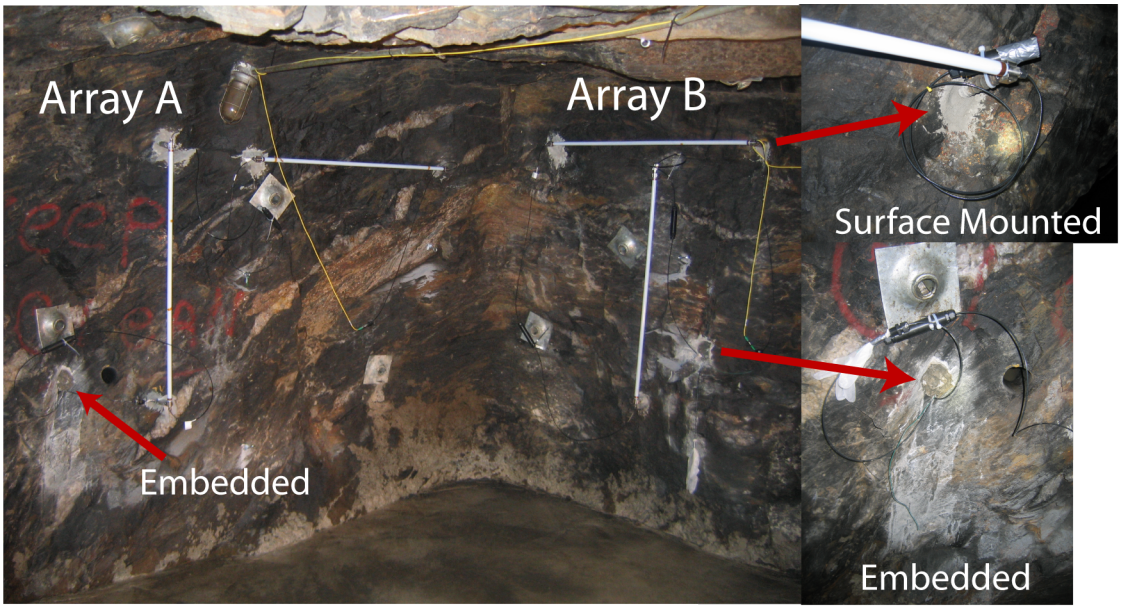

Figure 2.4. Photographs of installed OS3600 gages. Photograph showing the perpendicularly oriented surface-mounted sensors of the two arrays (left). Holes filled with grout (denoted by arrows) show the location of the two embedded sensors. Photographs on right show close-up views of sensor mounting techniques. The ends of the surface-mounted sensors are welded to the heads of steel rock bolts epoxyed into the rock (top). Embedded sensors are place into a 6.25 cm diameter drillhole ~2 m deep and surrounded by grout (bottom).

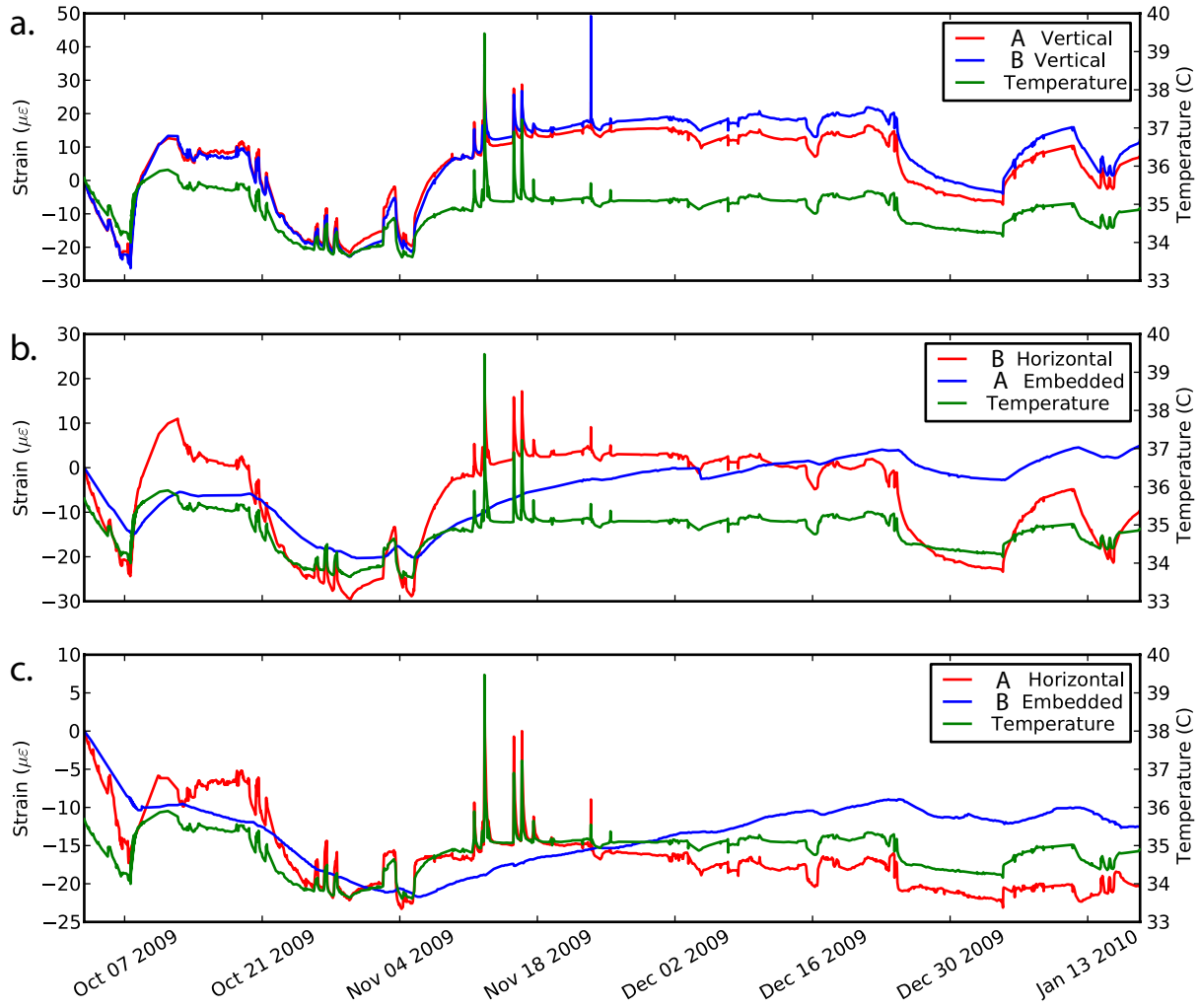

Figure 2.5. Plots showing uncorrected strain data for correlative sensors (red and blue curves) and surface temperature (green curves) results from October 1, 2009 through February 1, 2010; a.) Uncorrected strain data for the two vertical surface-mounted sensors and surface temperature; b.) Uncorrected strain data for the Array B horizontal surface-mounted sensor and the Array A embedded sensor with surface temperature; c.) Uncorrected strain data for the Array A horizontal surface-mounted sensor and the Array B embedded sensor with surface temperature.

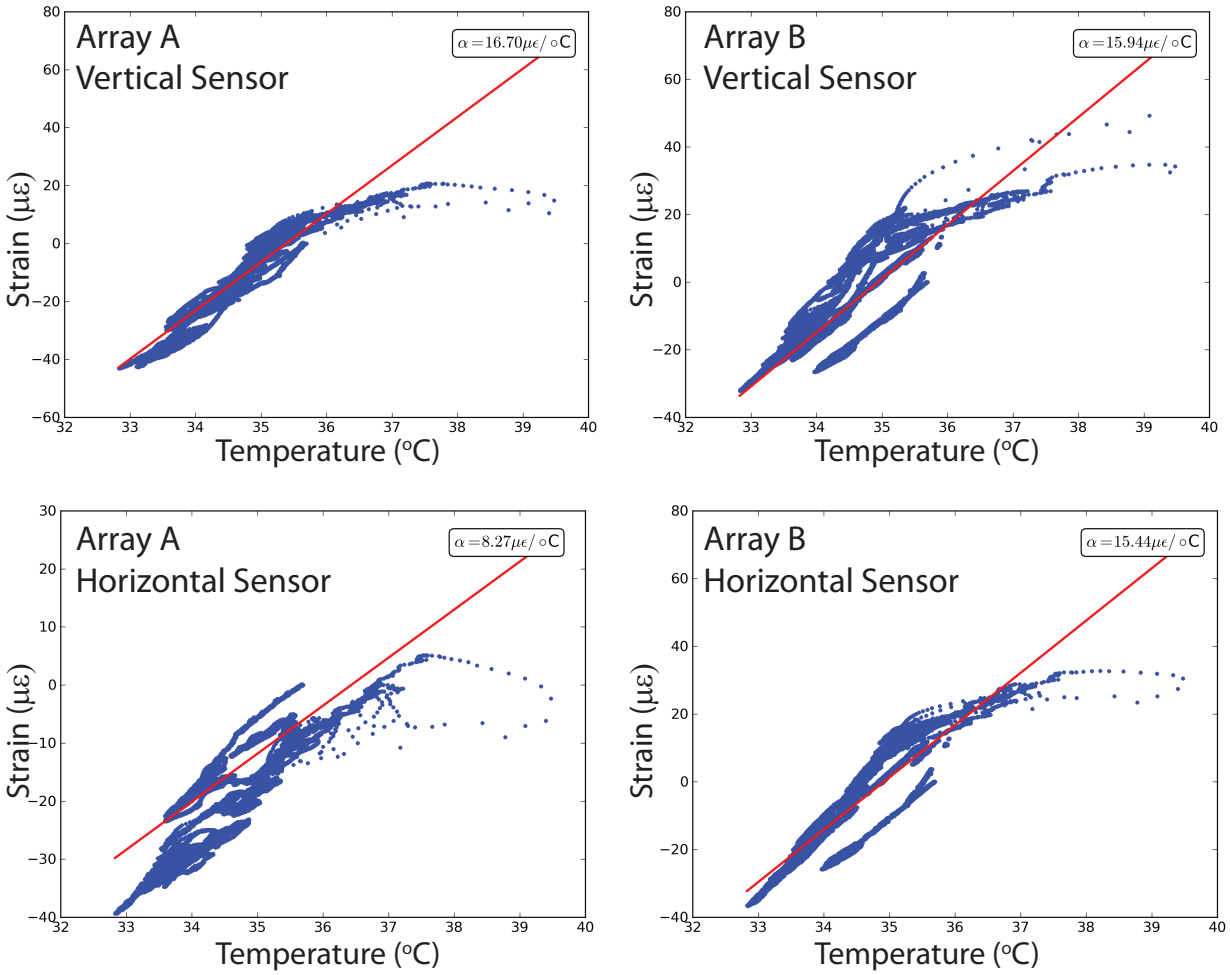

Figure 2.6. Results of the least squares linear thermal expansion analysis for the four surface-mounted sensors and surface temperature. Plots of strain versus temperature show the best-fit line. The slope of the line is an approximation of the coefficient of thermal expansion (α) of the rock/gage system.

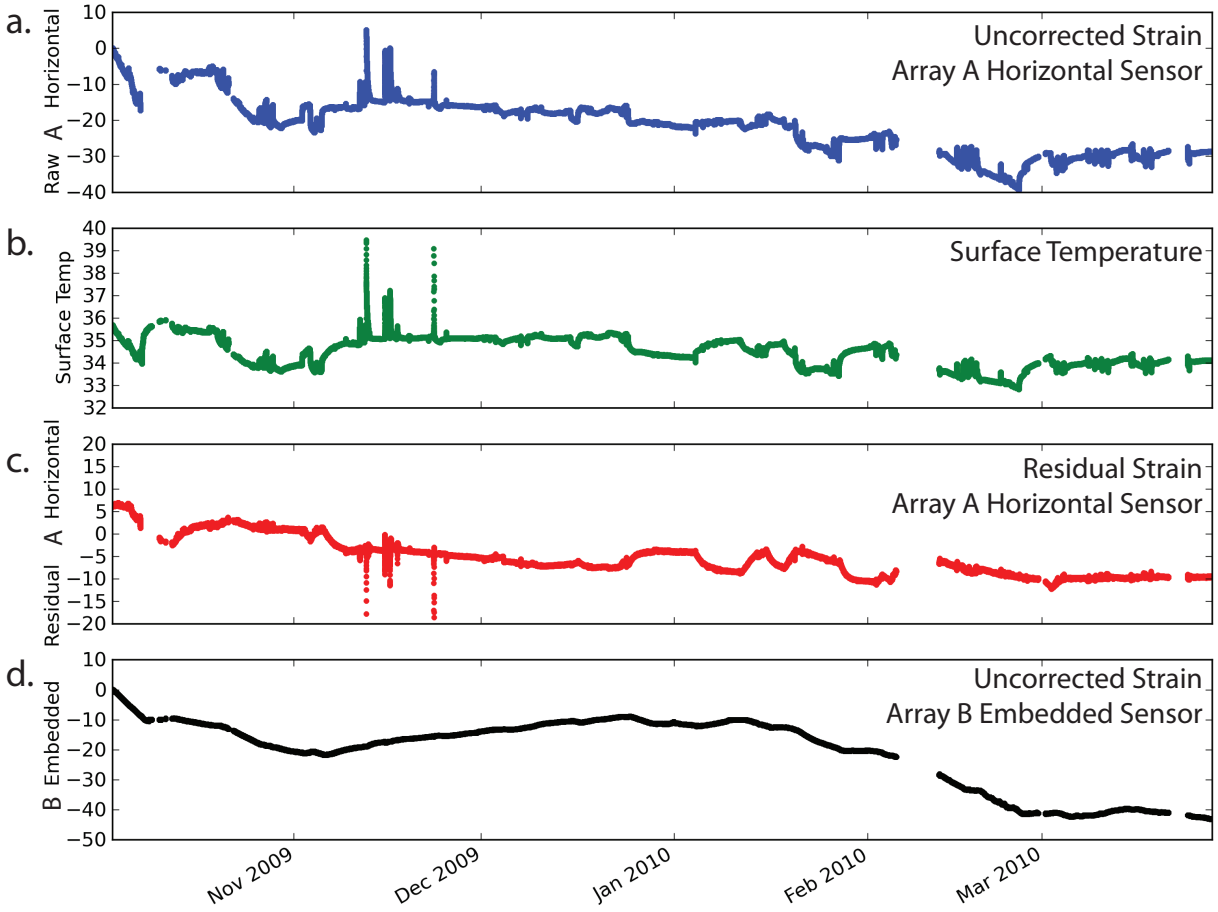

Figure 2.7. a.) Uncorrected strain data from the array A surface-mounted horizontal sensor used for least squares analysis; b.) Air temperature data used for least squares analysis; c.) Residual of the array A horizontal uncorrected strain after least squares analysis, which represents mechanical strain, or strain with all thermal effects due to air temperature change and thermal expansion removed; d.) Uncorrected strain data from the Array B embedded sensor for comparison to the residual. The residual and strain from the embedded sensor have similar shapes, but the residual strain is much smaller in magnitude.

Chapter 3: Fiber-optically Instrumented Rock Strain and Temperature Strips (FROSTS): Validation and implementation of a new method for monitoring *in situ* strain and temperature in intact rock masses

J. R. Gage, H. F. Wang, D. O. Fratta, A. Turner, M. L. MacLaughlin

Published in part as: Gage, J.R., Wang, H.F., MacLaughlin, M., Turner, A., and Fratta, D. (2011) A new method for measuring in situ strain in intact rock masses: Fiber optically instrumented rock strain and temperature strips (FROSTS). *45th US Rock Mechanics Symposium, San Francisco, CA June 26-29*. 10 pp.

ABSTRACT

Fiber-optically instrumented rock strain and temperature strips (FROSTS) are a new method for monitoring *in situ* strain and temperature in intact rock masses. FROSTS are an alternative to other techniques such as borehole extensometers or instrumented rock bolts for monitoring strain around underground openings. FROSTS have six fiber-optic strain and temperature gages installed at 30 cm intervals along specially designed strips of 304-stainless steel and are embedded into the rock mass. FROSTS are modified Rock Strain Strips (ROSS), developed by Signer and Sunderman (2003). If pretensioned prior to installation, the FROSTS can measure both shortening and elongation. Two FROSTS were pretensioned and installed on the 4100 level (~1250 m below the surface) of the Sanford Underground Research Facility (SURF) in Lead, SD. Data from the initial monitoring of these FROSTS record strain in the rock mass due to the closure of microcracks and fractures created during drilling for installation and then stabilization of the FROSTS sensors. The fiber-optic temperature sensors

on the FROSTS also record a detailed thermal gradient of increasing temperature with depth into the rock mass. Laboratory experiments show that the FROSTS accurately measure strain, are more compliant than the rock mass they are embedded into, and thoroughly couple to the rock mass to ensure accurate readings. FROSTS provide an accurate and detailed record of *in situ* strain and temperature in rock masses and are useful for the structural health monitoring of underground spaces.

3.1 INTRODUCTION

Structural health monitoring of underground openings is critical for the safety and longevity of these spaces. Statistics from the Mine Safety and Health Administration (MSHA) indicate that rock falls are one of the major hazards in underground mines. From 2007 through 2011, 37% of all underground mining fatalities were caused by rock falls (MHSA, 2011). Tunnels, mines, and underground repositories require a long-term monitoring program to detect changes in strain in the surrounding rock mass that might be a precursor for instability or collapse (Bhalla et al., 2005). Continuous real-time monitoring provides the most robust data to detect instabilities and mitigate fall hazards.

All of the tools currently used for the deformation monitoring of underground openings have significant drawbacks. Convergence monitoring is limited by intermittent campaign-style readings as well as low accuracy, typically 0.1 mm (Milner, 1969). Additionally, both convergence measurements and surface-mounted extensometers only monitor changes at the surface of the excavation, which may not be representative of important strain changes within the rock mass (Franklin, 1977).

Embedded monitoring tools, such as borehole extensometers, provide measurements at depth in the rock mass. Multiple rod extensometers are quite accurate and provide detailed data with up to 10-20 points per hole, however, the size of the borehole increases with the number of rods (Burland et al., 1972). Larger boreholes will affect the ability of the extensometer to accurately measure movement in the rock (Franklin, 1977). Multiple wire extensometers can be installed in smaller boreholes than multiple rod extensometers, but are less accurate due to difficulties in reproducing tension levels in the wires and creep and kinking in the wires (Hedley, 1969; Whittaker and Hodgkinson, 1970). Strain measurements from both multiple rod and multiple wire borehole extensometers are typically taken periodically and manually; however, electric transducers can be installed at the heads of the extensometers to facilitate continuous automatic monitoring (Franklin, 1977).

Instrumented rock bolts are also used for strain monitoring in mines. For ground control purposes, rock bolts require a minimum amount of load on the bolt, but the bolt and rock mass will fail when the load exceeds the tensile strength of the bolt (Winsor, 1997). The load on the rock bolt can be monitored by sensors at the head of the rock bolt (Boyle, 1995) or with strain gages along the length of the bolt (Serbousek and Signer, 1985; Johnston and Cox, 1993; Maleki et al., 1994). However, the rock bolt is generally much stiffer than the surrounding rock mass, which leads to slip in the grout between the bolt and the rock (Farmer, 1975) and inaccurate measurement of strain in the rock mass due to the stiffness contrast between the rock and the bolt (Littlejohn, 1993; Boyle, 1995; Signer and Sunderman, 2003).

Signer and Sunderman (2003) developed a new method for measuring *in situ* strain in intact rock masses. Rock Strain Strips (ROSS) are thin strips of 304-stainless steel in a

specific design that are instrumented with strain gages and grouted into a borehole (Signer and Sunderman, 2003). The ROSS are more compliant than the rock mass and their design allows for more detailed strain measurements than instrumented rock bolts (Signer and Sunderman, 2003).

We have enhanced the original ROSS design and developed Fiber-optically Instrumented Rock Strain and Temperature Strips (FROSTS). FROSTS are instrumented with both strain and temperature gages and use fiber-optic technology to measure deformation in the rock mass. We have also developed a method to pretension the FROSTS prior to installation to measure a broader range of strain than is possible with the ROSS. The main advantages of FROSTS over the traditional ROSS are: 1) FROSTS can measure both shortening and elongation; 2) They provide a detailed temperature profile with depth into the rock mass; 3) The fiber-optic gages have longer-term stability and require many fewer leads than electrical-resistance gages; and 4) FROSTS have stream-lined data collection and recording in the field.

Fiber-optic strain and temperature sensors have great potential for the structural health monitoring of underground openings. Fiber-optic sensors have gained popularity in civil engineering for structural health monitoring of bridges, highways, dams, and buildings (Rao, 1999; Zhang et al., 2006). They are recognized as a relatively inexpensive, lightweight, versatile, and long-lasting way to monitor structures (Glisic and Inaudi, 2007). The primary advantages of fiber-optic sensors are their accuracy, sensitivity, and suitability for long-term monitoring (Kincade, 2006). Fiber-optic sensors also have great geotechnical monitoring potential for the safety and stability of mines, tunnels, and caverns (Matsui et al., 2009).

Although this potential has been recognized, the sensors have not been extensively implemented underground.

One major obstacle in the implementation of fiber-optic sensors for geotechnical applications is attachment methods. It is critical that the fiber-optic sensors are coupled to the rock mass to accurately measure deformation. Previous studies have shown that embedded fiber-optic sensors are preferable to installing the gages at the surface due to the effects of temperature change at the rock surface on the sensors (Matsui et al., 2009; Gage et al., 2010). In our research, FROSTS have become the preferred method for installing fiber-optic strain and temperature gages for monitoring deformation in intact rock masses (Gage et al., 2011b).

This paper discusses our methodology for the construction and installation of FROSTS. We also provide field validation of the FROSTS monitoring tool with the installation and data analysis from two FROSTS installed on the 4100 level of the Sanford Underground Research Facility (SURF) in Lead, SD. We also present laboratory data that validates the switch from electrical-resistance gages to fiber-optic gages on the FROSTS, as well as our pretensioning and installation methods.

3.2 FIBER BRAGG GRATING (FBG) SENSORS

FBG sensors are wavelength dependent fiber-optic sensors that consist of a 7 μm diameter cylindrical glass filament core surrounded by a protective cladding. A diffraction grating corresponding to a specific Bragg wavelength is written into the core of the fiber. Broad-spectrum light is transmitted down the fiber from an optical laser interrogation box. The grating will reflect a wavelength of light corresponding to its Bragg wavelength, and all other light will be transmitted through the fiber (Fig. 3.1) (Hasse, 2007). Strain and

temperature changes introduce a corresponding change in the grating spacing of the fiber, which results in a shift of the Bragg wavelength (Hasse, 2007). The change in the reflected wavelength of light from the FBG sensor corresponds to changes in strain and temperature. Both the FBG strain and temperature sensors are constructed using the same fiber with inscribed diffraction granting. In FBG strain gages, the fiber is anchored at each end of the diffraction grating; allowing the fiber to respond to changes in both mechanical strain and temperature. In contrast, the fiber and diffraction grating within the FBG temperature sensors is not fixed at its endpoints, and thus records only to temperature change and not mechanical movement.

The change in wavelength of the reflected light is converted into strain using the following equation:

$$\varepsilon_{raw} = (\Delta WL/WL0) / F_g \tag{3.1}$$

where ε_{raw} is the raw strain and ΔWL is the change in the Bragg Wavelength. WL_0 and F_G are the reference wavelength and the gage factor respectively; both are manufacturer-supplied constants. Temperature change affects the shift in wavelength of the FBG stain sensors by inducing thermal strain in the fiber as well as changing the refractive index of the fiber. Thus, in order to examine mechanical strain it is necessary to apply a thermal correction to equation 1 (Micron Optics, 2010). The thermal strain is calculated as:

$$\varepsilon_{thermal} = \Delta T\ [(C_1/F_g) + CTE_S - C_2] \tag{3.2}$$

where the change in temperature (ΔT) is calculated from the change in the Bragg Wavelength of a spatially correlative FBG temperature sensor, C_1, C_2, and F_G are manufacturer supplied constants, and CTE_S is the coefficient of thermal expansion of the test specimen. The thermal output ($\varepsilon_{thermal}$) is subtracted from the raw strain (equation 1) to get the mechanical strain in the system (Micron Optics, 2010). Because FBG strain gages are affected by temperature, it is necessary to have temperature sensors adjacent to strain sensors in any FBG array.

3.3 STRAIN AND TEMEPRATURE STRIPS

3.3.1 Rock Strain Strips (ROSS)

Rock Strain Strips (ROSS) were developed by Signer and Sunderman (2003), as an alternative to instrumented rock bolts, to measure rock movement and the performance of roof supports in mines. The ROSS is cut from a thin (1.5 mm) sheet of 304-stainless steel. 304-stainless steel was chosen for its high ductility (~70%) so that the ROSS will not break prior to tensile failure of typical roof supports (Signer and Sunderman, 2003).

The shape of the ROSS is critical to its performance. Its shape is similar to that of a dog-bone consisting of narrow (1.27 cm wide) straight strips of metal between two sets of wider (3.18 cm wide) areas with teeth cut into the edges of the strip (Fig. 3.2). The ROSS is twisted 60° along each serrated section. The ROSS is 183 cm (6 ft.) long. The narrow, flat sections are 20 cm long and the wider, serrated and twisted sections are 10 cm long. The twisted sections with the teeth of the ROSS are designed to center the strain strip in the borehole and grip the grout to ensure sufficient coupling between the ROSS and the rock mass. The strain gages are installed on the narrow straight portion of the ROSS (Fig. 3.2)

because the thinnest point is where the strip should be the most compliant. Thus, strain will be partitioned into the area of the ROSS where the strain gages are located (Signer and Sunderman, 2003). For our work, we began with this basic construction and developed the ROSS for a wider variety of applications.

3.3.2 Fiber-optically Instrumented Rock Strain and Temperature Strips (FROSTS)

The ROSS is typically instrumented with electrical-resistance strain gages at 30 cm intervals along its length (Signer and Sunderman, 2003). In contrast, fiber-optic FBG strain and temperature gages were chosen for several reasons: 1) The coupling of highly accurate temperature gages with the strain gages provides a detailed thermal profile with depth into the rock mass; 2) FBG gages are easily read in the field using off-the-shelf interrogation boxes and manufacturer-supplied software rather than a specially designed and built data acquisition system (Signer and Sunderman, 2003) or time-consuming campaign-style readings; 3) The FBG gages are arranged in series with twelve gages operating off a single fiber-optic cable and interrogation channel, which creates a slimmer design than each resistance gage with its own set of wires; and 4) FBG gages require no calibration and do not have drift over time so an FBG array could be installed with its interrogation box in another location and run indefinitely without any on-site interaction. These enhanced ROSS instruments are called "Fiber-optically Instrumented Rock Strain and Temperature Strips" or FROSTS.

The FROSTS are instrumented with sensor arrays custom-built by Micron Optics Inc. Each array is composed of six OS3200 strain gages accurate to 1 με and six OS4310 absolute temperature sensors accurate to 0.1 °C. The strain and temperature gages are epoxied side by side on each of the straight sections of the FROSTS (Fig. 3.3). The splices between the gages

are epoxied on to the twisted sections of the FROSTS. After the gages were attached to the FROSTS, the entire strip was covered in two coats of a West System two-part epoxy. For further protection, each of the FROSTS is wrapped in linerless rubber splicing tape prior to installation.

3.4 FIELD IMPLEMENTATION

3.4.1 Location

In February 2011, we installed two FROSTS on the 4100 level (~1250 m below the surface) of the Sanford Underground Research Facility (SURF) at the site of the former Homestake gold mine in Lead, SD (Fig. 3.4). In conjunction with the South Dakota Science and Technology Authority (SDSTA) and the Department of Energy (DOE), the Homestake gold mine is being converted to SURF, which is an underground laboratory that will house physics experiments as well as provide some space for underground biology, geology, and engineering research (Kramer, 2011). Monitoring of the rock surrounding the SURF laboratory spaces is critical for the safety and longevity of the laboratory.

The two FROSTS were installed into an alcove measuring 2 m deep by 3 m wide and 2 m tall. One FROSTS was installed vertically into a drill hole in the roof of the alcove. The second FROSTS was installed horizontally into a wall of the alcove (Fig. 3.4).

3.4.2 FROSTS Pretensioning and Installation Technique

As designed by Signer and Sunderman (2003), the ROSS is primarily a tool to measure deformation in mines associated with rock bursts or collapses and failures of excavated surfaces. Thus, ROSS are only meant to measure elongation. Since we are interested in measuring more general strain fields, including both shortening and elongation,

we have developed a method for pretensioning the FROSTS prior to installation, permitting the measurement of both.

For the pretensioning process, ideally, the downhole tip of the FROSTS would be anchored in a borehole, and the FROSTS would be pretensioned *in situ*. Our two-step pretensioning procedure is cumbersome, but mandated by limited underground time. Our procedure was successful, but there is room for improvement in the pretensioning method in future installations.

In order to pretension the FROSTS before arriving at the installation site, the FROSTS were held in a frame composed of two 215 cm long pieces of rebar with two 30 cm wide blocks of 4" x 4" wood on the end (Fig. 3.5). The wooden blocks had 3 holes drilled in them: two for the rebar, and one for the fiber-optic wires of the FROSTS to extend through. The FROSTS were attached to a threaded rod using a specialized clamp and held between the wooden blocks (Fig. 3.6).The threaded rods extend through u-shaped brackets on the outside of the wooden blocks with a nut that was turned to produce tension in the FROSTS (Fig. 3.7). The amount of strain in the FROSTS was monitored using a Micron Optics sm225 laser interrogation box. The FROSTS were pretensioned to ~1,000 με (Fig. 3.8a).

In order to hold the pretension in the FROSTS, the strips were grouted into a ~3.8 cm (1.5 in.) inner-diameter PVC pipe while being held under tension in the frame (Fig. 3.5). Prior to grouting, the inside of the PVC pipe was coated with lithium grease so that the grout would not bond to the pipe. We then poured a quick-setting anchoring cement (Thorogrip) down the PVC pipe. The frame was inclined off the end of a table so that the grout would flow down the pipe. The PVC pipe had breather holes drilled at 30 cm intervals along its length, which

allowed us to monitor the filling of the tube with grout, and to ensure there were no large air bubbles. The grout was completely cured in less than 5 hours, which is recorded by the temperature spike during curing followed by equilibration of temperature (Fig. 3.8).

After curing overnight, we released the FROSTS from the pretensioning frame. The four strain gages in the middle of the FROSTS held between 600 – 300 με of pretension (Fig. 3.8). The strain gages on either end of the two FROSTS lost all pretension when the strips were released from the frames (Fig. 3.8). The strain gages on the ends of the FROSTS did not hold pretension because the two serrated sections at the ends of the FROSTS were held in the brackets that connected the FROSTS to the tensioning frame (Fig. 3.6). Once tension was released, there was nothing to grip the grout above the final sets of sensors and slip occurred between those sensor segments and the grout. After removing the FROSTS from the tensioning frames, the PVC pipe was cut off using a Dremel tool.

It is critical to achieve sufficient coupling between the grout around the FROSTS and the new grout between the FROSTS and the rock mass. Thus, all grease was cleaned from the FROSTS with several applications of a spray degreaser, and the FROSTS were covered with a concrete bonding adhesive.

The FROSTS were then grouted into a ~9 cm (3.5 in.) diameter drill hole in the rock mass using an expanding Portland cement-based grout (Fig. 3.9). Although the FROSTS are only ~3.8 cm (1.5 in.) in diameter, the extra size of the hole was required to accommodate the breather and grout tubes (5/8 in. and 7/8 in. diameter, respectively). Ideally, as small a hole as possible should be used. The quick-drying grout was pumped into the borehole under pressure while the drill holes were sealed with shredded rags during grouting.

3.4.3 Field Implementation: Results

Strain and temperature data from both FROSTS installed on the 4100 level of SURF have been recorded continuously since February 4, 2011. Data from the first three months of monitoring are presented in Fig. 3.10. Both FROSTS record changes in strain and temperature during the initial three month period. During the first two weeks after installation, both FROSTS show numerous changes in strain (Fig. 3.10). These changes are rapid and relatively random. There is no clear pattern with location or depth in the rock mass. After the first two weeks, the sensors do not display any rapid changes in strain. During the subsequent six weeks, the strain sensors show a gradual trend to stabilization at constant value (Fig. 3.10). After strain gage stabilization during the initial six weeks, there is virtually no change in the mechanical strain state of the rock mass (Fig. 3.10).

The FROSTS also record a detailed temperature profile into the rock mass. The FROSTS installed in the roof of the alcove records a temperature gradient where temperature increases with depth into the rock mass (Fig. 3.10a). Sensor A, closest to the surface at 0.62 m deep, is consistently 1 °C cooler than sensor F, the deepest in the rock mass at ~2.3 m deep. The other four temperature sensors fall along a gradient between sensors A and F with increasing temperature corresponding to increasing depth (Fig. 3.10a). The temperature of the rock mass increases ~0.25 – 0.3 °C for every sensor (spaced 35.6 cm apart), or 0.7 °C/m.

The other FROSTS is installed horizontally in a wall of the alcove and the length of the FROSTS is parallel to the drift (Fig. 3.4). This FROSTS does not record a gradient of increasing temperature with depth into the rock mass. Sensor A (closest to the surface)

consistently shows the lowest temperature of all the sensors, but the remaining five sensors all plot at nearly that same temperature (Fig. 3.10b).

3.4.4 Field Implementation: Discussion

3.4.4.1 Pretensioning method

Although cumbersome, the pretensioning method presented was successful. The four internal gages on each of the FROSTS held at least 30% of the initial applied strain (between 300 and 600 με) (Fig. 3.8). However, the two end gages on the FROSTS lost nearly all pretension load (Fig. 3.8), which was expected due to the construction of the pretensioning frame. One caveat with this two-step grouting process is that, while performing the laboratory tests, we noticed that once the PVC pipe was removed from the grout, the grout cylinder developed radial cracks. These cracks took about 3 to 4 days to develop. Thus, it is imperative that the FROSTS be grouted into the rock mass within two days after being cut out of the PVC. The expanding grout that holds the strain strip in the rock mass should be sufficient to keep the tensional cracks from forming. During our installation at SURF, the FROSTS were inspected for cracks prior to placement in the boreholes and no cracks were observed.

The coupling of the FROSTS to the rock mass is critical to ensure strain is accurately measured. It was possible that the FROSTS would not bond to the new grout once cut from the PVC pipe because the FROSTS were coated with grease. Additionally, subsequent generations of concrete commonly do not bond well to each other, even in the absence of lubricants on the interface between them (Wall and Shrive, 1988). We addressed both these issues with the degreaser and concrete bonding adhesive, respectively. Because the strain

record is unique for each sensor on both FROSTS (Fig. 3.10), we can assume sufficient coupling between the FROSTS and the new grout.

A preferred method would be to pretension the FROSTS directly in the borehole and use a single layer of grout to couple the FROSTS with the rock mass. This method would require the development of a down-hole anchor that can hold the FROSTS in the borehole while the pretensioning load is applied and while the grout is curing. The surface pulling device we developed (i.e. the strain strip holder, threaded rod, and u-shaped bracket (Fig. 3.5, 3.6 and 3.7) could easily be adapted to an *in situ* pretensioning method. Pretensioning the FROSTS directly in the borehole is advantageous because it eliminates the uncertainty about the coupling of multiple grout layers. Also, the FROSTS can be grouted into a smaller diameter borehole. It is ideal to use the smallest borehole possible because it disturbs the rock mass less than a larger hole, which will lead to better performance of the strain monitoring tool (Franklin, 1977). Direct pretensioning will also allow the strain gages at the end of the strip to hold the pretension.

3.4.4.2 FROSTS: A new method for monitoring in situ strain and temperature

The FROSTS record a detailed *in situ* strain and temperature profile into the rock mass, which is invaluable for structural health monitoring. During the first two weeks of monitoring, both FROSTS record changes in strain that are different among all the sensors (Fig. 3.10). This strain is a result of the grout curing and small-scale rock movement after drilling. As the grout cured it expanded and strained the FROSTS. Also, because a jack-leg drill was used to drill the boreholes, it is likely that new small-scale fractures and other instabilities were created in the rock mass (Ramezanadeh and Hood, 2010). In addition to

grout curing, the strain recorded in the FROSTS also represents the closure of these openings as the rock mass equilibrates into a stable state after drilling.

The six strain sensors on both FROSTS record distinct strain events (i.e. different magnitude, direction, and time) during the initial monitoring (Fig. 3.10). The independent strain histories for each sensor suggest that the FROSTS are coupled to the rock mass. The individual strain sensors are measuring deformation within the discrete segments of the FROSTS between each set of serrate sections (Fig. 3.10).

Because the sensor installation on the 4100 level of SURF is too far away from new excavations and active tectonism, the fiber-optic sensors do not record any large-scale mechanical strain (Gage et al., 2010). In order to induce measureable strain in the rock mass, we performed two point-loading tests in which we applied 10 ton and 100 ton loads to the rock mass. The point-loading test used hydraulic jacks load to the floor and ceiling of the underground sensor alcove in SURF. The FROSTS recorded strain due to both loading events (from 0 – 5 με for the 10 ton experiment and from 2 – 12 με for the 100 ton experiment) (e.g. Gage et al., 2011a). These data show that the FROSTS are able to measure mechanical strain in the rock mass.

FROSTS also show a trend of increasing temperature from the surface into the rock mass. Following a typical cratonic geotherm, the temperature at the 4100 level, at ~1250 m below the surface, should be ≥ 27.6 °C (Turcotte and Schubert, 2002). Both FROSTS measure lower temperatures than expected from the geothermal gradient (average for sensor A, closest to the rock surface = 23.5 °C). Previous studies of rock mass temperatures in the Poorman formation at the Homestake mine note a similar difference between the temperature measured

in the drift and the expected temperature of the rock mass from the geothermal gradient. On the 4850 level, at ~1480 m below the surface, the measured temperature in the drift is 27.1 °C and the temperature calculated from the geothermal gradient is 32.7 °C (Dobson and Salve, 2009). On the 7000 level, at ~2130 m depth, the measured rock temperature is 37 °C and the temperature calculated from the geothermal gradient is 47.5 °C (Ashworth, 1983). For these three levels in the mine, the measured temperature is 78 – 85% of the expected geothermal temperature. This temperature difference is a result of ventilation cooling of the mine (Dobson and Salve, 2009). The FROSTS installed in the ceiling of the alcove records a gradient of increasing temperature with depth (Fig. 3.10a) due to the difference in temperature in the undisturbed rock and the cooler temperature at the exposed alcove ceiling.

For the FROSTS installed into the wall of the alcove, the temperature gradient is not as well developed as the FROSTS in the ceiling (Fig. 3.10). The sensor closest to the surface has the lowest temperature, and the sensors deeper in the rock mass record a higher temperature, but the five deeper sensors all group within error (0.1 °C) at the same temperature (Fig. 3.10b). The FROSTS in the wall is ~1.5 m from the drift and its length is parallel to the length of the drift (Fig. 3.4). The FROSTS in the wall thus has a second free surface along the drift that further cools the rock mass, and disturbs the temperature gradient. The FROSTS in the roof only has one free surface at the head of the FROSTS, and thus, records the gradient of increasing temperature with depth into the rock mass. As a monitoring tool, FROSTS are sensitive enough to resolve detailed temperature gradients in the rock mass over a range of ~1.5 °C.

3.5 LABORATORY VALIDATION

We performed three different types of laboratory tests to validate the FROSTS instrument and our installation techniques. The goal of the first test was to ascertain that FBG strain and temperature gages perform the same as electrical-resistance strain gages on a ROSS/FROSTS device. For this test, a FROSTS was instrumented with both FBG and electrical-resistance gages and loaded in tension using the pretensioning frame we developed (Figs. 5, 6 and 7).

The second test examined how the FROSTS perform when embedded directly into a rock mass. It is important to confirm that the FROSTS accurately measure strain within the medium being monitored. For this test, a short (~10 cm) segment of FROSTS was grouted into a hollow core of the Lac du Bonnet granite. The granite/grout/FROSTS sample was loaded in compression in a load frame.

The goal of the third test was to determine the effect of the two-step grouting procedure utilized during our pretensioning and installation procedure, described in section 4.2, on the performance of the FROSTS. We assessed the compliance of the FROSTS relative to the grout and whether or not a long section of FROSTS would bend in compression. For this test, a ~41 cm long segment of FROSTS was embedded into a 4 cm diameter cylinder of grout that was then embedded into a 7.6 cm diameter cylinder of grout. The sample assembly was loaded in compression in a load frame.

It is important to clarify terminology for the following laboratory testing sections. Test 2 and 3 involve embedding a segment of FROSTS in granite or grout. For these sections, FROSTS refers to the piece of steel embedded in the grout and/or granite. Also,

measurements for the Young's modulus of the FROSTS refers to the moduli measured by the strain gages installed on the metal piece of FROSTS embedded in the grout or granite. By design, once the FROSTS is surrounded by grout, the steel of the FROSTS is a volumetrically small component of the system. Thus, the moduli measured by the strain gages installed on the FROSTS will be more compliant than the Young's modulus for 304-stainless steel. The moduli reported in tests 2 and 3 for the FROSTS represent the stiffness of FROSTS as a monitoring system.

3.5.1 Test 1: Fiber-optic and electrical resistance gages performance on FROSTS

3.5.1.1 Test 1: Methods

A FROSTS was suspended in a pretensioning frame (Fig. 3.5, 3.6 and 3.7) with a Futek inline load cell, model # LCM325, to measure the tensional load. One side of the FROSTS was instrumented with six electrical-resistance strain gages, in the same manner as Signer and Sunderman (2003). On the opposite side of the FROSTS, six strain and six temperature FBG gages were co-located with the electrical-resistance gages (Fig. 3.11). The area of the FROSTS where the strain gages were installed is 1.27 cm wide and 1.5 mm thick. The FROSTS was deformed in tension to 650 lbs. (~2900 N). Strain data were collected during six loading and unloading cycles.

3.5.1.2 Test 1: Results

For each loading and unloading cycle, all twelve strain gages (six electrical-resistance and six fiber-optic) on the FROSTS behaved nearly the same. The representative data in Fig. 3.12 show that the stress-strain curve for correlative electrical-resistance gages and fiber-optic FBG gages is nearly the same both in terms of slope and magnitude. For both the electrical-

resistance gages and the fiber-optic gages, there is virtually no hysteresis in the measurements (Fig. 3.12). There is also no pattern of strain partitioning along the FROSTS. All gages deform the same, and record similar amounts of strain regardless of location on the FROSTS (Table 3.1). The handbook value for Young's modulus of 304-stainless steel is 199.6 GPa (Ledbetter et al., 1980). The Young's moduli from each testing cycle and each of the twelve strain gages are shown in Table 3.1. The average Young's modulus for the 304-stainless steel of the FROSTS is 203.7 GPa as measured by the electrical-resistance gages, and 216.7 GPa as measured by the FBG gages. Thus, the fiber-optic strain gages measure a 6% higher Young's modulus than the electrical-resistance gages.

3.5.1.3 Test 1: Discussion

Both the FBG and electrical-resistance gages behaved the same during laboratory testing. The correlative gage pairs measured similar strain magnitudes at each location along the FROSTS (Table 3.1). The fiber-optic strain gages consistently recorded strain at about 6% higher than the electrical-resistance gages (Table 3.1). This difference in strain between the electrical-resistance gages and FBG gages could be due to stiffness differences between the fiber and the copper wire, or between the packaging of the gages: the foil backing of the electrical gages and the rubber housing of the FBGs. Although this discrepancy has been noted previously (Moyo et al., 2005) the FBG strain and temperature gages are rigorously calibrated and tested during manufacturing (Davis et al., 1996), so this small discrepancy between the optical and resistance gages should not affect the accuracy of strain measurement. Thus, substituting fiber-optic strain gages for the electrical-resistance strain gages of Signer and Sunderman (2003) does not affect the performance of the FROSTS tool.

Also, both the FBG and electrical-resistance gages accurately measure the Young's modulus for the steel of the FROSTS. The Young's modulus of 304-stainless steel in tension is 199.6 GPa (Ledbetter et al., 1980). The FBG and electrical-resistance gages measure 216.7 and 203.7 GPa, respectively, which is within the error of Ledbetter et al.'s (1980) experiments, and is further validation of the FROSTS method and the use of fiber-optic strain gages.

3.5.2 Test 2: FROSTS grouted into hollow core of the Lac du Bonnet granite

3.5.2.1 Test 2: Methods

Electrical-resistance strain gages were installed on both sides of a 10 cm long serrated section of a FROSTS. The FROSTS was twisted ~30° above and below the strain gages. This section of FROSTS was then grouted into a 5.8 cm diameter hole drilled in a 10 cm diameter core of Lac du Bonnet granite using Thorogrip grout (Fig. 3.13). Seven electrical-resistance strain gages were installed on the outside of the granite core. Five strain gages were oriented axially and two radially (Fig. 3.13). Because the wires connected to the strain gages on the embedded FROSTS were coming out of the top of the sample, a 2.5 cm thick layer of grout was poured on top of the granite sample to create a flat base. The granite core was ~12 cm tall; total sample height was ~14.5 cm. The sample was left unconfined and loaded in axial compression to ~ 89 kN (20,000 lbs.). Strain data were collected during six loading and unloading cycles.

3.5.2.2 Test 2: Results

The measured stiffness of the FROSTS segment is significantly lower than the surrounding rock. The stress-strain curves measured by the strain gages installed on the

FROSTS record a very compliant Young's modulus of 22.5 GPa for the grout inside the granite core (Table 3.2). The apparent Young's modulus measured for the annular sample of Lac du Bonnet granite is 37.1 GPa with an average Poisson's ratio of 0.14 (Fig. 3.14). The stress-strain curves of the FROSTS show virtually no hysteresis and very slight hysteresis for the granite (Fig. 3.14). Data for the Young's moduli of the FROSTS and Lac du Bonnet granite as well as the Poisson's ratio for the granite are shown in Table 3.2.

The strain gages on both sides of the FROSTS measure the same strain during each test (Table 3.2). However, the Young's modulus for the first loading cycle is significantly higher (27.7 GPa) than the subsequent five tests (21.4 GPa). Also, the five axial strain gages on the outside of the granite core do not behave the same (Table 3.2), but all the Poisson's ratio measurements are very similar.

3.5.2.3 Test 2: Discussion

When embedded into a rock mass, the FROSTS are more compliant than the surrounding rock mass. The FROSTS embedded in grout in the granite core record a Young's modulus of 22.5 GPa for the FROSTS (Table 3.2). The Lac du Bonnet granite records an average Young's modulus of 40.1 GPa. Ideally, a strain monitoring tool will have similar mechanical properties to the rock mass so that the strain field is not affected by the instrument (Franklin, 1977). However, an exact match of properties is difficult to achieve, thus it is important to make sure the strain gage is more compliant than the rock mass. If the strain gage is stiffer than the rock mass, it will not accurately measure strain in the rock mass and may not detect important changes (Serbousek et al., 1985; Maleki et al., 1994; Signer and Sunderman, 2003).

The FROSTS embedded in the granite cores records the most compliant Young's modulus measured for the surrounding granite cylinder. In an intact rock mass, the variation of the stiffness of the surrounding material will not vary as widely as the granite core in experiment #2 (Table 3.2), thus the FROSTS will more accurately record deformation in the rock mass (Signer and Sunderman, 2003).

The accepted Young's modulus for the Lac du Bonnet granite is 55 ± 10 GPa (Martin, 1990), which is significantly higher than the Young's modulus measured in the laboratory experiments. Similarly, the Poisson's ratio was measured at 0.14, which is lower than the accepted value at 0.30 ± 0.15 (Martin, 1990). This difference between our laboratory measurements and the accepted material properties of the Lac du Bonnet granite is attributed to the geometry of the sample. The FROSTS was grouted into a 5.8 cm diameter drillhole in a 10 cm diameter Lac du Bonnet core, which makes the test sample a composite material of the granite and grout. Thus, the strain gages on the outside of the granite measure the material properties of the composite, not just the granite (Nielsen, 1992).

The stiffness of composite samples with coaxial cylinders of different materials ($E_{composite}$) can be estimated using equation 22 from Wilczynski (1992):

$$E_{composite} = E_1 f_1 * E_2 f_2 \tag{3.3}$$

where E_1 and E_2 are the Young's moduli of the two materials in the composite and f_1 and f_2 are their volumetric fractions. For the granite/grout sample, the Young's modulus of the sample should be 39.3 GPa, using $E_{granite}$ = 55 GPa (Martin, 1990) and E_{grout} = 20 GPa. The

predicted 39.3 GPa is similar to the 40.1 GPa measured in the laboratory. When the FROSTS is installed in the field, the rock mass is essentially infinite, so this composite stiffness effect should be negligible (Wilczynski, 1992).

In laboratory test #2, we have shown that the FROSTS, as a strain monitoring tool, is more compliant than the rock mass into which it is embedded. However, the measured Young's moduli for the gages on the outside of the granite cylinder have significant differences among the strain gages around the circumference of the sample. These inconsistencies may be a result of uneven stress distribution during loading. The inner cylinder was slightly off-center, so the grout is not perfectly concentric within the granite. The recorded Young's modulus values vary in a gradient around the rock mass. Where the granite cylinder is the thinnest (near gage #4; Table 3.2) the Young's modulus is the lowest (22.7 GPa). Similarly, where the granite cylinder is the thickest (near gage #2; Table 3.2) the Young's modulus is the greatest (66.7 GPa) and most closely approximates the upper limit of the accepted range for the Young's Modulus of the Lac du Bonnet granite (Martin, 1990). Thus, the uneven thickness of the granite may create the differences in stress distribution during loading.

3.5.3 Test 3: FROSTS and two-step grouting procedure

3.5.3.1 Test 3: Methods

A laboratory simulation was made of the two-step grouting procedure used during the field installation (Section 4.2). Electrical-resistance strain gages were installed on both sides of a 41 cm long section of FROSTS that included a 20 cm long straight section between two 10 cm long serrated sections twisted 60° (Fig. 3.15). The strain gages were installed at the

midpoint of the straight section of the FROSTS. The FROSTS was grouted into a 46 cm long greased section of 4 cm inner-diameter PVC pipe using Thorogrip grout. After the grout cured completely, the PVC pipe was removed and a degreaser was applied to the grout. Four electrical-resistance strain gages were installed on the surface of the 4 cm diameter grout cylinder midway along its length. Two strain gages were oriented axially and two radially on the core (Fig. 3.15).

After strain gage installation, the 4 cm diameter grout cylinder was stored at room temperature for 3 weeks. After that time, the cylinder was grouted into a 56 cm long greased section of 7.6 cm inner-diameter PVC pipe using Thorogrip grout (Fig. 3.15). Again, after the grout was completely cured, the PVC pipe was removed and a degreaser was applied to the grout. Four electrical-resistance strain gages were installed halfway down the length of the outer grout cylinder; two axial and two radial, for a total of ten strain gages on the sample: two on the steel of the FROSTS, four on the 4 cm diameter inner cylinder of grout, and four on the 7.6 cm diameter outer cylinder of grout (Fig. 3.15). The final sample dimensions were 56 cm long and 7.6 cm in diameter. The sample was stored at room temperature for 3 days before performing the loading tests. The sample was unconfined and loaded in compression to 2,500 lbs. (~11 kN). Strain data were collected during four loading and unloading cycles.

3.5.3.2 Test 3: Results

The stress-strain curves for the gages on the FROSTS record an average Young's modulus of 12.5 GPa, while the average Young's modulus measured by the strain gages on the inner and outer layers of grout is 17.9 GPa (Fig. 3.16). The average Poisson's ratio for the grout is 0.19. The stress-strain curves for the FROSTS and both layers of grout show very

little hysteresis during loading and unloading (Fig. 3.16). Data for the Young's moduli of the steel of the FROSTS and both layers of grout as well as Poisson's ratio for both layers of grout are shown in Table 3.3.

The strain gages on both sides of the FROSTS measure the same strain during each test (Table 3.3). However, the two layers of grout do not behave similarly. The 4 cm diameter cylinder of grout (the inner grout layer) has a consistently higher average Young's modulus (21.2 GPa) than the 7.6 cm diameter cylinder (the outer layer of grout) at 14.5 GPa. Also, the two gages on opposite sides of the 4 cm diameter cylinder of grout measure significantly different amounts of strain (Fig. 3.16), which may be a result of uneven distribution of the load during testing. Poisson's ratio also varies from an average of 0.17 to 0.21 between the layers of grout (Table 3.3).

3.5.3.3 Test 3: Discussion

Because the FROSTS is a volumetrically small component of the test sample, the strain gages on the FROSTS should measure the stiffness of the grout. However, the strain gages on the FROSTS record a more compliant Young's modulus than the strain gages on the outside of both layers of grout (Table 3.3). The Young's modulus recorded by the strain gages on the FROSTS is most similar to that of the outer layer of grout (12.5 GPa and 14.5 GPa), and significantly lower than the inner layer of grout.

The difference in the Young's moduli between the inner and outer layers of grout (21.2 GPa and 14.5 GPa, respectively) suggest that the two layers of grout may not be coupled. However, data from the field implementation (see section 3.4.4.2) and experiments (Gage et al., 2011a) suggest that the FROSTS are coupled to the rock mass through the two

layers of grout. The discrepancy in the Young's moduli between the two layers of grout could be attributed to a stiffness difference between the two layers. Cement-based grouts increase in stiffness with curing time. There is generally a 50% stiffness increase between 3 and 28 days of curing (Benmokrane et al., 1995). At the time of deformation, the inner cylinder of grout had cured for 24 days and the outer cylinder for only 3 days, which would create a significant stiffness difference between the two layers of grout.

In order to test the effect of curing time on grout stiffness, we deformed a sample of pure grout (i.e. no embedded FROSTS or multiple grout layers) measuring 11.5 cm (4.5 in.) tall and 3.8 cm (1.5 in.) in diameter. The grout was deformed at 3 days and 24 of curing time. The pure grout sample has nearly the same Young's moduli and Poisson's ratios as measured for the inner and outer grout layers (Table 3.4), which suggests that the discrepancy in stiffness is indeed a result of curing time. For the FROSTS installed on the 1250 m level of SURF, the difference in curing time between the two grout layers was less than 24 hours, so this effect should be small. Also, Portland cement-based grouts generally reach their peak and stable stiffness at approximately 2 months of curing time (Benmokrane et al., 1995), thus stiffness differences due to curing time are negligible for long-term strain monitoring using FROSTS.

It is also important to note that the grout is more compliant than most rock types (Turcotte and Schubert, 2002); therefore, Thorogrip grout is a good choice for FROSTS installation. The type of grout can be varied to simulate rock properties as desired. Strain gages on both sides of the FROSTS record the same strain (Table 3.3), which suggests that this long (~46 cm) section of FROSTS did not bend in compression. Since no bending was

observed in the FROSTS, we can conclude that the FROSTS is coupled to the grout and that FROSTS are useful tools for measuring shortening in rock masses.

3.6 CONCLUSIONS

1) The conversion of Rock Strain Strips (ROSS) (Signer and Sunderman, 2003) to Fiber-optically Instrumented Rock Strain and Temperature Strips (FROSTS) by replacing the electrical-resistance strain gages with fiber-optic FBG strain and temperature sensors does not affect the accuracy or sensitivity of the instrument.

2) FROSTS have several key advantages over ROSS: the fiber-optic gages increase the long-term stability of the instrument and do not require calibration. Also, by replacing the electrical-resistance gages with fiber-optic gages the design is streamlined by reducing the number of cables in the borehole.

3) The addition of fiber-optic temperature sensors to the FROSTS provides the advantage of a detailed temperature profile with depth into the rock mass. Incorporating temperature sensors gives FROSTS the capability of measuring thermal properties of rock simultaneously with deformation.

4) Pretensioning the FROSTS prior to installation allows them to measure both shortening and elongation. Our two-step pretensioning procedure, while successful, is not the best method for FROSTS pretensioning. It would be ideal to pretension the FROSTS directly in the borehole during installation.

5) The FROSTS, once embedded in a rock mass, is more compliant than both the grout and rock mass, which allows the FROSTS to accurately measure strain in the rock mass. Also, the FROSTS are sufficiently coupled to the rock mass, ensuring accurate strain measurements.

6) FROSTS provide an accurate and detailed record of *in situ* strain and temperature in intact rock masses and are a useful new tool for the structural heath monitoring of underground spaces.

3.7 ACKNOWLEDGMENTS

This work was supported by National Science Foundation Grants to Wang (CMMI-0900351) and MacLaughlin (CMMI-0821788). The authors wish to thank the South Dakota Science and Technology Authority especially Jaret Heise, Tom Trancynger, and Jason Van Beek for logistical support during the installation. We are also grateful to Neal Lord for laboratory support and assistance, Branko Glisic (Princeton University), Steve Gabriel (Spearfish Schools), Rich Barry (Crazy Horse Memorial), Matt Kogle and Andres Tascon (UW-Madison) for assistance in the field and Steve Signer for fruitful discussion about the ROSS instrument. This work was supported by the National Science Foundation under Cooperative Agreements PHY-0717003 and PHY-0940801 with the University of California, Berkeley. Any opinions, findings, and conclusions or recommendations expressed in this material are those of the author(s) and do not necessarily reflect the views of the National Science Foundation.

References

Ashworth, E. (1983) *The Applications of Finite Element Analysis to Thermal Conductivity Measurements.* Master of Science thesis, South Dakota School of Mines and Technology.

Benmokrane, B., Chennouf, A., and Mitri, H.S. (1995) Laboratory evaluation of cement-based grouts and grouted rock anchors. *International Journal of Rock Mechanics, Mining Sciences & Geomechanics Abstracts.* 32: 633-642.

Bhalla, S., Yang, Y.W., Zhao, J., and Soh, C.K. (2005) Structural health monitoring of underground facilities – Technological issues and challenges. *Tunnelling and Underground Space Technology*. 20: 487-500.

Boyle, A. (1995) Rock bolt load sensor. *United States Patent 5392654*.

Burland, J.B., Moore, J.F.A., and Smith, P.D. (1972) A simple and precise borehole extensometer. *Geotechnique*. 22:1 74-177.

Davis, M.A., Bellemore, D.G., Putnam, M.A., and Kersey, A.D. (1996) Interrogation of 60 FibreBragg Grating Sensors with Microstrain Resolution Capability. *Electrical Letters.* 32: 1393-1394.

Dobson, P.F. and Salve, R. (2009) Underground Reconnaissance and Environmental Monitoring Related to Geologic CO2 Sequestration Studies at the DUSEL Facility, Homestake Mine, South Dakota. *Ernest Orlando Lawrence Berkeley National Laboratory, Earth Sciences Division*. Report LBNL-2858E.

Farmer, I.W. (1975) Stress distribution along a resin grouted anchor. *International Journal of Rock Mechanics, Mining Sciences & Geomechanics*. 12: 347-351.

Franklin, J.A. (1977) The monitoring of structures in rock. *International Journal of Rock Mechanics Mining Sciences & Geomechics Abstracts*. 14: 163-192.

Gage, J.R., Noni, N., Turner, A., MacLaughlin, M., and Wang, H.F. (2010) Fiber optic strain and temperature monitoring in crystalline rock at the Sanford Underground Science and Engineering Laboratory (SUSEL), Lead, South Dakota, *44th U. S. Rock Mechanics Symposium and 5th U.S- Canadian Rock Mechanics Symposium*, *Salt Lake City, 27 – 30 June.* 8 pp.

Gage, J.R., Wang, H.F., Fratta, D., MacLaughlin, M., and Turner, A. (2011a) The variation of the mechanical properties of rock on spatial scales from the laboratory to the outcrop. *Abstract H21B-1095 presented at 2011 Fall Meeting, AGU, San Francisco, Calif., 5-9 Dec.*

Gage, J.R., Wang, H.F., MacLaughlin, M., Turner, A., and Fratta, D. (2011b) A new method for measuring in situ strain in intact rock masses: Fiber optically instrumented rock strain and temperature strips (FROSTS). *45th US Rock Mechanics Symposium, San Francisco, CA June 26-29*. 10 pp.

Glisic, B. and Inaudi, D. (2007) *Fibre Optic Methods for Structural Health Monitoring.* 1st ed. Sussex: Chinchester. 276 pp.

Hasse, K. (2007) Strain sensors based on Bragg gratings. *In: IMEKO 20th TC3, 3rd TC16 and 1st TC22 International Conference Cultivating metrological knowledge, 27 – 30 November.*8pp.

Hedley, D.G.F. (1969) Design criteria for multi-wire borehole extensometer systems. *1st Canadian Symposium on Mining, Surveying, and Rock Deformation Measurements, Fredericton*.

Johnston, J.L. and Cox, D.J. (1993) Instrumentation procedures for fully grouted rock bolts. *U.S. Bureau of Mines Information Circular 9341*. 1-10.

Kincade, K. (2006) Optoelectric applications: Fiberoptic sensing – Fiber sensors lay groundwork for structural health monitoring. *Laser Focus World*. 42.

Kramer, D. (2011) Funding for NSF underground laboratory is rejected. *Physics Today*. 21.

Ledbetter, H.M., Frederick, N.V., and Austin, M.A. (1980) Elastic-constant variability in stainless-steel 304. *Journal of Applied Physics*. 51: 305-309.

Littlejohn, S. (1993) Overview of rock anchorages In: *Comprehensive Rock Engineering: Principles, Practice, and Projects.* Pergamon Press. p. 413-450.

Maleki, H., Signer, S.P., King, M.E., and Edminster, P.A. (1994) Evaluation of support performance in a highly stressed mine. *Proceedings of the 13th International Conference on Ground Control in Mining (Morgantown, WV Aug. 2-4).* 9-17.

Martin, C.D. (1990) Characterizing *in situ* stress domains at the AECL Underground Research Laboratory. *Canadian Geotechical Journal*. 23: 631-646.

Matsui, H., Kashiwai, Y., Sano, O., Tokunaga, T., He, Z., Mogi, K., and Wang, H.F. (2009) Evaluation of the applicability of optical fiber strain sensors for monitoring rock deformation caused by ocean tide – A case study at the Aburatsubo site, Japan. *EOS Trans. AGU. 2009;* 90: Abstract H23E-1010.

Micron Optics Inc. (2010) Optical Fiber Sensors Guide: Fundamentals & applications. http://www.micronoptics.com/uploads/library/documents/Micron%20Optics%20Optical%20Sensing%20Guide.pdf. Accessed February 19, 2012.

Milner, R.M. (1969) Accuracy of measurements with steel tapes. *Building Research*. Station. CP51/69.

Mine Safety and Health Administration (MHSA). (2011) http://www.msha.gov/stats/Statistics.HTM. Accessed January 23, 2012.

Moyo, P., Brownjohn, J.M.W., Suresh, R., and Tjin, S.C. (2005) Development of fiber Bragg grating sensors for monitoring infrastructure. *Engineering Structures*. 27: 1828-1834.

Nielsen, L.F. (1992) Stiffness of fibre composites – A simple approach. *Building Material Library: Technical University of Denmark*. TR-264(1992): 16pp.

Ramezanzadeh, A. and Hood, M. (2010) A state-of-the-art review of mechanical rock excavation technologies. *International Journal of Mining & Environmental Issues*. 1: 29-39.

Rao, Y.J. (1999) Recent progress in applications of in-fibre Bragg grating sensors. *Optics and Lasers in Engineering*. 31: 297-324.

Serbousek, M.O. and Signer, S.P. (1985) Load transfer mechanics in fully grouted roof bolts. *4th Conference on Ground Control in Mining (Morgantown, WV, July 22-24)*. 32-40.

Signer, S.J. and Sunderman, C. (2003) New tools for roof support evaluation and design. *In Proceedings of the 22nd International Conference on Ground Control in Mining, Morgantown, August 5-7*.

Turcotte, D.L. and Schubert, G. (2002) *Geodynamics. 2nd ed*. Cambridge: Cambridge University Press. p. 132-194 and 292-338.

Wall, J.S. and Shrive, N.G. (1988) Factors affecting bond between new and old concrete. *ACI Materials Journal*. 85: 117-125.

Whittaker, B.N and Hodgkinson, D.R. (1970) Strata displacement measurement by multi-wire borehole instrumentation. *Colliery Guard*. 218: 445-449.

Wilczynski, A.P. (1992) Longitudinal compressive strength of a unidirectional fibrous composite. *Composites Science and Technology.* 45: 37-41.

Winsor, C.R. (1997) Rock reinforcement systems. *International Journal of Rock Mechanics & Mining Sciences*. 34: 919-951.

Zhang, W., Gao, J., Shi, B., Cui, H., and Zhu, H. (2006) Health monitoring of rehabilitated concrete bridges using distributed optical fiber sensing. *Computer Aided Civil and Infrastructure Engineering.* 21: 411-424.

Table 3.1. Young's modulus (GPa) of 304-stainless steel in tension

	Electrical Resistance Strain Gages						Fiber Optic Strain Gages					
Test	eA	eB	eC	eD	eE	eF	oA	oB	oC	oD	oE	oF
1	205.6	199.4	226.4	179.7	212.9	214.6	222.6	214.6	186.8	257.3	205.0	194.9
2	196.7	198.0	219.3	184.6	211.1	211.4	227.9	217.6	194.0	244.7	205.1	208.3
3	195.7	196.6	218.1	186.8	212.0	211.4	235.0	217.1	194.9	242.6	203.2	209.9
4	193.3	199.1	216.8	187.9	211.4	210.7	232.9	218.9	197.2	239.8	206.1	214.3
5	192.6	198.1	217.1	186.9	210.4	210.0	227.4	217.5	195.8	239.2	205.2	211.4
6	193.2	199.1	217.1	188.8	214.0	214.9	236.9	219.9	197.7	239.6	206.4	214.0
Average	195.6	198.0	218.6	186.1	211.9	211.8	230.5	217.6	194.4	243.9	205.2	208.8
	Average resistance strain gages				203.7 GPa		Average fiber-optic gages				216.7 GPa	

Table 3.2. Moduli measured by strain gages on FROSTS and on the surface of Lac du Bonnet granite core

Test	Young's modulus (GPa) strain gages on FROSTS		Young's modulus (GPa) from axial gages on granite					Poisson's ratio from radial gages on granite	
	#1	#2	#1	#2	#3	#4	#5	#1	#2
1	27.5	27.8	43.4	66.3	28.3	21.7	37.6	0.10	0.17
2	20.7	21.1	46.3	67.4	29.0	23.2	37.7	0.13	0.15
3	21.4	21.7	45.2	66.3	28.9	23.1	36.5	0.13	0.15
4	21.4	21.7						0.13	0.15
5	21.4	21.7						0.14	0.14
6	21.5	21.8						0.14	0.15
Average	22.3	22.6	45.0	66.7	28.7	22.7	37.3	0.13	0.15
	22.5 GPa		40.1 GPa					0.14	

Table 3.3. Moduli measured by strain gages on FROSTS and two layers of grout

	Young's modulus (GPa) from strain gages on FROSTS		Young's modulus Grout (GPa)				Poisson's ratio grout			
			Axial gages on inner grout layer		Axial gages on outer grout layer		Radial gages on inner grout layer		Radial gages on outer grout layer	
Test	#1	#2	#1	#2	#1	#2	#1	#2	#1	#2
1	12.4	12.3	25.1	18.0	13.2	14.7	0.14	0.20	0.26	0.19
2	12.5	12.4	25.0	16.9	14.5	14.5	0.15	0.19	0.25	0.17
3	12.6	12.5	25.8	16.5	15.2	14.3	0.15	0.19	0.25	0.17
4	12.6	12.4	26.1	16.3	15.4	14.3	0.14	0.19	0.24	0.18
Average	12.5 GPa		21.2 GPa		14.5 GPa		0.17		0.21	

Table 3.4. Moduli measured by strain gages on pure grout sample at different curing times

	Tests at 3 days of curing time				Tests at 24 days of curing time			
	Young's modulus from axial strain gages		Poisson's ratio from radial strain gages		Young's modulus from axial strain gages		Poisson's ratio from radial strain gages	
Test	#1	#2	#1	#2	#1	#2	#1	#2
1	15.6	14.9	0.24	0.26	21.8	21.3	0.18	0.17
2	13.5	12.6	0.21	0.21	20.1	21.1	0.15	0.18
3	13.3	14.3	0.20	0.19	21.2	20.3	0.17	0.16
4	13.6	14.7	0.19	0.20	21.0	20.5	0.18	0.17
Average	14.1 GPa		0.22		20.9 GPa		0.17	

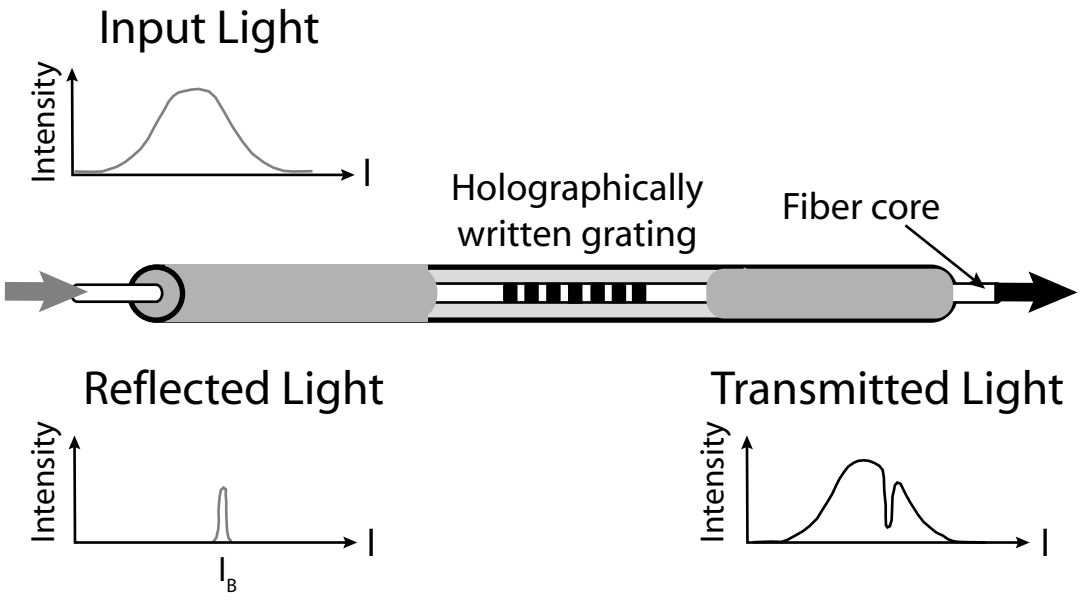

Figure 3.1. Diagram of a Fiber Bragg Grating with input, reflected, and transmitted light. Light with the wavelength of the Bragg grating (I_B) is reflected. The Bragg wavelength changes with strain and temperature. After Hasse, 2007.

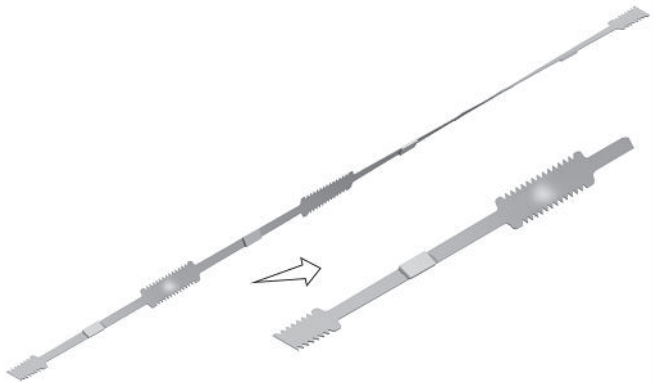

Figure 3.2. Sketch of Rock Strain Strip showing dog-bone configuration with 60° twist. White patches denote location of strain gages. From Signer and Sunderman (2003).

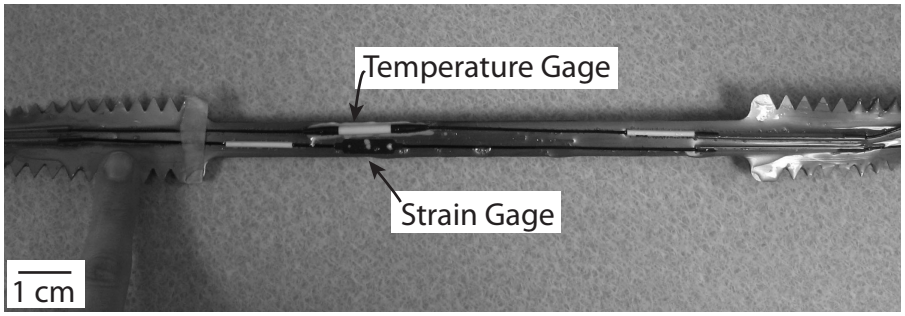

Figure 3.3. Photograph of fiber-optic strain and temperature sensors on FROSTS. Note that the sensors are epoxied on the narrow area of the strip between two sets of wider, serrated areas that are twisted 60°.

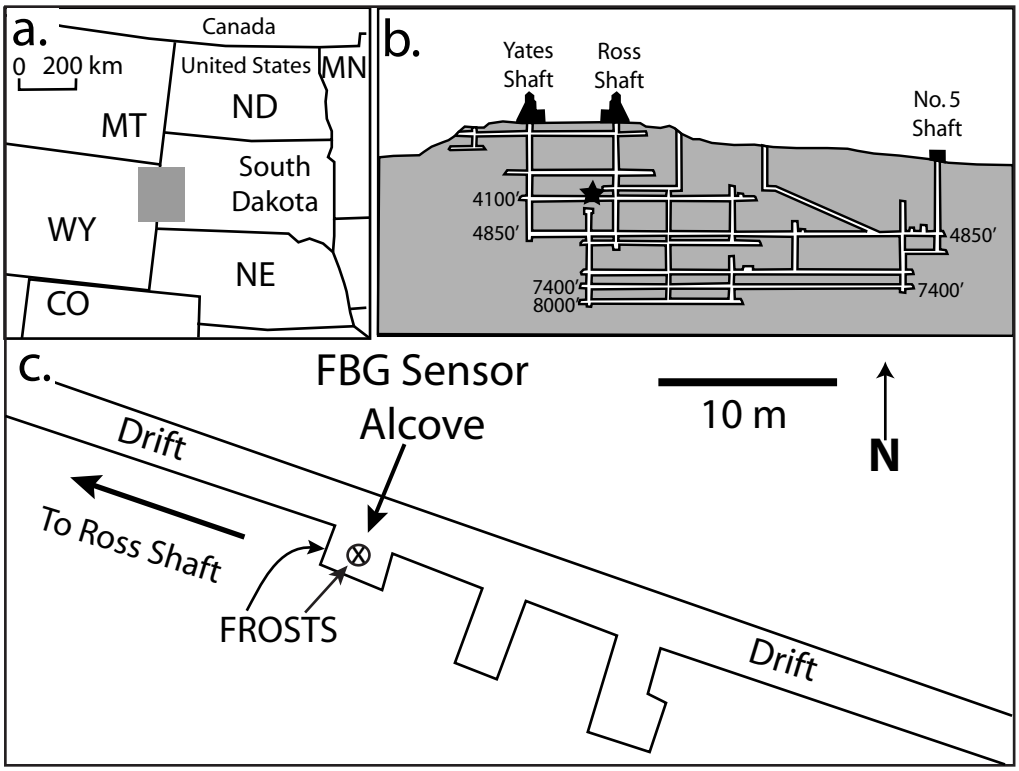

Figure 3.4. a.) Map of the western United States, gray box denotes the location of the Black Hills in western South Dakota; b.) Schematic cross section of Sanford Underground Research Facility showing major science levels. After (Pariseau et al., 1995b). Black star denotes approximate location of experiment; c.) Map view of experiment alcove on the 1250 m (4100 ft.) level. Location of FROSTS is noted. One FROSTS is embedded in the roof of the alcove, and the other is embedded in the alcove wall.

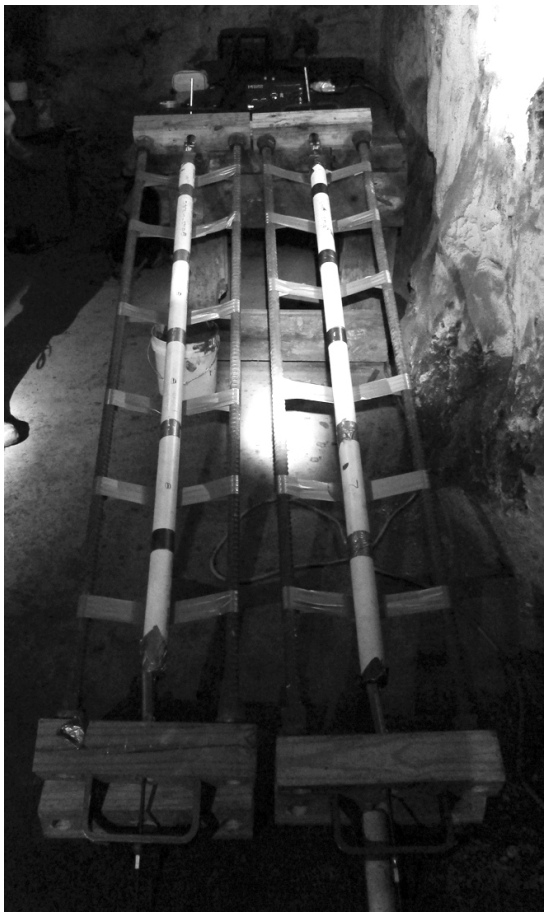

Figure 3.5. Photograph of two FROSTS in pretensioning frames. The FROSTS are grouted into the PVC pipes while being held in tension. The frames are inclined off the table to allow the grout to fully fill the pipe, surrounding the FROSTS, from bottom to top. The duct tape on the PVC pipe covers the breather holes, and the duct tape spanning the rebar provides support for the PVC pipe filled with grout.

Figure 3.6. Close-up photograph of bracket holding FROSTS in the pretensioning frame.

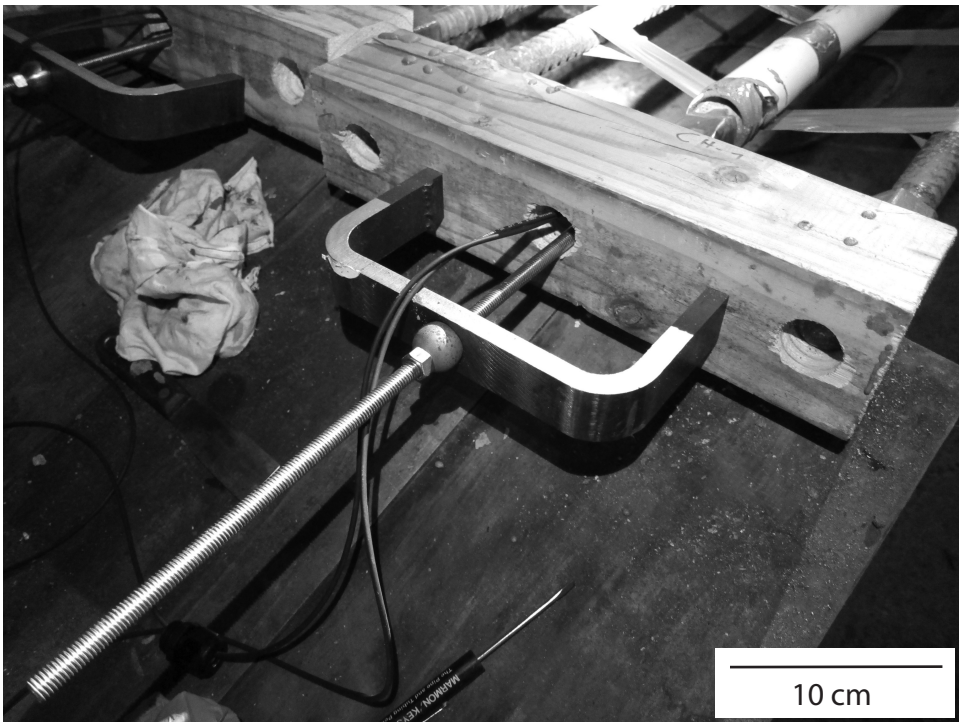

Figure 3.7. Close-up photograph of the top of the pretensioning frame. The threaded rod is connected to the FROSTS bracket (Fig. 3.6) the nut at the top end of the u-shaped bracket provides tension pulling on the FROSTS when tightened.

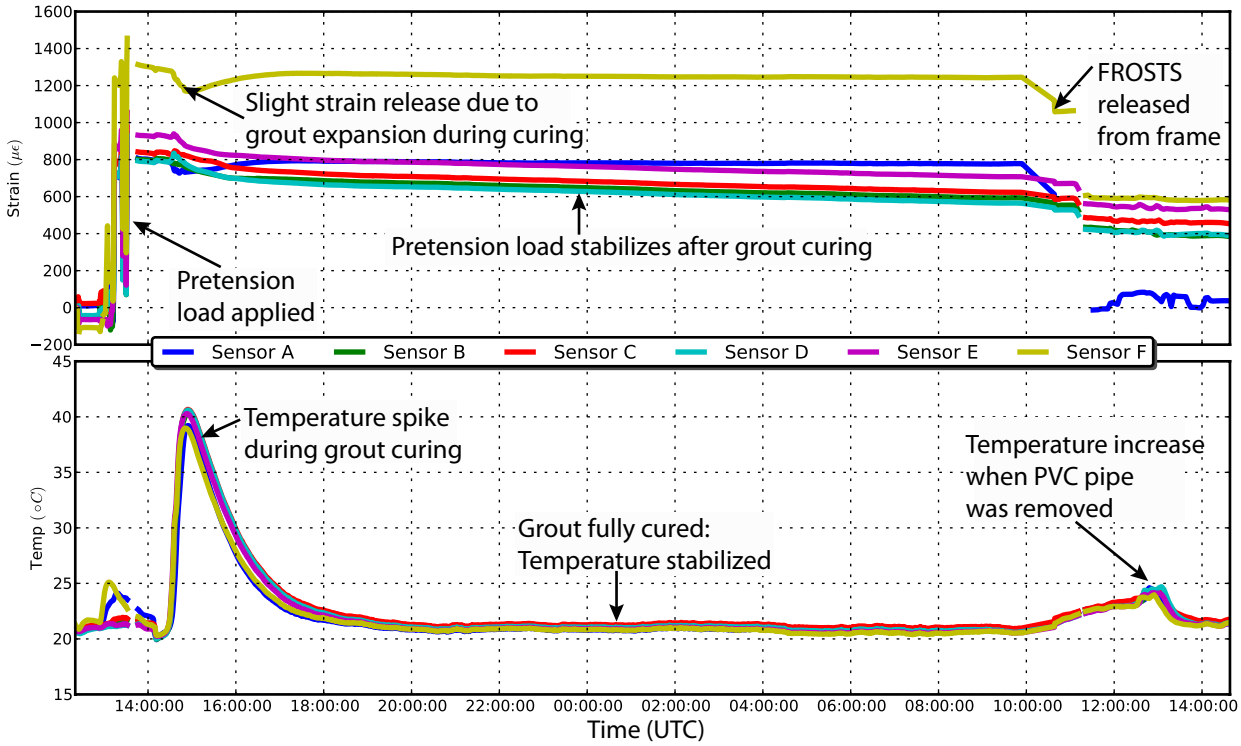

Figure 3.8. Graphs of strain vs. time (top) and temperature vs. time (bottom) for one FROSTS during the pretensioning process. Each FROSTS has six strain and six temperature sensors. The strain/temperature sensor pairs are ordered alphabetically. Data were collected at 1 second intervals. The graphs are annotated for events in the pretensioning process that are discussed in the text.

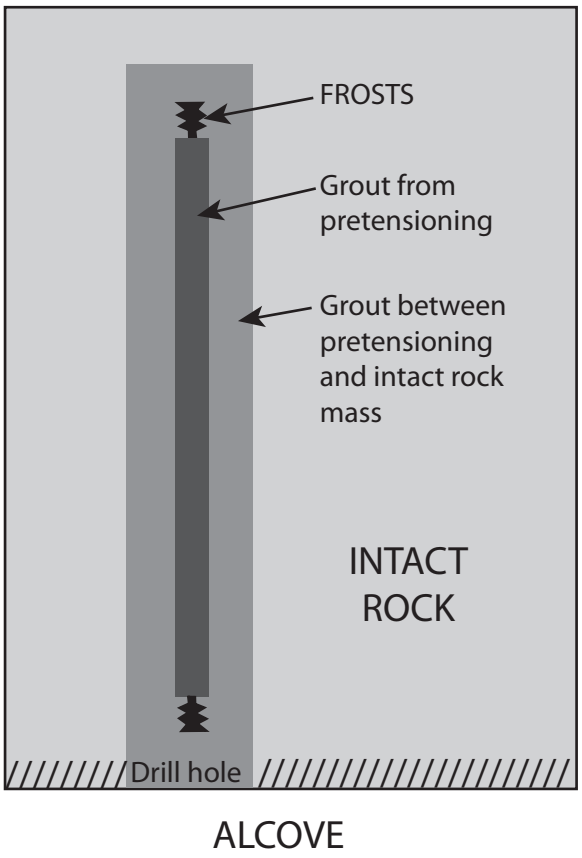

Figre 3.9. Schematic cross section through FROSTS and two layers of grout after final installation into the rock mass

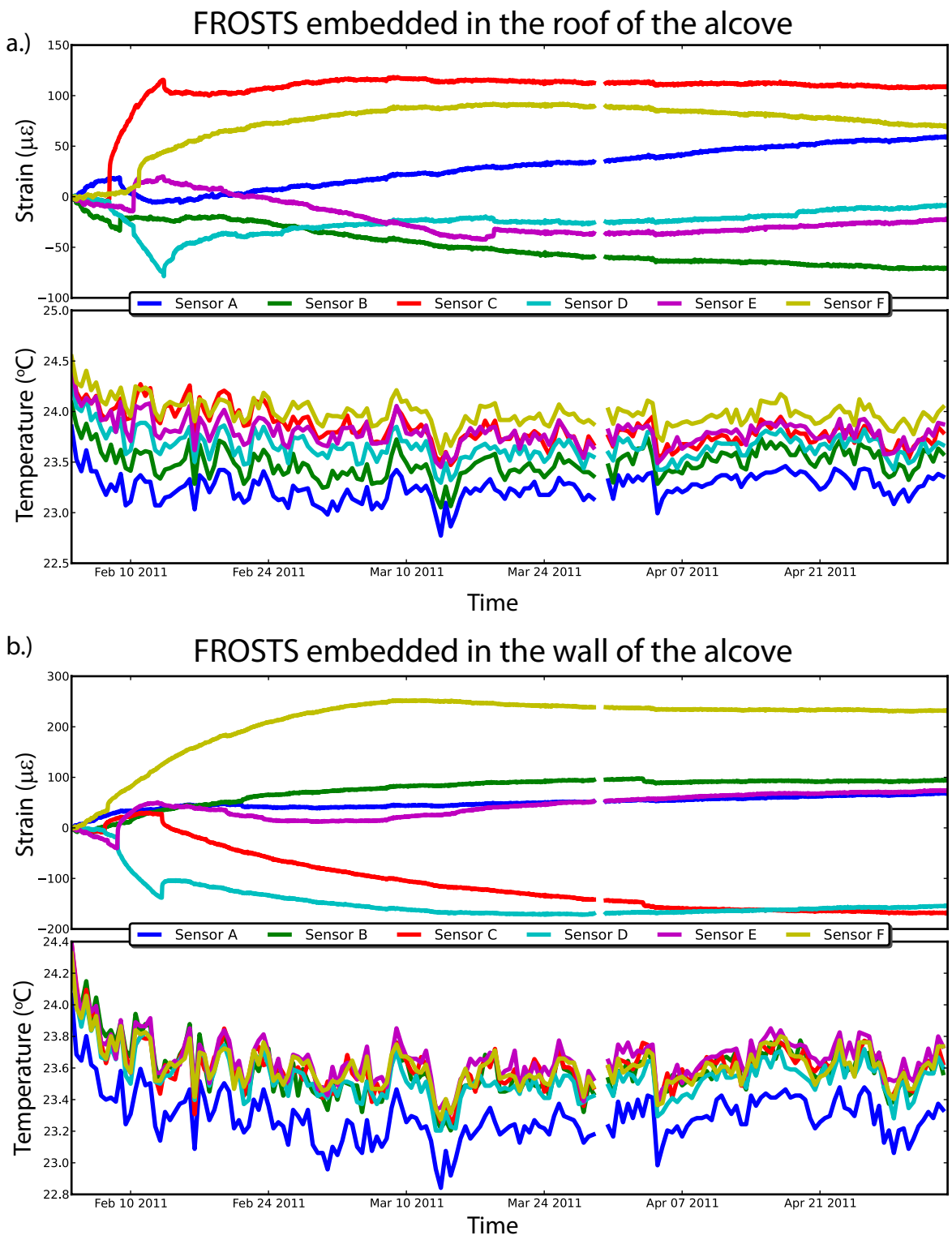

Figure 3.10. Graphs of strain vs. time (a & b top) and temperature vs. time (a & b bottom) for two FROSTS after installation. Each FROSTS has six strain and six temperature sensors. The strain/temperature sensor pairs are ordered alphabetically with sensor A being closest to the rock surface and sensor F being deepest in the rock mass. Data were collected at 1 second intervals. Initial strain values were normalized to zero to show changes in strain between sensors.

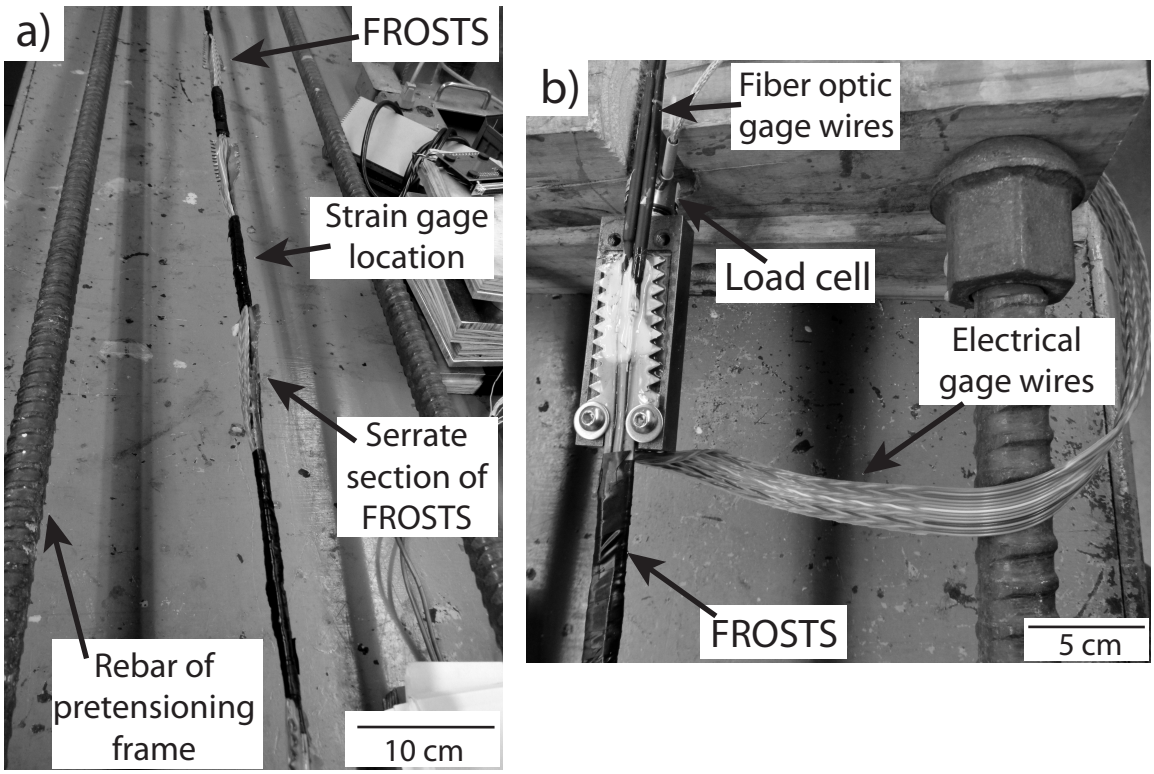

Figure 3.11. Photographs of setup for laboratory test #1: Electrical-resistance and fiber-optic strain gages and FROSTS performance. a) Photograph of FROSTS in pretesnioning frame. Fiber-optic and electrical-resistance gages are co-located along the FROSTS and covered with black tape. b) Photograph of the end of the FROSTS held in the pretensioning clamp during testing. The load cell measures the tension in the FROSTS during testing.

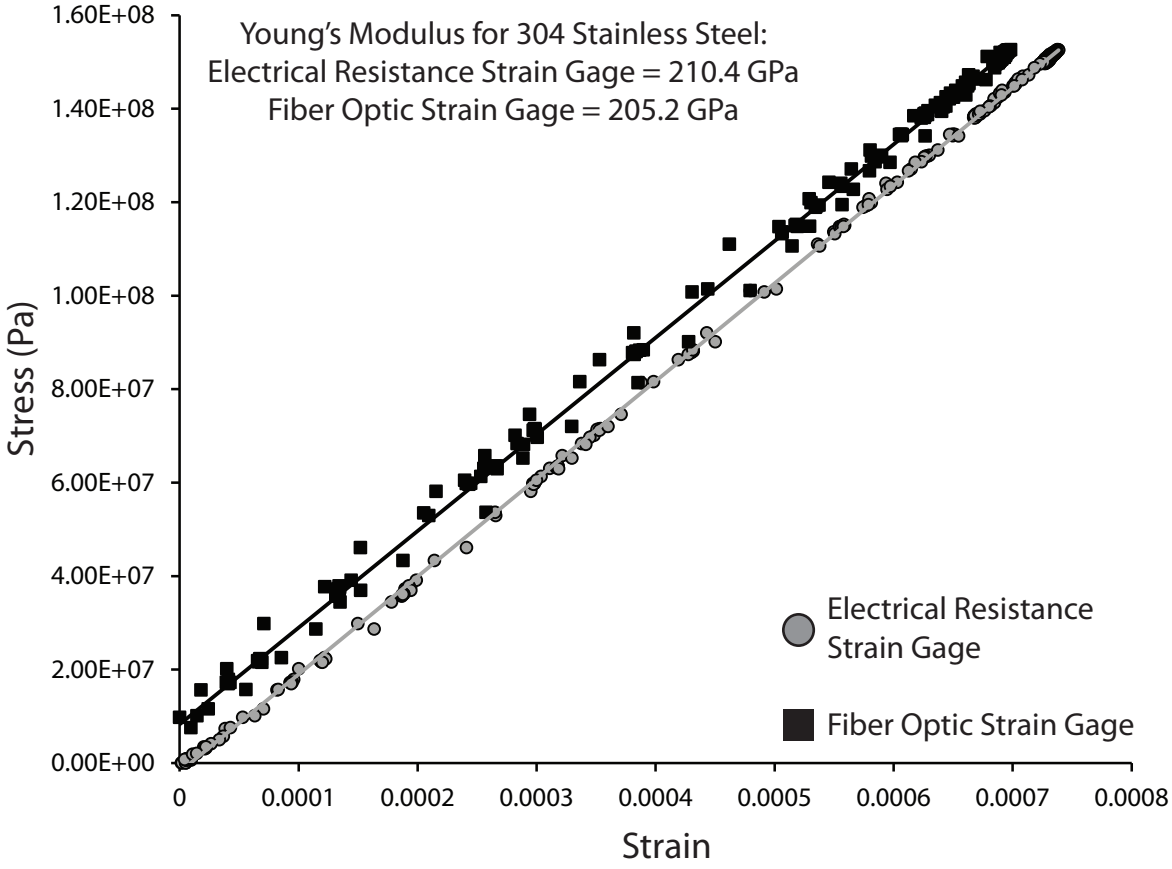

Figure 3.12. Representative data from laboratory test #1: Electrical-resistance and fiber-optic strain gages and FROSTS performance. Stress-strain data and Young's moduli for 304-stainless steel from an electrical-resistance strain gage and a fiber-optic FBG gage. The electrical-resistance and FBG gages are co-located along the FROSTS.

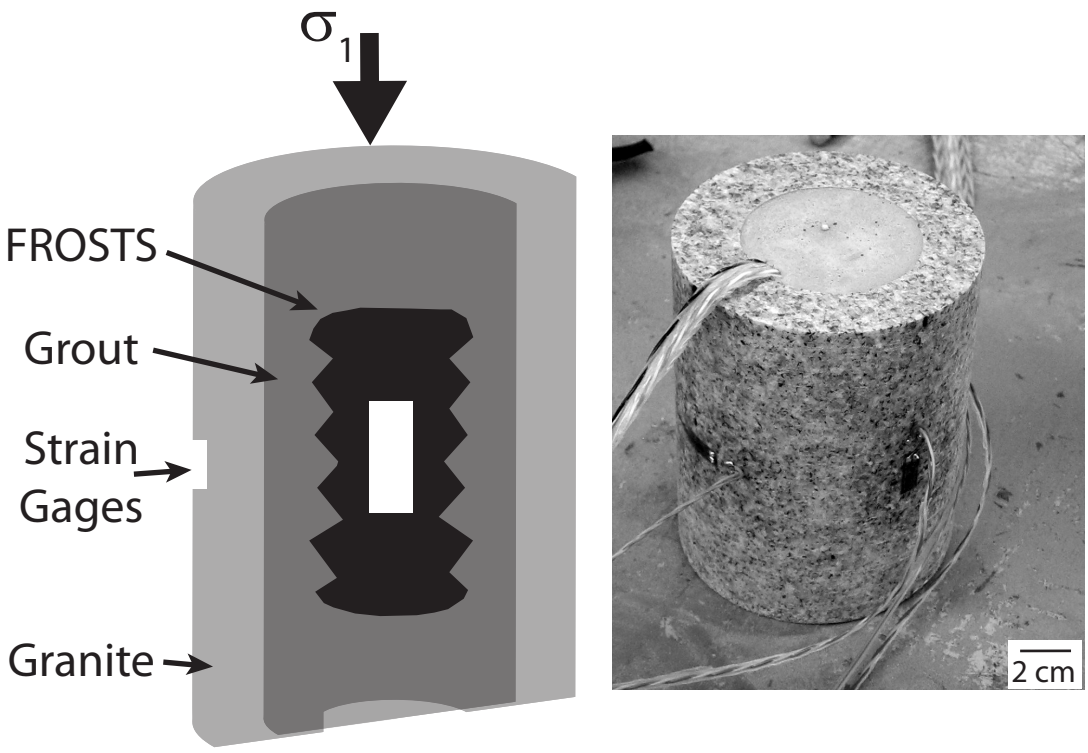

Figure 3.13. Experimental setup for laboratory test #2: FROSTS embedded in Lac du Bonnet granite. Schematic drawing of piece of FROSTS embedded in hollow granite core (left). White patches denote locations of strain gages. Photograph of laboratory sample showing strain gages on the granite. The wires coming out of the top are attached to the strain gages installed on the FROSTS.

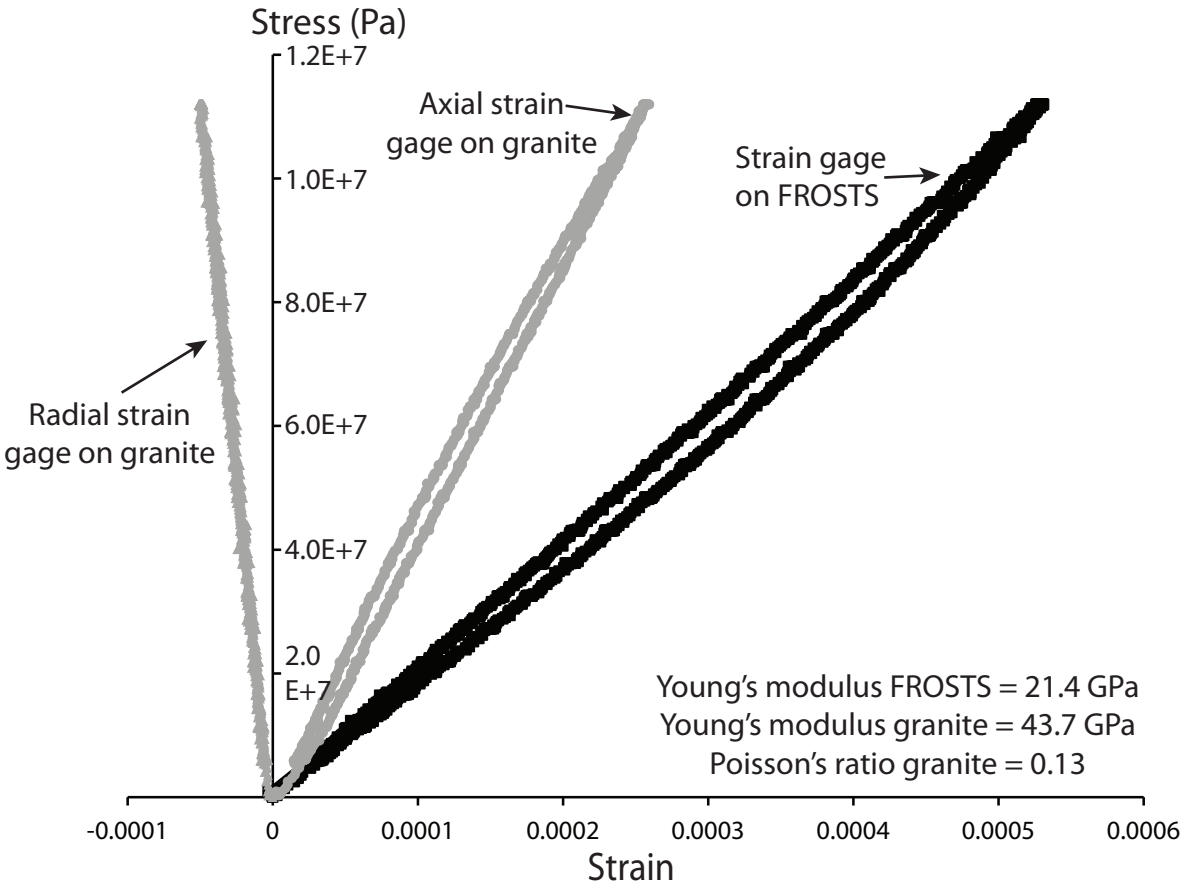

Figure 3.14. Representative stress and strain data for laboratory test #2: FROSTS embedded in Lac du Bonnet granite. Stress-strain curve for an electrical-resistance gage on the FROSTS segment (black) and stress-strain curves for axial and radial strain gages on the Lac du Bonnet granite hollow core (gray). Young's moduli for the FROSTS and granite and Poisson's ratio for the granite are noted on the graph.

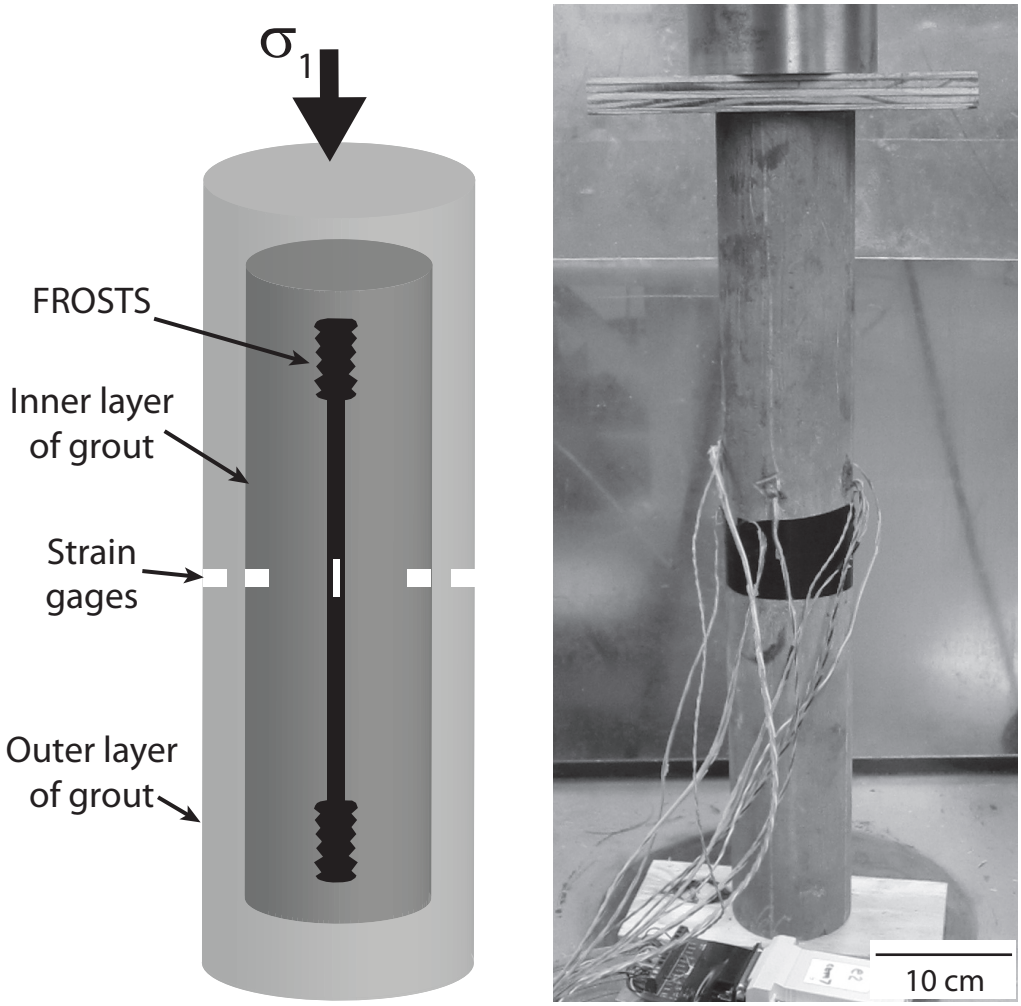

Figure 3.15. Experimental setup for laboratory test #3: FROSTS and two-step grouting procedure. Schemtic drawing of piece of FROSTS embedded in two cylinders of grout (left). White patches denote location of strain gages. Photograph of laboratory sample in load frame (right). Wires are attached to strain gages and black tape covers the strain gages on the outer layer of grout.

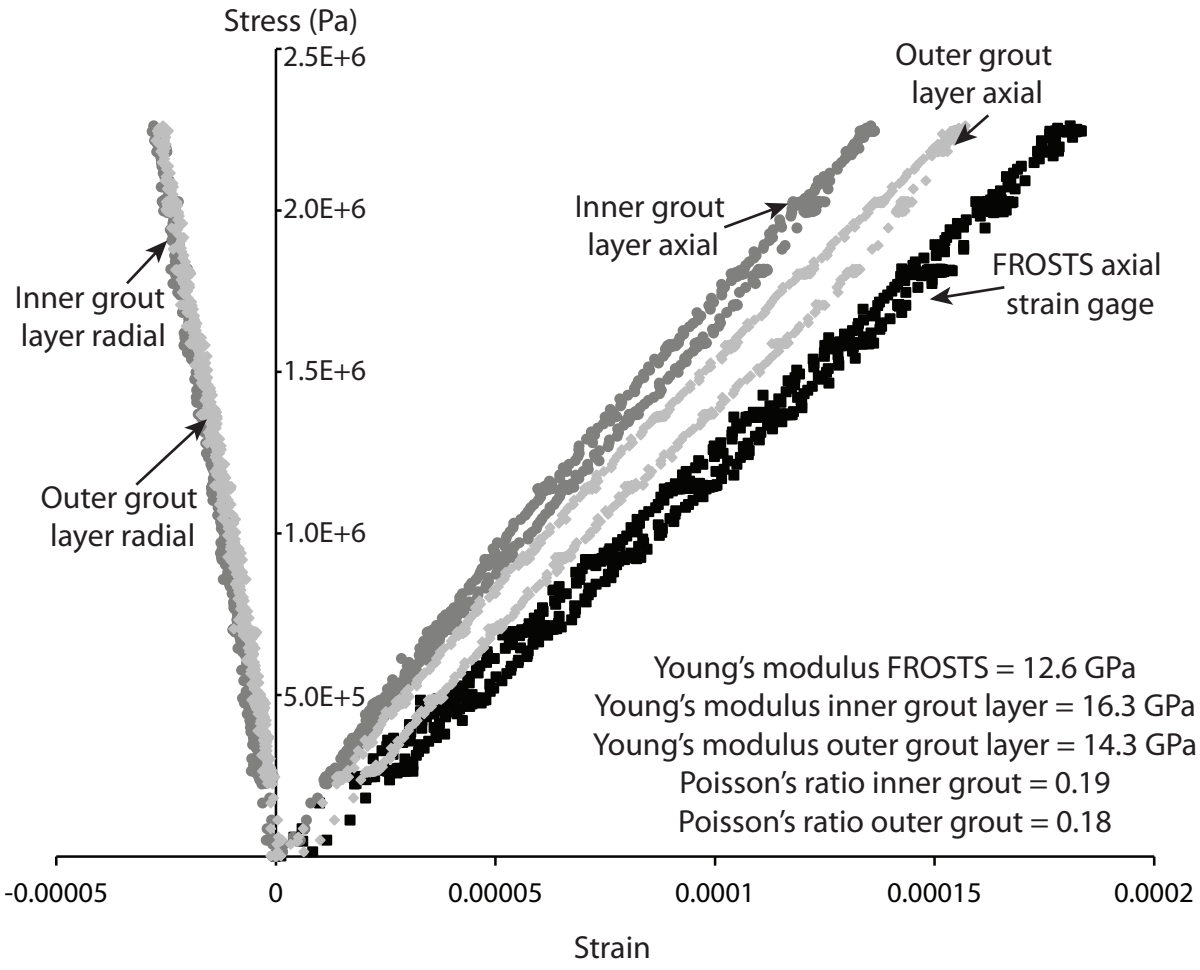

Figure 3.16. Representative stress and strain data from the laboratory test #3: FROSTS and two-step grouting procedure. Stress-strain curve for an electrical-resistance strain gage on the FROSTS segment (black) and stress-strain curves for axial and radial strain gages on the inner (dark gray) and outer (light gray) layers of grout. Young's moduli for the FROSTS and both grout layers and Poisson's ratio for both grout layers are noted on the graph.

Chapter 4: *In situ* measurements of rock mass deformability

J. R. Gage, H. F. Wang, D. O. Fratta, A. Turner

ABSTRACT

In order to examine how the mechanical properties of a rock mass vary from the centimeter to meter scale, we performed two field point-loading tests (89 kN and 890 kN) to determine the *in situ* modulus of deformation (E_m) of a rock mass. The experimental setup is analogous to plate jacking-type tests, but with a point load. The experiments were done in the Poorman formation on the 4100 level (~1250 m underground) of the Sanford Underground Research Facility (SURF) at the site of the former Homestake goldmine in Lead, SD. For comparison with *in situ* values, we also conducted laboratory mechanical tests and used two geotechnical classification systems to evaluate rock stiffness. The *in situ* modulus of deformation increases with depth into the rock mass. This increase in stiffness is a result of the differences in mechanical properties due to the effect of excavation of the underground space. Near the surface (0 – 1.2 m depth), the rock is weakened due to damage from blasting. Beyond this damaged zone is the stress-relief zone (1.2 – 1.5 m depth), where open joint sets affect rock stiffness, and beyond that lies the undisturbed zone (>1.5 m depth) where the rock is the stiffest. If done properly, *in situ* measurements of rock stiffness are a valuable tool to fully characterize the gradient in stiffness of a rock mass, which laboratory tests or geotechnical classification systems do not fully capture.

4.1 INTRODUCTION

The deformability and strength of a rock mass are the most important geotechnical variables to characterize for the construction of underground excavations in rock masses. The modulus of deformation (E_m) is one of the parameters that best represents the mechanical behavior of a rock mass. However, there is no clear consensus on the most accurate method to determine a representative modulus of deformation. There has been significant work done on this problem using three main approaches: 1) The extrapolation of laboratory mechanical tests to the field scale; 2) The development of geotechnical classification systems that incorporate laboratory results and field observations; and 3) *In situ* measurements of rock mass deformability.

The results of laboratory mechanical tests frequently cannot be used to predict the behavior of an intact rock mass. Small laboratory samples cannot capture the effect of structural heterogeneities, such as joints and fractures, on the mechanical behavior of a larger-scale rock mass (e.g. Hu and Huang, 1993; Scott et al. 1998). In addition to using laboratory measurements, several authors have also developed geotechnical classification systems to predict rock mass deformability. These classification systems incorporate field observations with the laboratory-measured rock moduli. The three main classification systems are the Rock Mass Rating (RMR) (Bieniawski, 1973), the Tunneling Quality Index (Q) (Barton et al., 1974), and the Geological Strength Index (GSI) (Hoek and Brown, 1997).

Instead of using indirect classification systems or extrapolating laboratory stiffness, it would be preferable to measure the deformability of a rock mass directly in the field. However, *in situ* deformation measurements are time consuming and expensive and often

produce inconsistent results. The reliability and accuracy of *in situ* measurements largely depend on the experimental methods and setup (Bieniawski, 1978; Hoek, 2000; Palmström and Singh, 2001). There are three main methods used to measure the *in situ* deformation modulus; they are the plate-loading test (PLT), plate-jacking test (PJT) and Goodman jack test (Palmström and Singh, 2001).

The Goodman jack test is the least reliable when compared to the PLT and PJT (Singh, 2011) primarily because of complications associated with accurately measuring the displacement of the jack's plates and modeling the applied stress field (Li and Cornet, 2004), and results typically show significant scatter because only a small volume of rock is deformed (Volger et al., 1977). Plate-loading tests can also produce unreliable results because of the difficulty in accurately measuring displacement of the surface of the rock mass (Boyle, 1992; Agharazi et al., 2012). Plate-jacking tests produce the most reliable results because the embedded extensometers allow strain to be measured at depth within the rock mass and hopefully beyond any damaged zone surrounding the opening (Ribacchi, 1988).

Although the database of *in situ* modulus of deformation measurements is not extensive, many authors have tried to correlate the *in situ* measurements with the geotechnical classifications systems. Both the RMR and GSI systems can be linked to *in situ* measurements with reasonable reliability (Palmström and Singh, 2001; Hoek and Diederichs, 2006). Other authors suggest that it is important to integrate field observations of joints, weathering and general rock mass character with any geotechnical classification scheme and *in situ* measurements (Bieniawski, 1978; Serafim and Pereira, 1983; Gokceoglu et al., 2003). Without a well-defined and agreed upon method to predict the behavior of a rock mass during

deformation, it is important to continue to critically evaluate both experimental methods and classification techniques and continue to examine how the mechanical properties of rock vary over spatial scales.

In this paper we present the results of two point-loading tests performed ~1250 m underground in a quartz and mica-rich amphibolite. We applied both a 98 kN (10 ton) and 980 kN (100 ton) point load to the rock surface, and utilized a dense array of fiber-optic sensors to measure strain at depth in the intact rock mass (Gage et al., 2010; Gage et al., 2011). The resulting *in situ* moduli of deformation (E_m) are compared to laboratory measurements of Young's modulus and stiffness estimates from geotechnical classification systems, which allows us to examine how the mechanical properties of the rock vary from the centimeter to the meter scale. We also discuss several important experimental considerations to improve future *in situ* rock deformability measurements.

4.2 GEOLOGIC BACKGROUND

Our loading tests take place at the Sanford Underground Research Facility (SURF) at the site of the former Homestake gold mine in Lead, SD. SURF is an underground laboratory that will house physics experiments as well as provide some space for underground biology, geology, and engineering research (Kramer, 2011). In conjunction with the South Dakota Science and Technology Authority (SDSTA) and the Department of Energy (DOE), the Homestake gold mine is being converted to SURF. When mining stopped in 2002, the Homestake gold mine was the largest and deepest (>8,000 ft.; ~2,500 m) gold mine in North America.

SURF is located in the northern Black Hills of South Dakota (Fig. 4.1). The area was subjected to several episodes of tectonism during the Precambrian, resulting in metamorphism, foliation development, complex folding, shear zones, and the emplacement of dikes and veins (Dahl et al., 1999). Fluid influx during Precambrian deformation and metamorphism produced economic gold deposits along the structures (Nabelek et al., 1999). Uplift during the Laramide orogeny caused brittle deformation in the area of SURF (Lisenbee and DeWitt, 1993) and created several joint sets and brittle faults. Our experiment is located in the Precambrian Poorman formation, which consists of metamorphosed tholeiitic basalt and metasedimentary rocks (Harder and Noble, 1948). In the area of our strain sensors, the Poorman formation is a strongly foliated and lineated amphibolite-grade mica schist with several quartz veins, vein arrays, and joint sets oriented obliquely to the strain sensor array (Gage et al., 2010).

4.3 POINT-LOADING TESTS

4.3.1 Strain sensor array

We have installed a dense array of Fiber Bragg Grating (FBG) fiber-optic strain and temperature sensors on the 4100 level of SURF in an alcove measuring 2 m deep by 3 m wide and 2 m tall. Gage at al. (2010) and Gage et al. (2011) provide a detailed discussion of the sensor array. For this experiment, we primarily used the sensors embedded in the ceiling of the alcove, which were grouted into vertically oriented boreholes. These fiber-optic strain sensors measure one-dimensional shortening or elongation in the vertical direction, and are accurate to 1 με and 0.1 °C.

There are two types of fiber-optic strain sensors embedded in the ceiling of the alcove. First, there is a Micron Optics Inc. OS3600 temperature compensated strain gage. This gage consists of an FBG strain gage anchored between two metal disks (5 cm diameter) and surrounded by a 1.5 cm diameter Teflon tube (Fig. 4.2). The gage length of the OS3600 sensor is 25.4 cm. The near-edge of the OS3600 is 32 cm from the surface of the rock mass. The OS3600 sensor is grouted into a ~9 cm (3.5 in.) diameter borehole.

Also embedded in the roof of the alcove is a Fiber-optically Instrumented Rock Strain and Temperature Strip, or FROSTS (Gage et al., 2011). FROSTS are *in situ* strain measuring tools that are ~183 cm (6 ft.) long and have six strain and temperature sensors installed at 30 cm intervals along its length. The strain gages are installed in the center of the 10 cm long sections of the FROSTS that are separated by wider serrated sections (Signer and Sunderman, 2003; Gage et al., 2011) (Fig. 4.3). The ridges on the serrated sections grip the grout that embeds the FROSTS in the rock mass and divide the FROSTS into six discrete sections that measure strain independently along the FROSTS length. The FBG gages on each of the six sections of the FROSTS should measure the average strain between the two serrated sections on either end.

The FROSTS use Micron Optics Inc. OS3200 strain gages and OS4310 absolute temperature sensors. The OS3200 strain gages have a gage length of 1.0 cm. The FROSTS was pretensioned prior to installation (cf. Gage et al., 2011), which allows the tool to measure the shortening strains associated with the point-loading tests. The near-end of the FROSTS is 45 cm from the surface. The FROSTS was grouted into a ~7 cm (2.75 in.) diameter borehole.

4.3.2 Stress during point-loading tests

In order to determine the *in situ* modulus of deformation (E_m) for the rock mass, the surface load must be extrapolated into the rock mass to determine the stress at each sensor location. Because only the embedded sensor nearest the applied load measured strain during the loading cycles of the 890 kN test, we can assume that the shape of the alcove and edge effects of nearby walls do not affect the stress field. Thus, we can treat the experiment as a point load on a semi-infinite half space and utilize a Boussinesq solution to determine the vertical stress (σ_{zz}) within the rock mass at the sensor locations, which is:

$$\sigma_{zz} = (Q/(2\pi)) * ((3Z^3)/R^5) \quad (4.1)$$

where Q is the applied load, z is the vertical distance from the surface to the sensor, and R is the distance from the load to the sensor (Davis and Selvadurai, 1996).

4.3.3 89 kN (10 ton) point-loading test

In order to measure the *in situ* modulus of deformation (E_m) with the embedded strain sensors, we performed two point-loading tests, which are analogous to plate-jacking tests (PJT) (Palmström and Singh, 2001). The major difference between our point-loading tests and traditional PJTs, is that we apply a point load directly to the rock mass instead of a load distributed across a plate.

For the first experiment, we used two 89 kN (10 ton) capacity hydraulic rams to apply a load between the floor and ceiling of the alcove (Fig. 4.4). The rams were Strata Products Inc. Rocprops, which are portable roof supports used primarily in coal mines. The Rocprops

are able to apply a 10 ton pre-stress to the rock mass using 1,000 psi hydraulic pressure. The tops of the Rocprops are hemispherical, and they were placed directly against the rock mass, thus applying an 89 kN point force. Each of the two Rockprops was placed near one of the two sensors (FROSTS and OS3600) embedded in the ceiling of the alcove (Fig. 4.5). We performed five loading cycles holding the maximum load on the rock mass for between five and twenty minutes during each cycle.

4.3.3.1 Results: 89 kN (10 ton) point-loading test

For the 89 kN test, the stress decreases along the FROSTS from 0.024 MPa at the FROSTS sensor closest to the surface of the rock mass (sensor A) to 0.008 MPa at the deepest sensor (sensor F) (Table 4.1). The stress at the embedded OS3600 is 0.016 MPa (Table 4.1). The stress-strain curves during loading are linear for each sensor that recorded measurable strain.

In general, the 89 kN load is too small to induce substantial strain in either the FROSTS or the embedded OS3600 sensor (Fig. 4.6). The embedded OS3600 measures ~2 με during each 89 kN loading cycle. On the FROSTS, sensor A, closest to the surface, also measures 2 με for each loading cycle. Sensors E and F, deepest in the rock mass, do not measure any strain, except in loading cycle # 3 (Fig. 4.6 and Table 4.1). All deformation measured during the 89 kN loading test by the FROSTS is near or below the 1 με resolution of the sensors. However, the recorded changes in strain correlate temporally to the application and removal of the load, which suggests that the measured strain is a result of the loading experiment.

Using the stress determined by the Boussinesq solution and the measured strain at each sensor along the FROSTS, we can calculate the modulus of deformation for the rock mass. For sensor A, at a depth of 0.62 m in the rock mass, E_m = 12.1 GPa. For the four sensors on the FROSTS that recorded strain during the test, the E_m increases with depth (Table 4.1). The modulus of deformation increases by ~7.3% for each sensor (Table 4.1). The OS3600 sensor, at a depth of 0.5 m in the rock mass, records an E_m = 8.1 GPa.

4.3.4 890 kN (100 ton) point-loading test

In order to induce larger strains in the rock mass, we performed a second point-loading test using an 890 kN (100 ton) hydraulic ram on the rock mass. The experimental set up is similar to the 89 kN loading test. For the 890 kN test, we used a single load that consisted of a specially machined steel column atop a 100 ton capacity hydraulic cylinder (Fig. 4.7a). The steel column had a rounded head to apply a point load to the rock mass (Fig. 4.7b). We loaded the rock mass in two different locations near our embedded strain sensors (Fig. 4.5). An 89 kN load was held on the rock mass continuously so that the steel column would not lose contact with the rock and become misaligned. In the first location, we performed four loading cycles from 89 kN to 890 kN. The maximum load was held on the rock mass for 10 minutes during each cycle. At the second location, we performed three loading cycles holding the maximum load on the rock mass for ten minutes during each cycle.

4.3.4.1 Results: 890 kN (100 ton) point-loading test

For the 890 kN experiment, at the first loading location, the stress decreases from 0.218 MPa at sensor A to 0.071 MPa at the deepest sensor (Table 4.2). The stress at the embedded OS3600 is 0.016 MPa. For the second loading location, the stress along the

FROSTS is 0.035 MPa at sensor A and 0.012 at sensor F. The stress at the embedded OS3600 is 0.571 MPa.

For the first loading location, the FROSTS records a clear gradient of decreasing strain into the rock mass (Fig. 4.8). The strain magnitude at each sensor on the FROSTS is above the resolution of the fiber-optic sensor. The sensor closest to the surface records approximately 6 με more than the deepest sensors in the rock mass (Table 4.2). The embedded OS3600 sensor does not record any statistically significant strain during the loading cycles at the first location (Fig. 4.8). For the 890 kN loading test at the first loading location, E_m for sensor A on the FROSTS is 28.7 GPa. The modulus of deforamtion increases with depth into the rock mass by ~18% for each sensor (Table 4.2). Sensor F at 2.14 m in the rock mass has an E_m of 65.1 GPa. The stress-strain curves during loading are linear for each sensor along the FROSTS and the OS3600 (Fig. 4.9). Also, the slope of the stress-strain curve for each sensor is unique, and is similar in magnitude to the modulus of deformation determined for each sensor from the average maximum strain for all four loading cycles (Fig. 4.9 and Table 4.2).

For the second loading location, the embedded OS3600 records an average of 12.7 με for the three loading cycles (Fig. 4.8). The FROSTS does not record any significant strain response during the loading cycles at the second location. Sensors C, D, E, and F show some strain response (Fig. 4.8), but the discrete loading events are indiscernible, and thus cannot be accurately analyzed. For the 890 kN loading test at the second location, the E_m measured by the embedded OS3600 sensor is 45.2 GPa.

4.4 LABORATORY MECHANICAL TESTING

We tested a total of six samples from a specimen of the Poorman formation collected in the sensor alcove on the 4100 level of SURF. Three samples were cored perpendicular to foliation and three were cored parallel. Each sample was 2.5 cm in diameter and 5 cm tall. The sample preparation and laboratory testing followed ASTM D702-10. Each sample had four electrical resistance strain gages installed on it with two strain gages oriented axially and two radially. The gages were Micro-Measurements CEA-06-250UW-120 foil strain gages installed with M-Bond 200 epoxy. The samples were unconfined and loaded until failure.

4.4.1 Results: Laboratory mechanical testing

The average Young's modulus for the Poorman formation perpendicular to foliation is 43.5 GPa and the average Poisson's ratio is 0.23 in the linear range of the stress-strain curve between 10 and 100 MPa (Fig. 4.10). For samples cored parallel to foliation, Young's modulus is 53.7 GPa, and Poisson's ratio is 0.16 in the linear range of the stress-strain curve between 10 and 100 MPa (Table 4.3). The average Young's modulus and average Poisson's ratio from each strain gage pair on individual samples are relatively consistent; however, for the parallel orientation, there is significant scatter in the data among samples (standard deviation = 11.9 GPa). The stress-strain curves for each sample are generally linear after ~10 MPa until failure (Fig. 4.10).

Because the load was applied obliquely to foliation during the point-loading tests, the mechanical properties of the rock are likely somewhere between the measured end members (Donath, 1961). The foliation dips 50° in the alcove; therefore following the construction of Nye (1957), the laboratory value for Young's modulus at 50° to foliation is approximately

50.8 GPa. These values are consistent with those measured by Johnson et al. (1993) for the Poorman formation and higher than those measured by Pariseau et al. (1987).

4.5 ROCK MASS GEOTECHNICAL CLASSIFICATION

Detailed field descriptions of the Poorman formation in the area of the sensor installation were completed in order to determine the geotechnical strength classification for comparison to laboratory and *in situ* results. The Poorman formation is an amphibolite-grade schist that contains visible quartz, muscovite, and garnet. It has a well-developed foliation that is often mineralized with pyrite and chalcopyrite. The most prominent joint set (J_1) in the alcove is parallel to the foliation, and it is oriented 044/50 SE (Fig. 4.11). There are several sets of quartz veins from 0.2 cm to 10 cm thick that are oblique to foliation. Some of the quartz veins also have sulfide mineralization.

In addition to foliation-parallel joints, the experiment alcove contains three other joint sets (Fig. 4.11). The two more prominent joint sets (J_2 and J_3) are, in general, steeply dipping and cut obliquely though the alcove. J_4 is less prominent than J_1, J_2, and J_3; it is moderately dipping and oblique to foliation. J_2 is oriented 161/86 W and J_3 is 075/87 SE. The sub-vertical joint sets (J_2 and J_3) are not mineralized. J_4 is oriented 205/39 NW. The joint spacing in the Poorman formation in the alcove is 0.3 m. In general, joint aperture is less than 1 mm, and the joint surfaces are slightly rough. The rock surface is completely dry and no groundwater is observed.

Using the Rock Mass Rating (RMR) classification scheme of Bieniawski (1973) the Poorman formation in the experiment alcove has a rating of 74 (good). On the 2.1 km (6950 ft.) level of the Homestake mine, the Poorman formation was determined to have a RMR of

70 (Pariseau et al., 1987 and Tesarik et al. 2002). It is important to note that we did not have access to core from the Poorman formation, so we used the Rock Quality Designation (RQD) parameter from Golder's analyses (Golder, 2006) where RQD = 75% for our RMR classification. Using the Geological Strength Index (GSI) classification of Hoek and Brown (1997), the Poorman formation has a rating of 80.

4.6 DISCUSSION

4.6.1 Comparison of *in situ* and laboratory deformability results

A major criticism of *in situ* measurements of the modulus of deformation is that the results are generally unreliable. Field measurements typically produce results that are significantly lower than the actual stiffness of the rock mass. For example, *in situ* modulus of deformation measurements of sandstones and siltstones at the Mingtan pumped storage site in Taiwan were up to 90% more compliant than laboratory-determined Young's moduli measurements (Hoek, 2000). However, much of this inaccuracy can be eliminated by proper *in situ* testing methodology (Palmström and Singh, 2001). Different types of *in situ* tests (plate-jacking, plate-loading, Goodman jack, etc.) give significantly different results for the same rock mass (Bieniawski, 1978; Heuze and Amadei, 1985). Plate-jacking tests produce the most accurate and reliable results, and should be the method of choice (Benson, 1970; Palmström and Singh, 2001).

Both our 89 kN and 890 kN point-loading tests are analogous to plate-jacking tests; however the 89 kN and 890 kN tests yielded significantly different results for the modulus of deformation for the Poorman formation. For the 89 kN, E_m = 12.1 GPa at sensor A at a stress of 0.024 MPa, and for the 890 kN experiment E_m = 28.7 GPa at sensor A at a stress of 0.218

MPa. A similar relationship is seen for sensors B-D on the FROSTS and the OS3600 (Table 4.1 and 4.2). The rock mass appears significantly more compliant when a small load is applied. This is likely caused by the closure of fractures and microcracks in the damaged zone surrounding the experiment alcove (Farmer and Kemeny, 1992). The data from the 890 kN test is more robust than the 89 kN test because all the sensors along the FROSTS measured strain and all the recorded strain was above the resolution of the FROSTS. If the 890 kN test, were not performed, the *in situ* modulus of deformation values would appear significantly lower. Thus, in *in situ* experiments, it is important to use a load that is sufficiently large to induce significant strain in the rock mass. It is possible that load magnitude contributed to the anomalously low E_m values reported in some previous *in situ* tests (Hoek, 2000; Palmström and Singh, 2001; Hoek and Diederichs, 2006).

The laboratory value for Young's modulus for the Poorman formation of 50.8 GPa is in similar to the *in situ* modulus of deformation values measured for the 890 kN experiment. Using the relationship of E_m and depth, the laboratory value would correspond to the E_m at ~1.2 m depth in the rock mass (Fig. 4.12). The results of the 89 kN test significantly underestimate E_m for the rock mass because the applied load was too small to close the open fractures in the rock mass surrounding the alcove (Table 4.2). By using a point-loading test setup and applying a significantly large load, we have improved the results of the *in situ* experiments and closely approximated the laboratory-measured value.

4.6.2 Comparison of *in situ* rock mass deformability and empirical estimations from geotechnical classification systems

Many studies have tried to develop empirical methods for determining a representative modulus of deformation of a rock mass using the results of the RMR and GSI classification systems (for reviews see Palmström and Singh, 2001 and Hoek and Diederichs, 2006). Both Bieniawski (1978) and Serafim and Periera (1983) determined empirical relationships producing E_m from the RMR classification of a rock mass. For rock masses with an RMR > 55, Bieniawski's (1978) relationship has been shown to be more accurate (Palmström and Singh, 2001). For the Poorman formation, where RMR = 74, E_m = 48 GPa. This is equivalent to the E_m measured at ~1 m depth in the rock mass during our 890 kN loading experiment, and is similar to the laboratory results.

The empirical relationship developed by Hoek and Diederichs (2006) uses the GSI classification and the disturbance factor (D) (Hoek et al., 2002). The disturbance factor is an attempt to quantify the effect of the damaged zone on the results of *in situ* deformability measurements. The damaged zone is the volume of rock surrounding an underground space that has been damaged due to excavation of the opening from blasting or boring (Palmström and Singh, 2001). Rock damage due to blasting significantly decreases the measured deformation modulus of a rock mass (Singh and Rajvansi 1996; Singh and Bhasin, 1996). The size of the damage zone is dependent on several variables such as the rock properties, amount of explosive used, and distance between blast holes (Olsson and Bergqvist, 1997), and thus is very difficult to quantify (Hoek and Diederichs, 2006).

The increase of rock stiffness and E_m with depth in the rock mass is a result of the transition from the damaged rock surrounding the alcove to the undisturbed rock mass (Palmström and Singh, 2001). Using the relationship in equation 2 from Hoek and Diederichs (2006) with different values for D (the disturbance factor; see Hoek et al., 2002), we can quantify the damaged zone around the experiment alcove. The equation is:

$$E_m = 100{,}000\ [(1-D/2) / (1+e^{((75+2D-GSI)/11)}] \quad (4.2)$$

where D is the disturbance factor, and GSI is the Geological Strength Index. At the depth of sensor A (0.62 m) D = 0.44. At D= 0, E_m = 61.2 GPa, which corresponds to a depth of ~1.5 m in the intact rock mass (Table 4.4). Thus, in the Poorman formation on the 1250 m level of SURF, the damaged zone extends ~1.5 m deep. Previous studies suggest that the damage zone in a relatively competent rock only extends up to 0.5 m (Sharma et al., 1989).

The transition from the damaged zone into the intact rock mass is gradual (Palmström and Singh, 2001); thus it is useful to record a detailed strain gradient during *in situ* testing. FROSTS are an ideal monitoring tool because they can be embedded through the length of the damage zone and used to document the change in rock properties with depth (Table 4.4). For example, the six strain gages along the FROSTS allow for the accurate characterization of the damaged zone, whereas the OS3600 only provides one E_m measurement. Thus, embedded multipoint borehole extensometers (such as FROSTS) are superior to single-point borehole extensometers for producing reliable *in situ* deformation modulus results.

The stiffness profile provided by the FROSTS during the 890 kN point-loading test shows that the rate of increase of the modulus of deformation varies with depth. The plot of *in situ* deformation modulus and depth in the rock mass has two distinct data populations (Fig.

4.12). Sensors A-C on the FROSTS measure a relatively compliant modulus, and have a steep slope (Fig. 4.12), which shows that the stiffness of the rock mass increases quickly in the damaged zone. Sensors D-F on the FROSTS measure stiffer moduli and have a shallow slope (Fig. 4.11), which suggests that, in the undisturbed zone, the deformation modulus of the rock mass asymptotically approaches a stable value. The change in slope also appears to occur in the stress-relief zone.

An alternate explanation for the apparent increase in stiffness with depth is that the strain measurements on the FROSTS occur at different initial stress levels along a nonlinear stress-strain curve. Each strain gage on the FROSTS is located at a different regional stress. Stress-strain curves are often nonlinear, especially at low stresses (Goodman. 1989), and the apparent Young's modulus becomes stiffer as the applied load increases. The stress-strain curves measured in the laboratory (Section 4.4; Fig. 4.10) are nonlinear below ~10 MPa. Thus, it is possible that the trend of increasing stiffness with depth is a result of the strain gages being at different initial stress states before the point-loading experiment.

The vertical regional stress (σ_v) at each strain gage location along the FROSTS was determined using the Kirsch solution and the *in situ* stress relationships of Pariseau (1985) (Table 4.5). Strain gages C-F are at nonzero stresses before loading (Table 4.5). It is not possible to correct for the effect of the nonlinear stress-strain curve of the rock on the modulus of deformation. However, strain gages A and B on the FROSTS do not have any initial stress and still record the increase with stiffness. Fractures in the damage zone surrounding the alcove are likely the dominant cause of the observed variation in modulus (Singh and Rajvansi 1996), and he fracture density should decrease with depth away from the

opening (Palmström and Singh, 2001). Thus, it is likely that increase in rock stiffness is primarily a result of the actual variation of rock properties with depth and only slightly affected by the initial stress state of the individual strain gages.

The FROSTS and OS3600 also record significantly different values for the modulus of deformation during both the 89 kN and 890 kN loading experiments. The OS3600 is 0.5 m deep in the rock mass and records an E_m = 45.2 GPa, whereas sensor A on the FROSTS records an E_m = 28.7 GPa at 0.62 m during the 890 kN experiment. This discrepancy could be due to the construction of the FROSTS and OS3600 sensors. The materials of the gages' packaging are different, which create contrasting mechanical properties of the gages and affect the way each measures strain (e.g. Littlejohn, 1993; Signer and Sunderman, 2003). Thus, it is important to understand the mechanical properties of the extensometers. The coupling between the sensors and the rock mass could also create the differences between the FROSTS and OS3600, since the sensors have different anchoring mechanisms. Alternatively, sensor A on the FROSTS and the OS3600 were deformed at different stresses during the point-loading tests, and the different deformation moduli might be a result of the non-linearity of the Poorman formation's stress-strain curve at low stresses (Fig. 4.10); however, the stress-strain curves observed in the 890 kN point-loading test are linear for the applied stresses.

4.6.3 Scale and the mechanical properties of rock

Discontinuities in a rock mass (e.g. fractures, joints, and faults) are the biggest influence on rock stiffness when moving from small-scale laboratory results to the m^3-scale of an underground excavation (such as the experiment alcove). In our work, the laboratory value for the Young's modulus of the Poorman formation is 50.8 GPa, which corresponds to a depth

of ~1.2 m as measured by the 890 kN point-loading experiment (Table 4.2). The meter-scale rock mass contains two main types of fractures that influence both its mechanical behavior and deformation modulus. First, fractures created during blasting weaken the rock mass (Singh and Rajvansi 1996; Singh and Bhasin, 1996). The stiffness of the damaged zone surrounding an excavation (up to the first 1.2 m, as measured in the 890 kN experiment) is lower than the laboratory measured results.

Second, fractures that are structural features of the rock mass (e.g. pervasive joint sets) also influence how the larger scale rock mass behaves (e.g. Dalgic, 2002). Beyond the damaged zone is an area where rock stiffness increases (Table 4.2). This zone is close enough to the free surface of the excavation that some stress is relieved, causing opening of the joint sets (Peila, 1994). At this depth in the Poorman formation (between ~1.2 – 1.5 m), the rock has a similar stiffness to the Young's modulus measured in the laboratory.

As depth into the rock mass increases (>1.5 m) the rock mass is stiffer than laboratory values (Table 4.2), this represents the undisturbed intact rock mass where it behaves as massive, unjointed rock mass (Palmström and Singh, 2001). The size and extent of these zones will vary significantly by rock type. Also, the degree to which laboratory measurements will approximate the mechanical properties of the stress-relived zone depends on joint configurations (Kulatilake et al., 1993; Kulatilake et al., 1997).

The stiffness of a rock mass is complex and a single measurement will not characterize its deformation behavior. The three documented zones (damaged zone, stress-relief zone, and undisturbed zone) all have different implications for underground openings. Near-surface rock stiffness in the damaged zone will influence the required ground control as

well as the potential for surface failure hazards. The deeper undisturbed rock stiffness will determine the size, orientation, depth, and construction methods of the openings (Aydan et al., 1997). This stiffness gradient in an intact rock mass is important on the larger scale and cannot be captured by a single laboratory value. Thus, *in situ* testing using an embedded multipoint borehole extensometer (such as the FROSTS), allows for the characterization of the different zones of rock behavior and provides a fuller understanding of rock mass deformability on the m^3-scale.

4.7 CONCLUSIONS

1) When performing *in situ* rock mass deformability tests, the experimental design is critical to attaining reliable results. Using a plate jacking-type test with significant load (e.g. our point-loading tests) and embedded multipoint borehole extensometers (such as FROSTS) produces the most robust results.

2) A multipoint borehole extensometer allows for the quantification of the damaged zone around an underground opening, which provides the most accurate *in situ* deformation moduli results.

3) Laboratory results, *in situ* tests, and empirical relationships give similar, but not the same results for the E_m of the Poorman formation. However, no single value of E_m accurately describes the behavior of a large intact rock mass.

4) The rock mass surrounding an underground excavation has three zones with different mechanical properties: the damaged zone, the stress-relief zone, and the undisturbed zone. The transition between these zones is gradual, but it is important to characterize rock deformability along this gradient to accurately understand rock mass behavior for excavation.

4.8 ACKNOWLEDGMENTS

This work was supported by National Science Foundation grant # CMMI-0900351. The authors wish to thank the South Dakota Science and Technology Authority especially Jaret Heise, Tom Trancynger, Wedny Zawada, Luke Scott, and Pat Kinghorn for logistical support during the loading experiments. We are also grateful to Neal Lord for laboratory support and assistance, Rory Holland and the Physical Science Laboratory at UW-Madison for building the steel post for the 890 kN point-loading experiment, Steve Gabriel (Spearfish Schools), Rich Barry (Crazy Horse Memorial), and Kevin Hachmeister (Golder Associates) for assistance in the field. Strata Products generously donated the two Rocprops used in the 89 kN point-loading test. We thank May MacLaughlin for collaboration on sensor installation and John Kemeny for discussion and development of ideas for the point-loading tests.

References

Agharazi, A., Tannant, D.D., and Martin, C.D. (2012) Characterizing rock mass deformation during plate load test at Bakhtiary dam project. *International Journal of Rock Mechanics & Mining Sciences*. 49: 1-11.

Aydan, O., Ulusay, R., and Kawamoto, T. (1997) Assessment of rock mass strength for underground excavations. *International Journal of Rock Mechanics & Mining Sciences*. 34: 1-18.

Barton, N., Lien, R., and Lunde, J. (1974) Engineering Classification of rock masses for the design of tunnel support. *Rock Mechanics*. 6: 189-236.

Benson, R.P., Murphy, D.K., and McCreath, D.R. (1970) Modulus testing of rock at the Churchill Falls underground powerhouse, Labrador. Determination of the *in situ* Modulus Deformation of Rock, *ASTM STP 477*, pp. 89-116.

Bieniawski, Z.T. (1973) Engineering Classification of rock masses. *Transactions of the Society of African Institute for Civil Engineers*. 15: 335-344.

Bieniawski, Z.T. (1978) Determining rock mass deformability: Experience from case histories. *International Journal of Rock Mechanics, Mining Sciences, & Geomechanics Abstracts*. 15: 237-247.

Boyle, W.J. (1992) Interpretation of plate load test data. *International Journal of Rock Mechanics, Mining Sciences, & Geomechanics Abstracts*. 29: 133-141.

Dahl, P.S., Holm, D.K., Gardner, E.T., Hubacher, .FA., and Foland, K.A. (1999) New constraints on the timing of Early Proterozoic tectonism in the Black Hills (South Dakota), with implications for docking of the Wyoming Province with Laurentia. *Geology.* 111:1335-1349.

Dalgic, S. (2002) A comparison of predicted and actual tunnel behavior in the Instanbul Metro, Turkey. Engineering Geology. 63: 69-82.

Davis, R.O. and Selvadurai, A.P.S. (1996) *Elasticity and Geomechanics*. Cambridge University Press. p. 76-111.

Donath, F.A. (1961) Experimental study of shear failure in isotropic rocks. *Geological Society of America Bulletin*. 72: 985-990.

Farmer, I.W. and Kemeny, J.M. (1992) Deficiencies in rock test data. *Proceedings of the International Conference of Eurock*. Thomas Telford, London, pp. 298-303.

Gage, J.R., Noni, N., Turner, A., MacLaughlin, M., and Wang, H.F. (2010) Fiber optic strain and temperature monitoring in crystalline rock at the Sanford Underground Science and Engineering Laboratory (SUSEL), Lead, South Dakota, *44th U. S. Rock Mechanics Symposium and 5th U.S- Canadian Rock Mechanics Symposium*, *Salt Lake City, 27 – 30 June.* 8 pp.

Gage, J.R., Wang, H.F., MacLaughlin, M., Turner, A., and Fratta, D. (2011) A new method for measuring in situ strain in intact rock masses: Fiber optically instrumented rock strain and temperature strips (FROSTS). *45th US Rock Mechanics Symposium, San Francisco, CA June 26-29*. 10 pp.

Gokceoglu, C., Sonmez, H., and Kayabasi, A. (2003) Predicting the deformation moduli of rock masses. *International Journal of Rock Mechanics & Mining Sciences*. 40: 701-710.

Golder Associates Ltd. (2006) Geotechnical Analyses of Proposed Laboratory Excavations at the Former Homestake Mine Lead, South Dakota. *Technical Report 06-1117-014 to Lawrence Berkeley Laboratory (May 2006).*

Goodman, R.E. (1989) *Introduction to Rock Mechanics*, second edition. New York: John Wiley & Sons: p.179-218.

Harder, J.A. and Noble, .JO. (1948) Stratigraphy and metamorphism in a part of the northern Black Hills and the Homestake mine, Lead, South Dakota. *Geological Society of America Bulletin*. 59: 941-976.

Heuze, F.E. and Amadei, B. (1985) The NX-borehole jack: A lesson in trials and errors. *International Journal of Rock Mechanics, Mining Sciences & Geomechanics Abstracts*. 22: 105-112.

Hoek E. (2000) *Practical rock engineering*. Available online: www.rocscience.com, Chapter 13; 29 pp.

Hoek, E. and Brown, E.T. (1997) Practical estimates of rock mass strength. *International Journal of Rock Mechanics & Mining Sciences*. 34: 1165-1186.

Hoek, E., Caranza-Torres, C.T., and Corcum, B. (2002) Hoek–Brown failure criterion- 2002 edition. *In: Bawden HRW, Curran J, Telsenicki M (eds) Proceedings of the North American Rock Mechanics Society (NARMS-TAC 2002). Mining Innovation and Technology, Toronto*. 267–273.

Hoek, E. and Diederichs, M.S. (2006) Empirical Estimation of rock mass modulus. *International Journal of Rock Mechanics & Mining Sciences*. 43: 203-215.

Hu, K.X. and Huang, Y. (1993) Estimation of the elastic properties of fractures rock masses. *International Journal of Rock Mechanics, Mining Sciences, & Geomechanics Abstracts*. 30: 381-394.

Johnson, J.C., Pariseau, W.G., Scott, D.F., and Jenkins, F.M. (1993) *In situ* stress measurements near the Ross pillar, Homestake Mine, South Dakota. *United States Department of the Interior Report of Investigations.* RI 9446: 1-21.

Kramer, D. (2011) Funding for NSF underground laboratory is rejected. *Physics Today*. 21.

Kulatilake, P.H.S.W., He, W., Um, J., and Wang, H. (1997) A physical model study of jointed rock mass strength under uniaxial compressive loading. *International Journal of Rock Mechanics & Mining Sciences*. 34: Paper No. 165.

Kulatilake, P.H.S.W., Wang, S., and Stephansson, O. (1993) Effect of finite size joints on the deformability of jointed rock in three dimensions. *Internal Journal of Rock Mechanics, Mining Sciences, & Geomechanics Abstracts*. 30: 479-501.

Li, L. and Cornet, F.H. (2004) Three dimensional consideration of flat jack tests. *International Journal of Rock Mechanics & Mining Sciences*. 41: 1-6.

Lisenbee, A.L. and DeWitt, R. (1993) Laramide evolution of the Black Hills Uplift. *Geological Survey of Wyoming Memoir*.

Littlejohn, S. (1993) Overview of rock anchorages In: *Comprehensive Rock Engineering: Principles, Practice, and Projects.* Pergamon Press. p. 413-450.

Nabelek, P.I., Sirbescu, M., and Liu, M. (1999) Petrogenesis and tectonic context of the Harney Peak Granite, Black Hills, South Dakota. *Rocky Mountain Geology*. 34: 165-181.

Nye, J.F. (1957) *Physical Properties of Crystals.* Clarendon Press: Oxford. 329 pp.

Olsson, M. and Bergqvist, I. (1997) Joint formation during detonation in multiple blast holes: Summary report from test period 1993-1996. *SveBeFo Report 32*. In Swedish.

Palmström, A. and Singh, R. (2001) The deformation modulus of rock masses – comparisons between in situ tests and indirect measurements. *Tunneling and Underground Space Technology*. 16: 115-131.

Pariseau, W. (1985) Research Study on Pillar Design for Vertical Crater Retreat (VCR) Mining. *Bureau of Mines Contract Report J0215043, Oct*.

Pariseau, W., Duan, F., and Schmuck, C.S. (1987) Stability Analysis of the VCR Stope at the Homestake Mine. *Gold Mining*. 87: 199-213.

Pariseau, W. G., Johnson, J.C., McDonald, M.M., and Poad, M.E. (1995) Rock mechanics study of shaft stability and pillar mining, Homestake Mine, Lead, SD: 2. Mine measurements and confirmation of premining results. *United States Department of the Interior Report of Investigations*. RI 9576: 1-13.

Peila, D. (1994) A theoretical study of reinforcement influence on the stability of a tunnel face. *Geotechnical and Geological Engineering.* 12: 145-168.

Ribacchi, R. (1988) Rock mass deformability *in situ* tests, their interpretation and typical results in Italy. *In: Sahurai (ed.) Proceedings of the Second International Symposium on Field Measurements in Geomechanics. Balkema: Rotterdam.*

Scott, D.F., Girard, J.M., Williams, T.J., and Denton, D.K. (1998) Comparison of seismic tomography, strain relief, and ultrasonic velocity measurements to evaluate stress in an underground pillar. *NIOSH*. 7 pp.

Serafim, J.L. and Pereira, J.P. (1983) Consideration of the geomechanical classification of Bieniawski. *Proceedings of the International Symposium on Engineering Geology and Underground Construction, Lisbon*. 1: 33-44.

Sharma, V.M., Singh, R.B., and Chaudhary, R.K. (1989) Comparison of different techniques and interpretation of the deformation modulus of rock mass *Proceedings of the Indian Geotechnical Conference ŽIGC., Visakhapatnam*. p. 439.

Signer, S.J. and Sunderman, C. (2003) New tools for roof support evaluation and design. *In Proceedings of the 22nd International Conference on Ground Control in Mining, Morgantown, August 5-7*. 5 pp.

Singh, R. (2011) Deformability of rock mass and a comparison between plate jacking and Goodman jack tests. *International Journal of Rock Mechanics & Mining Sciences*. 48: 1208-1214.

Singh, R. and Bhasin, R. (1996) Q-system and deformability of rock mass. *Proceedings of the Conference on Recent Advances in Tunnelling Technology, New Delhi*. p. 57.

Singh, R. and Rajvansi, U.S. (1996) Effect of excavation on modulus of deformation. *Proceedings of the Conference on Recent Advances in Tunnelling Technology, New Delhi*, pp. 57-67.

Tesarik, D., Johnson, J., Zipf, Jr., K., and Lande, K. (2002) Initial Stability Study of Large Openings for the National Underground Science Laboratory at the Homestake Mine, Lead, SD. *Proceedings of the 5th North American Rock Mechanics Symposium and the 17th Tunnelling Association of Canada Conference: NARMS-TAC 2002, Hammah et al. (eds) Toronto, Ontario, Canada, 7-10 July 2002*. pp.157-163

Volger, U.W., Deffur, R.D., and Bieniawski, Z.T. (1977) CSIR large flat jack equipment for determining rock mass deformability. *Exploration for Rock Engineering*. 2: 105-111.

Table 4.1: Deformation modulus (E_m) results for 89 kN point-loading test

FROSTS	Depth (m)	Stress (MPa)	Strain (με) Loading Cycle 1	Loading Cycle 2	Loading Cycle 3	Loading Cycle 4	Average	E_m (GPa)
Sensor A	0.62	0.024	2	2	2	2	2.00	12.1
Sensor B	0.92	0.023	1	1.5	1.5	1.5	1.38	16.5
Sensor C	1.23	0.018	0.5	1	1	1	0.88	21.2
Sensor D	1.53	0.013	0.25	0.5	0.5	0.5	0.44	31.7
Sensor E	1.84	0.010	0	0	0.5	0	0	-
Sensor F	2.14	0.008	0	0	0.25	0	0	-
OS3600	0.50	0.016	2	2	2	2	2	8.1

Table 4.2: Deformation modulus (E_m) results for 890 kN point-loading test

Loading location 1			Strain (με)					
FROSTS	Depth (m)	Stress (MPa)	Loading Cycle 1	Loading Cycle 2	Loading Cycle 3	Loading Cycle 4	Average	E_m (GPa)
Sensor A	0.62	0.218	9	6	8	8	7.8	28.7
Sensor B	0.92	0.203	4.5	5	6	6	5.4	37.5
Sensor C	1.23	0.159	3	3	3	3.5	3.3	49.1
Sensor D	1.53	0.119	2	2	2	2	2.0	59.5
Sensor E	1.84	0.091	1.5	1.5	1.5	1.5	1.5	60.8
Sensor F	2.14	0.071	1.5	1	1	1	1.1	65.1
OS3600	0.50	0.016	0	0	0	0	-	-

Loading location 2			Strain (με)				
FROSTS	Depth (m)	Stress (MPa)	Loading Cycle 1	Loading Cycle 2	Loading Cycle 3	Average	Em (GPa)
Sensor A	0.62	0.035	0	0	0	0	-
Sensor B	0.92	0.033	0	0	0	0	-
Sensor C	1.23	0.026	0	0	0	0	-
Sensor D	1.53	0.019	0	0	0	0	-
Sensor E	1.84	0.015	0	0	0	0	-
Sensor F	2.14	0.012	0	0	0	0	-
OS3600	0.50	0.571	12	13	13	12.7	45.2

Table 4.3: Moduli from laboratory mechanical testing on the Poorman Formation

Sample	Core Orientation	Young's modulus gage #1 (GPa)	Young's modulus gage #2 (GPa)	Poisson's ratio gage #1	Poisson's ratio gage #2
PM1	Perpendicular	35.4	32.9	0.34	0.24
PM3	Perpendicular	52.7	47.5	0.17	0.16
PM5	Perpendicular	44.8	47.4	0.26	0.23
Average		43.5 GPa		0.23	
PM2	Parallel	56.7	52.7	0.16	0.14
PM4	Parallel	53.5	40.0	0.14	0.19
PM6	Parallel	74.3	66.3	0.18	0.17
Average		57.3 GPa		0.16	

Table 4.4: Comparison of *in situ* modulus of deformation results and E_m from Hoek and Diederichs (2006) as a function of Disturbance Factor

Disturbance Factor (D)*	E_m (GPa) Hoek and Diederichs (2006)**	*In situ* E_m (GPa) 890 kN loading experiment	Depth (m)
0.5	25.2		
0.44	28.7	28.7	0.62
0.4	31.1		
0.3	37.7	37.5	0.92
0.2	45.0		
		50.8	LAB
0.1	52.9	49.1	1.23
0	61.2	59.5	1.53
		60.8	1.84
		65.1	2.14

* From Hoek et al. (2002)

** From Equation 2 (Hoek and Diederichs, 2006)

Table 4.5: Vertical regional stress for each strain gage along the FROSTS embedded in the roof of the experiment alcove

Sensor	Depth (m)	σ_v (MPa)
A	0.62	0
B	0.92	0
C	1.23	6.31
D	1.53	10.2
E	1.84	12.4
F	2.14	13.7

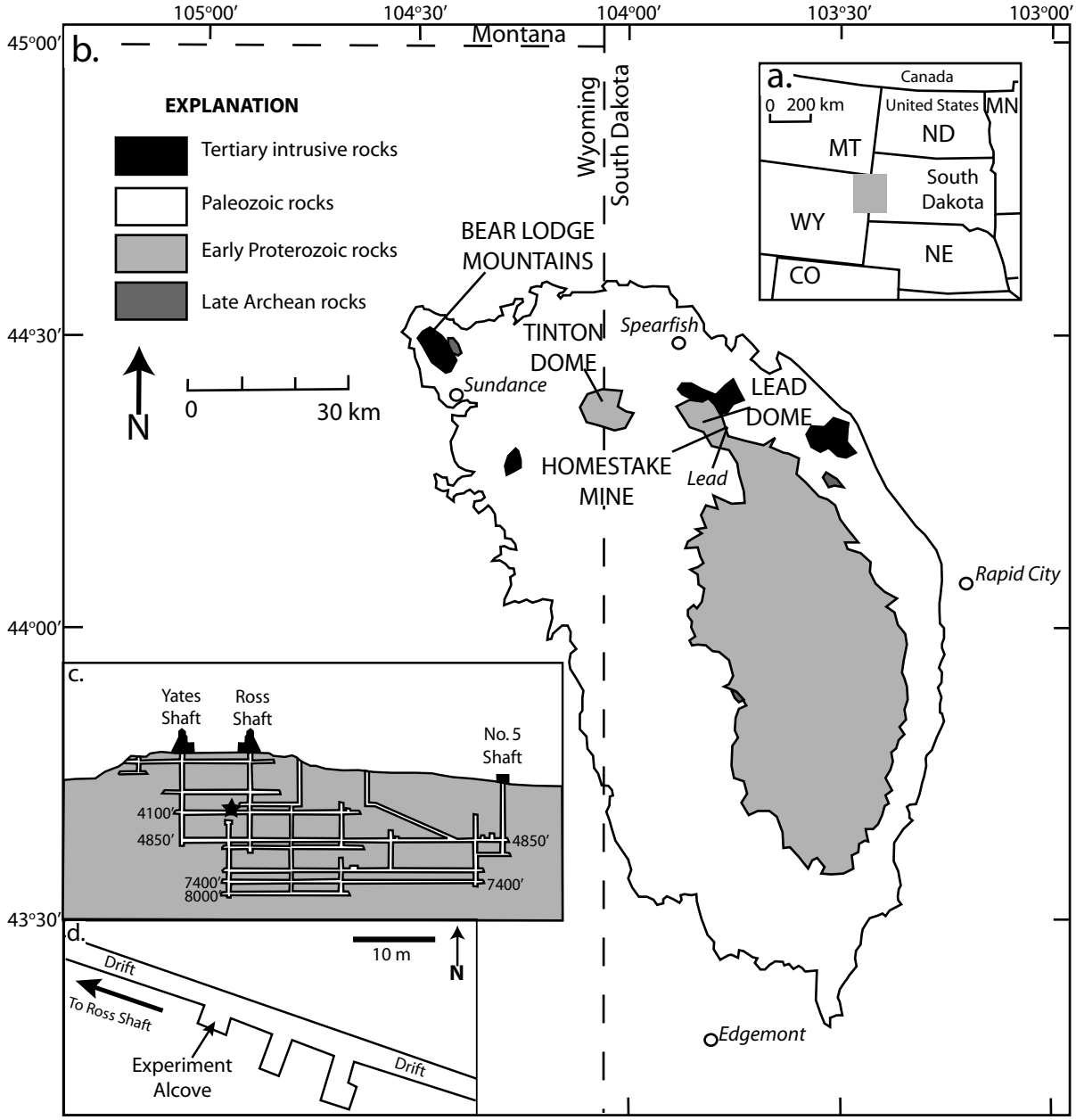

Figure 4.1. Location of SURF at the former Homestake gold mine in Lead, South Dakota. a.) Gray box shows location of the Black Hills; b.) Simplified geologic map of the Black Hills Uplift. SURF is located in the Lead Dome of the northern Black Hills. Modified from Pariseau (1995); c.) Schematic cross section of SURF showing major science levels. Black star denotes approximate experiment location; d.) Map view of experiment alcove on the 1250 m (4100 ft.) level.

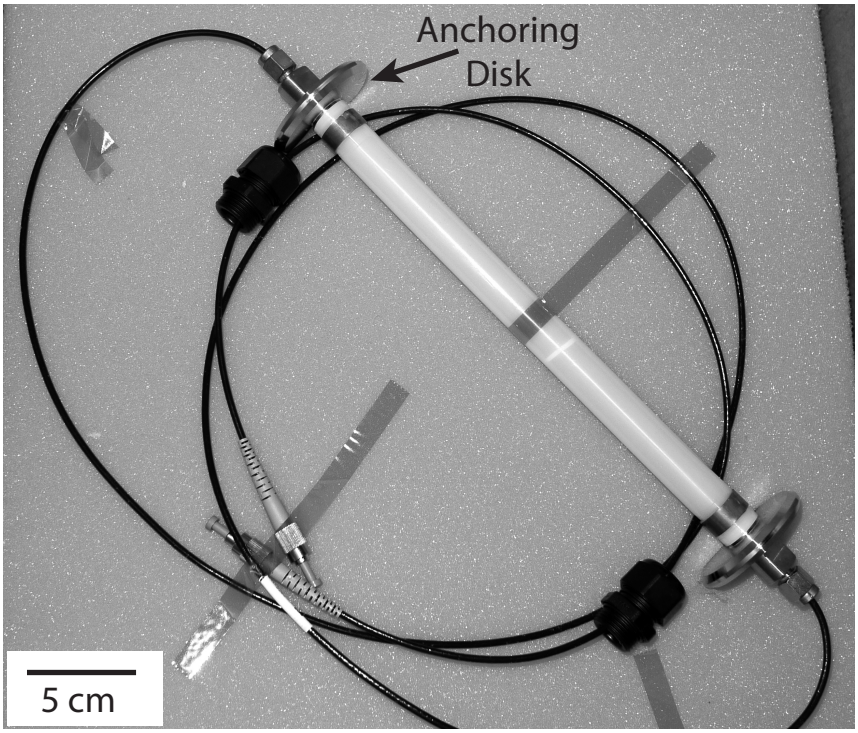

Figure 4.2. Photograph of OS3600 sensor embedded in the ceiling of the alcove. Gage length is 25.4 cm.

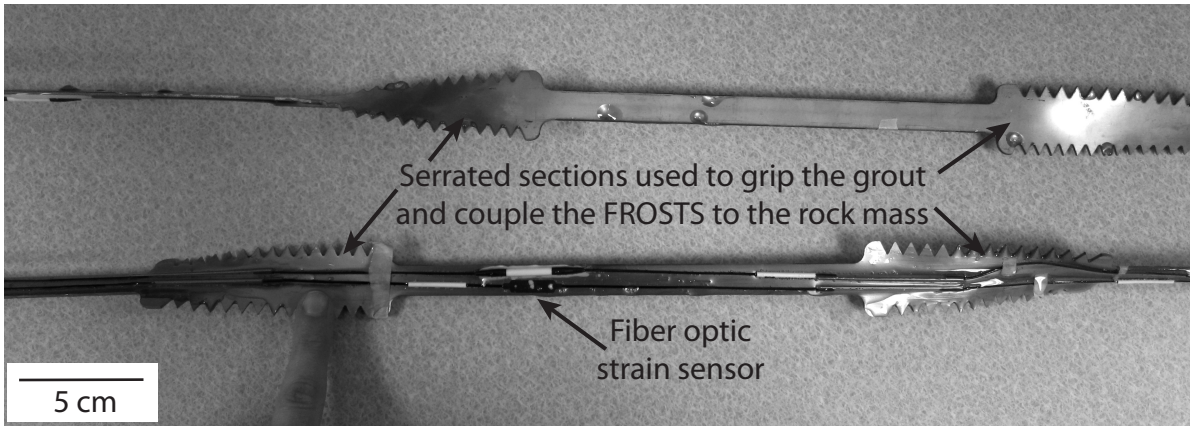

Figure 4.3. Photograph of a section of FROSTS showing fiber-optic strain gages and thicker serrated sections of the strip that grip the grout in the borehole and separate the FROSTS into six independent sections for strain measurement.

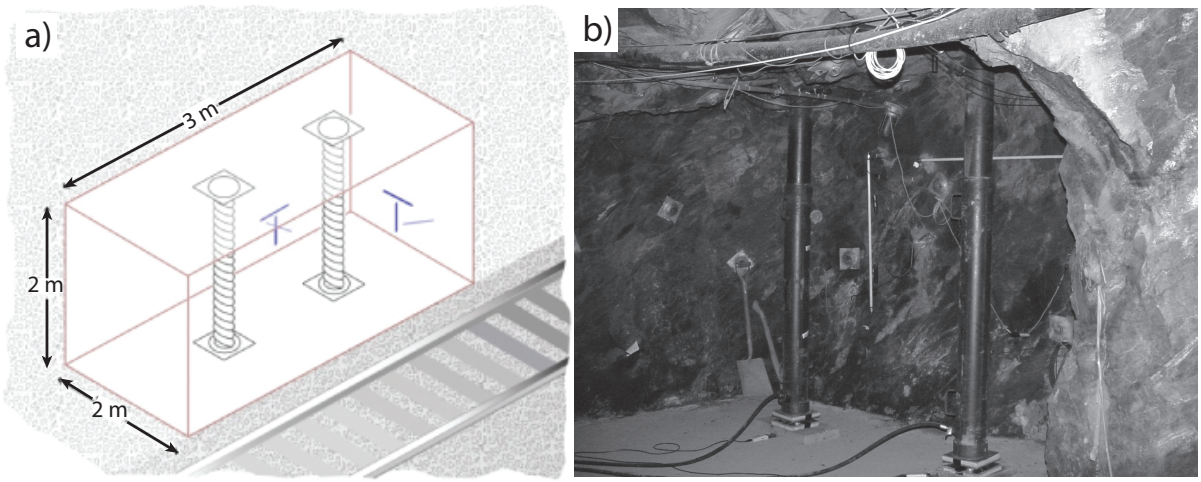

Figure 4.4. Set up for 89 kN (10 ton) point-loading test. a) Sketch of experiment alcove showing dimensions and schematic load locations. b) Photograph of 89 kN point-loading test on Poorman formation on the 1250 m (4100 ft.) level of SURF.

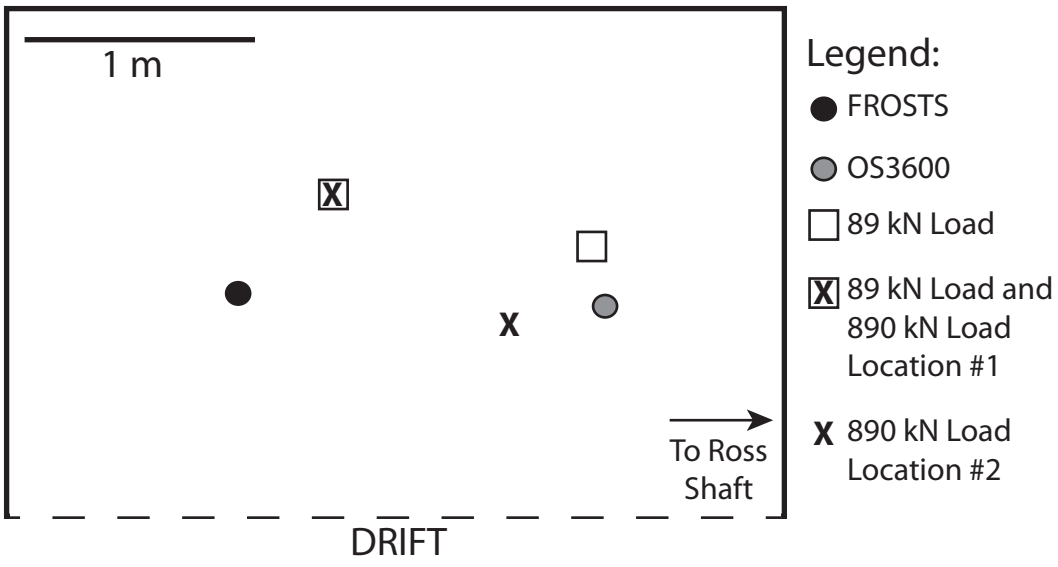

Figure 4.5. Map of experiment alcove showing location of FROSTS, embedded OS3600 sensors, and loads applied during the 89 kN and 890 kN point-loading tests.

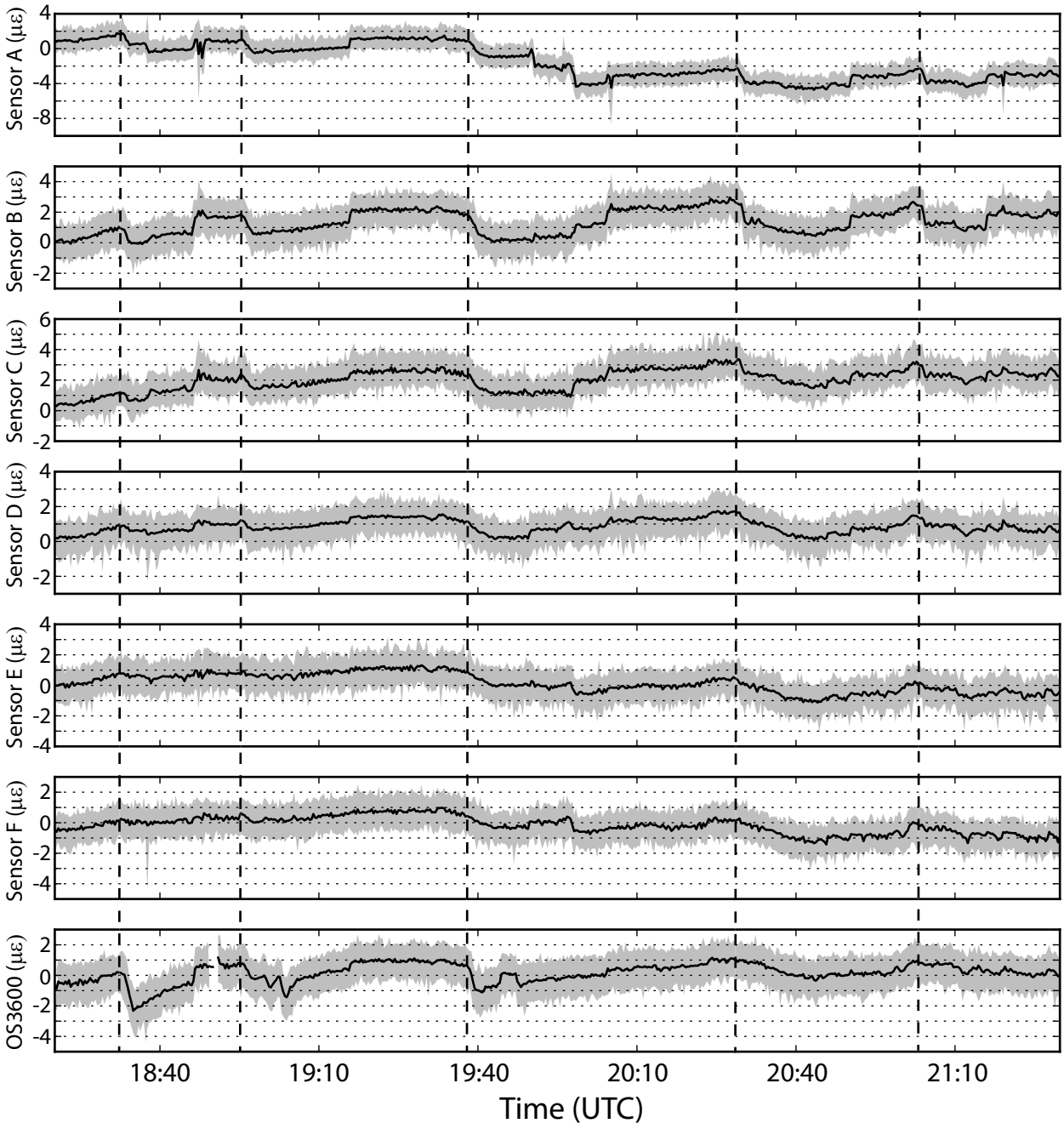

Figure 4.6. Strain data from 89 kN point-loading test. Loads were applied at 18:30, 18:55, 19:40, 20:30, and 21:05 (vertical dashed black lines). Shortening is negative and tension is positive. For the FROSTS, sensor A is closest to the surface (0.62 m) and sensor F is deepest in the rock mass (2.14 m). The OS3600 is embedded in the ceiling of the alcove. See Fig. 4.5 for FROSTS, OS3600, and load locations.

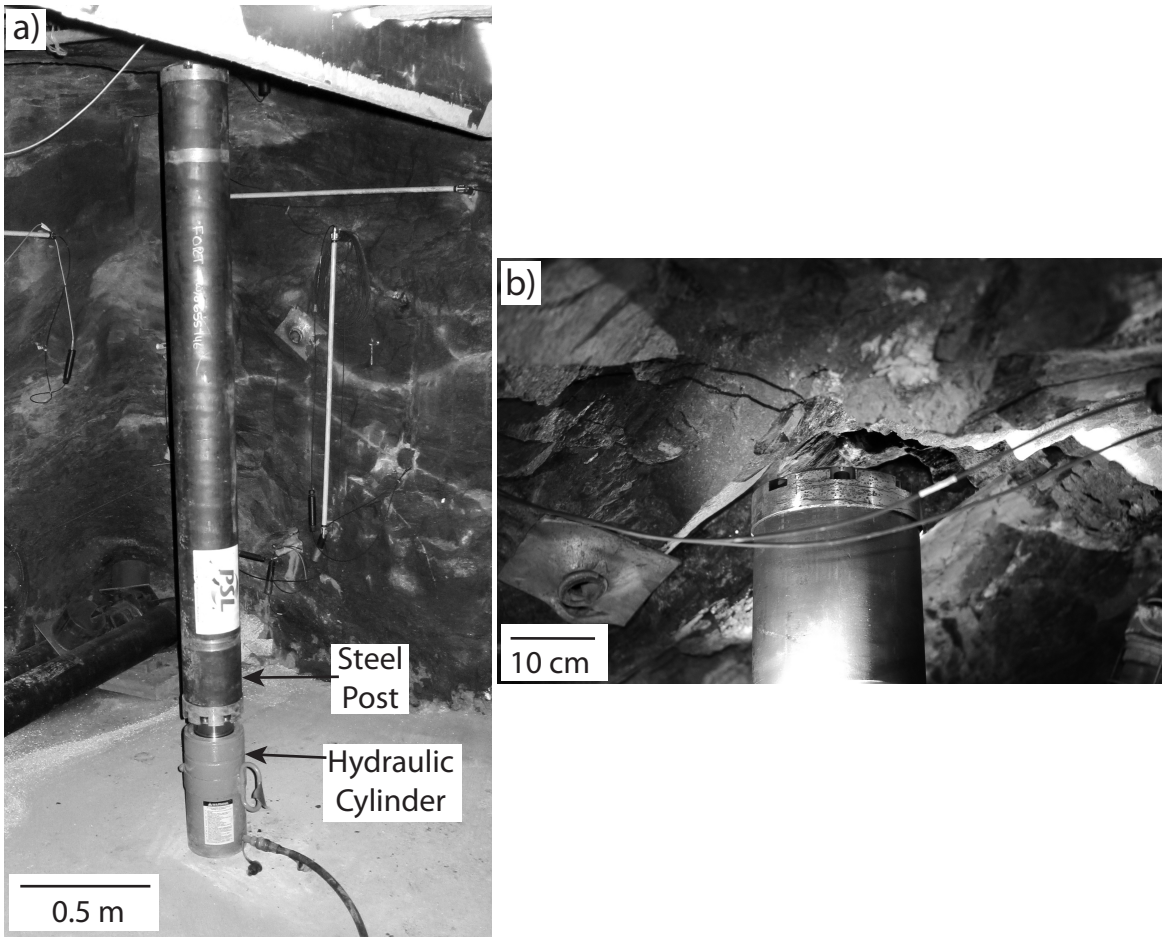

Figure 4.7. a) Photograph of hydraulic cylinder and steel post set up for 890 kN point-loading test. b) Close-up photograph of rounded head of steel post where it contacted the rock mass for the 890 kN loading test location #1.

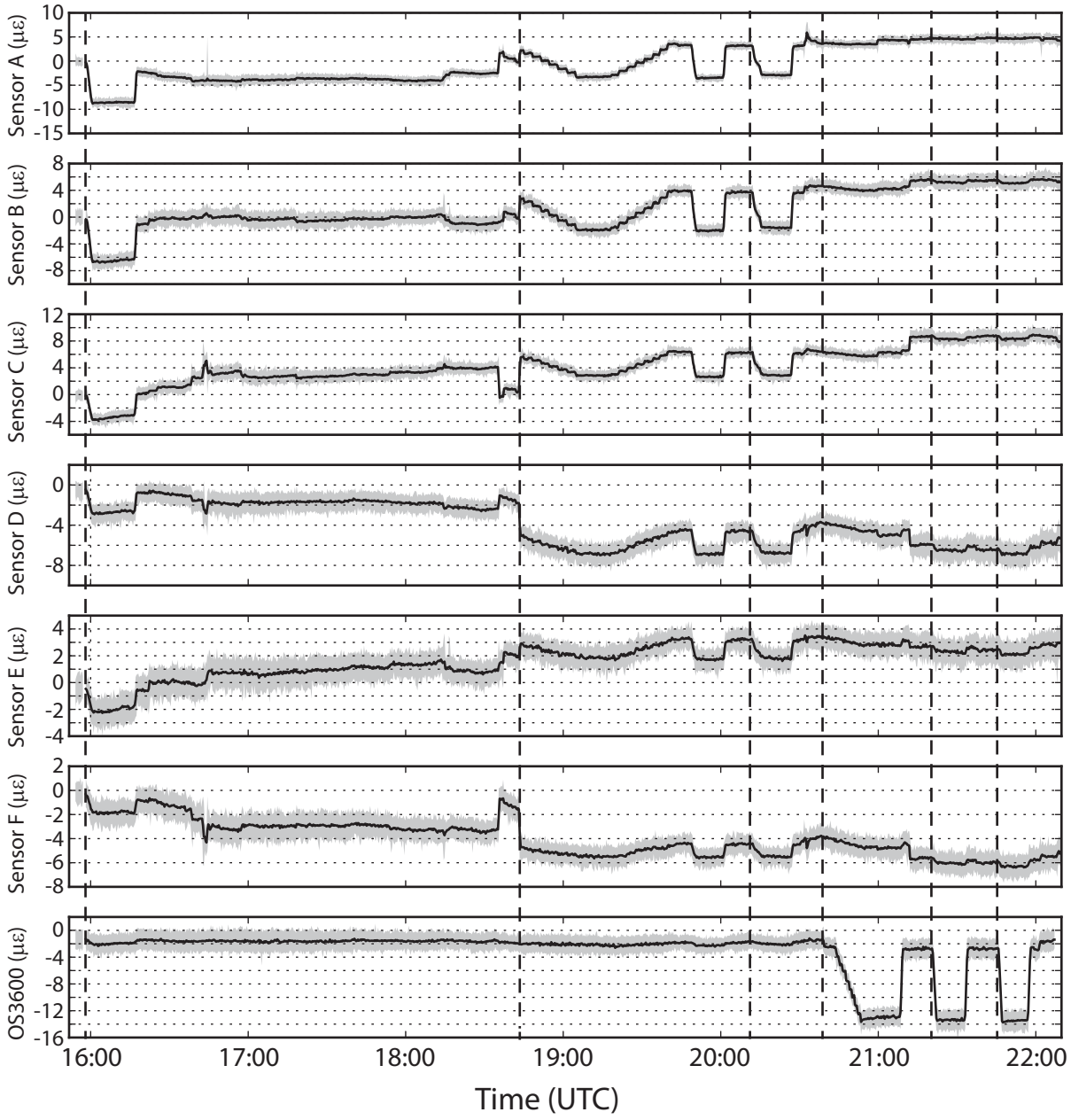

Figure 4.8. Strain data from 890 kN point-loading test. Loads were applied at location #1 at16:00, 18:40, 19:40, 20:20 (vertical black dashed lines) and at location #2 at 20:40, 21: 20, and 21:45 (vertical black dashed lines). Shortening is negative and elongation is positive. For the FROSTS, sensor A is closest to the surface (0.62 m) and sensor F is deepest in the rock mass (2.14 m). The OS3600 is embedded in the ceiling of the alcove. See Fig. 4.5 for FROSTS, OS3600, and load locations.

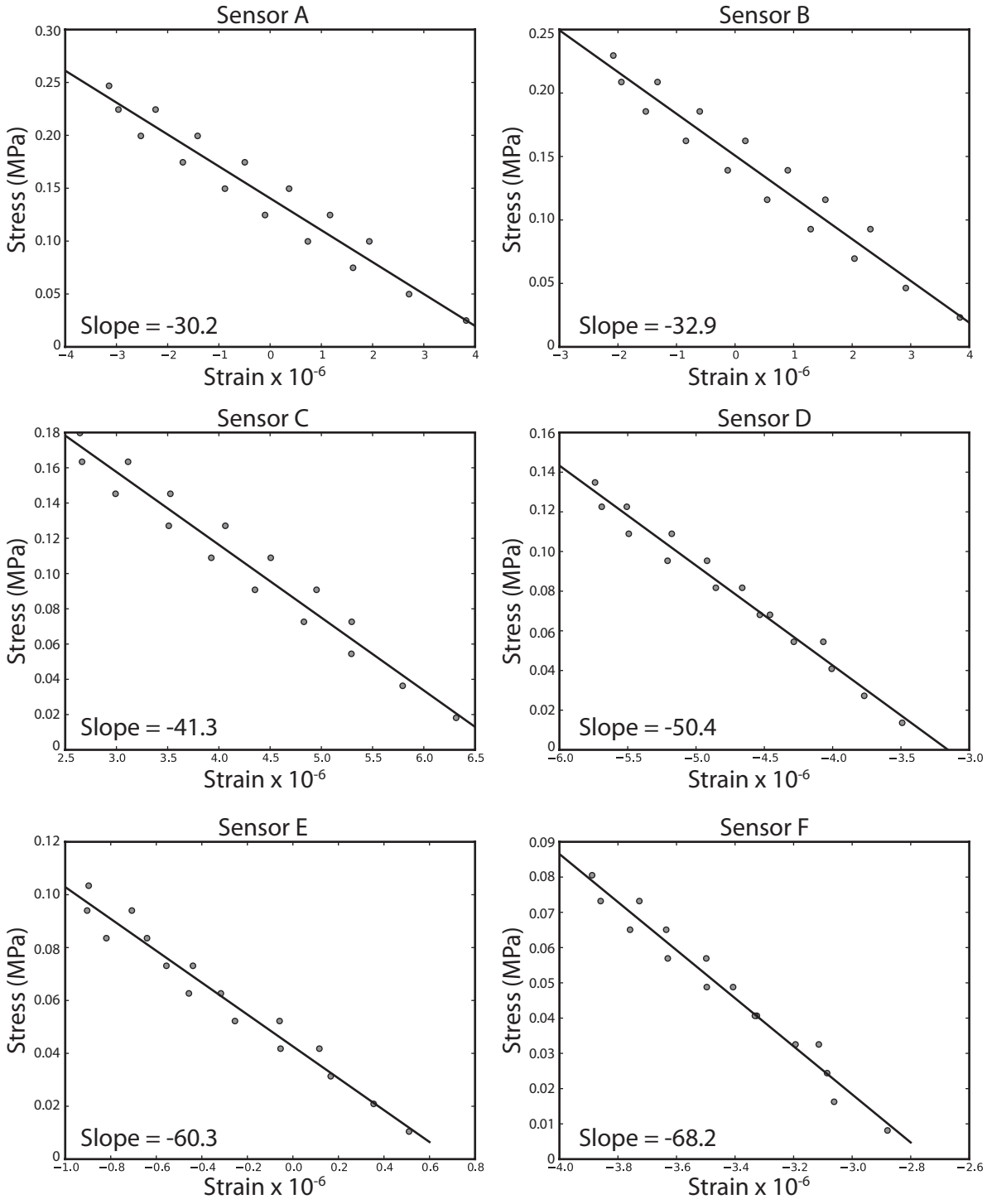

Figure 4.9. Loading and unloading stress-strain curves for the six FBG sensors on the FROSTS embedded in the roof of the alcove during the 18:40 890 kN point-loading test (Fig. 4.8). Sensor A is the closest to the surface and sensor F is deepest in the rock mass.

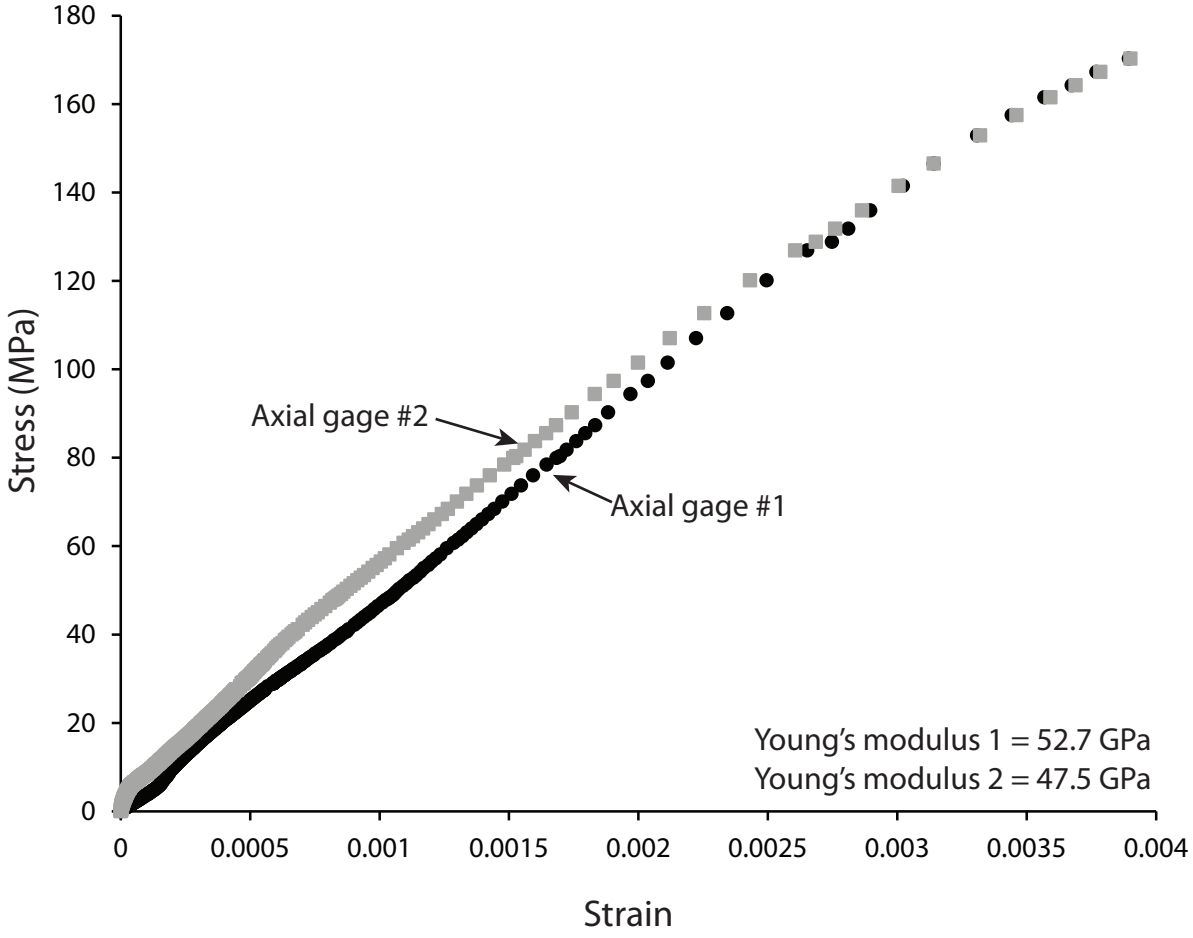

Figure 4.10. Representative stress-strain curve for two axial gages on Poorman formation during laboratory testing. Young's modulus is noted on graph.

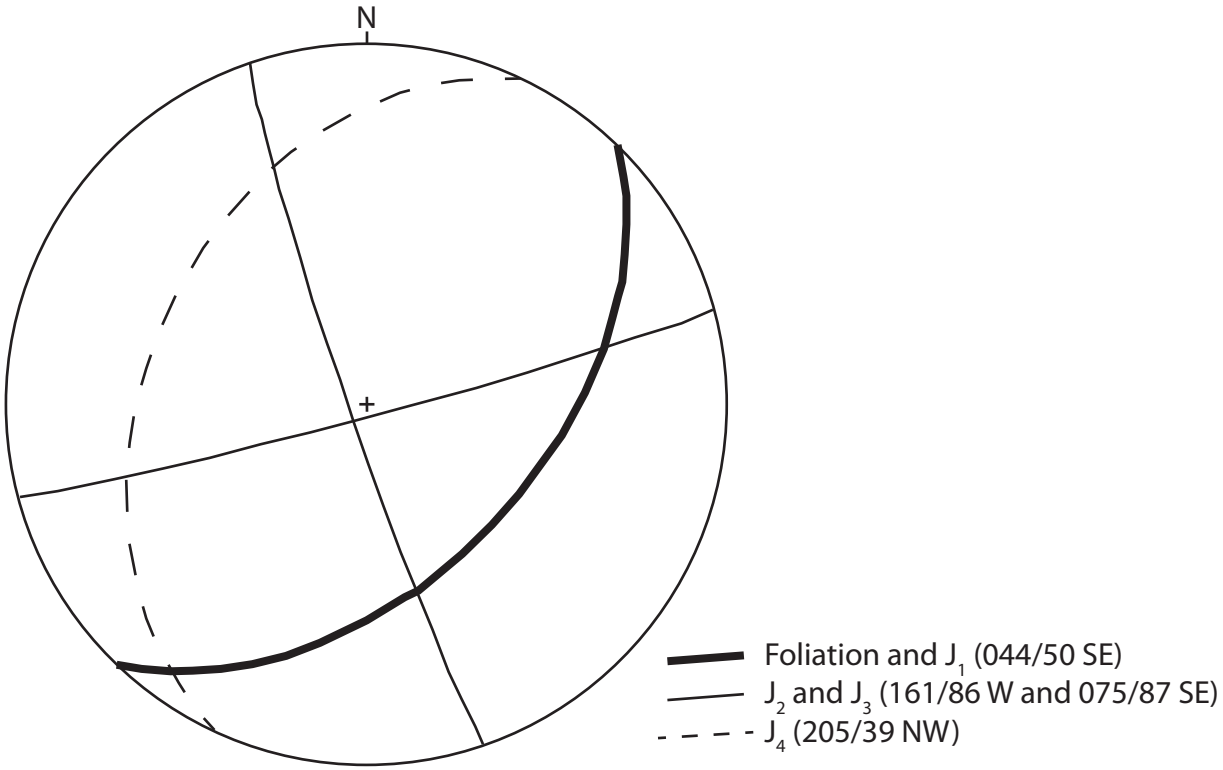

Figure 4.11. Equal-area, lower-hemisphere plot of traces of joint sets in the Poorman formation in the experiment alcove. Foliation is the most prominent joint set (dark black line), J_2 and J_3, the next most prominent joint sets, are oriented sub-vertical (light black lines), and J_4 is the least prominent joint set (dashed line).

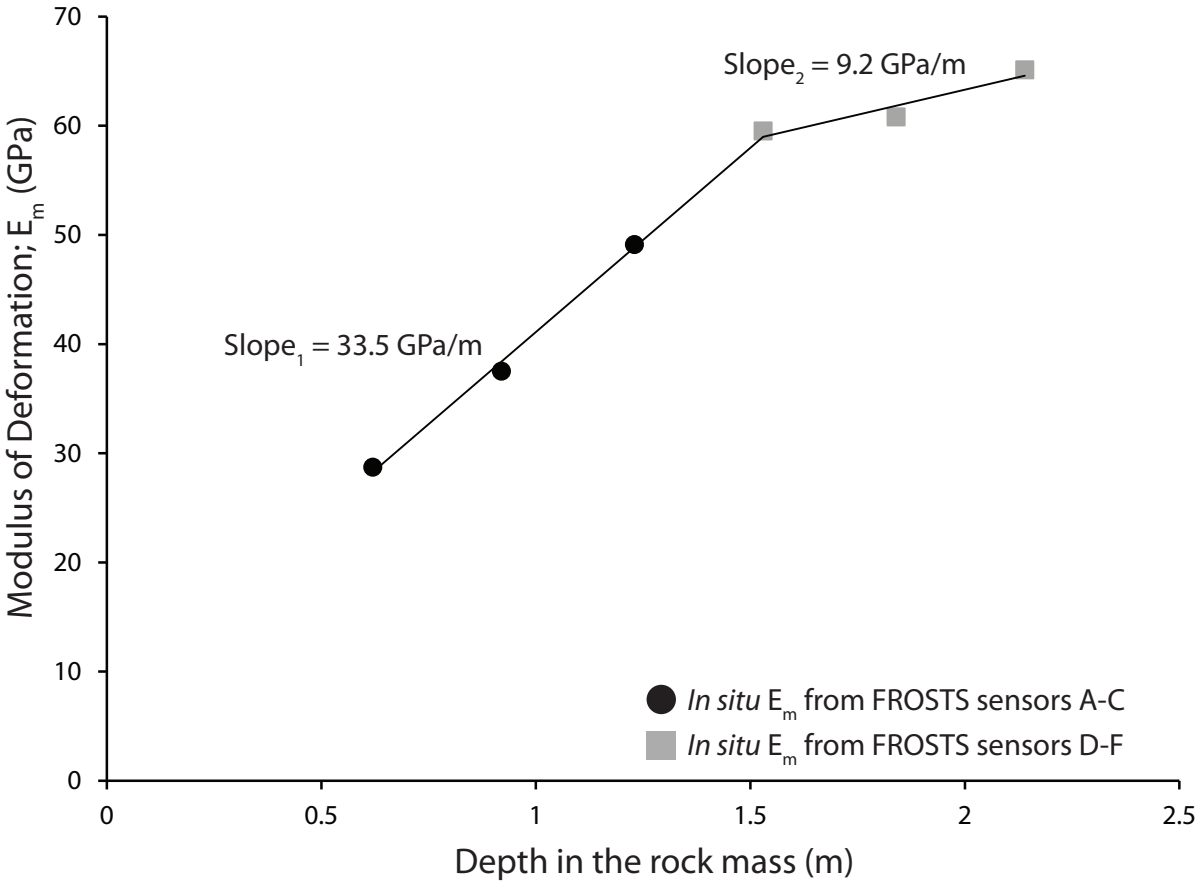

Figure 4.12. Plots of modulus of deformation (E_m) and depth in intact rock mass as measured during the 890 kN point-loading test. The data breaks into two populations. 1) Sensors A-C (black dots), which measured an E_m more compliant than laboratory Young's modulus and and have a steep slope. 2) Sensors D-F (gray squares), which measure an E_m stiffer than the laboratory Young' modulus and higher than the empirical results for a disturbance factor (D) of 0 (Hoek and Diederichs, 2006), and have a shallow slope.

Chapter 5: Conclusions

5.1 Conclusions

In chapters 2 and 3, I have established fiber-optic strain gages and temperature sensors as a viable method for monitoring real-time *in situ* strain in rock masses. I have developed the first Fiber Bragg Grating (FBG) sensor attachment methods for rock mass monitoring and tested their validity and accuracy for strain measurement. Because strain and temperature measurements are coupled in FBG sensors, embedded sensors are preferable to surface-mounted sensors, which are susceptible to bias from ambient temperature changes. Thus, I have also developed an embedded multipoint borehole extensometer instrumented with six fiber-optic strain gages and temperature sensors. These Fiber-optically Instrumented Rock Strain and Temperature Strips (FROSTS) are pretensioned prior to installation to allow them to measure the broadest possible range of both shortening and elongation. FROSTS provide an accurate and detailed record of *in situ* strain and temperature in intact rock masses and are a valuable new tool for the structural health monitoring of underground spaces.

In chapter 4, the results of an 890 kN (100 ton) field point-loading test quantify how the modulus of deformation increases with depth in an intact rock mass. This gradient of increasing stiffness from the surface to depth is a result of the excavation of the underground opening, and is an important illustration of the effect of scale on rock properties. My research has shown that no single measurement (laboratory, empirical estimate, or *in situ* experiment) fully characterizes a rock mass on the m^3-scale. Thus, it is important to use a multipoint borehole extensometer during *in situ* experiments to measure how the rock properties change with depth in a rock mass. Also, the results of the 89 kN (10 ton) point-loading test

significantly underestimate rock stiffness, thus, in *in situ* rock deformability experiments, it is important to use a sufficiently large load to accurately measure mechanical properties.

5.2 Implications

The development and validation of fiber-optic strain and temperature sensors for geotechnical applications, and specifically FROSTS, has created new tools for the structural health monitoring of underground openings. Fiber-optic sensors have many advantages over traditional monitoring techniques. In general, FBG sensors are accurate and sensitive enough to measure small strains that may be a precursor to rock mass failure (Bhalla et al., 2005). Because FBG strain gages must be deployed with temperature compensation gages, fiber-optic sensor arrays also provide a thermal profile of the rock mass, which can be useful to determine *in situ* thermal properties of the rock mass. Because fiber-optic sensors are stable over long time scales and do not require calibration, they are suitable for long-term structural health monitoring (Glisic and Inaudi, 2007). FBG sensors also have streamlined data collection and the ability to monitor data remotely, which is preferable to the campaign-style measurements of many other rock monitoring techniques (Franklin, 1977).

My attachment methods allow the FBG sensors to couple directly to or be embedded in the rock mass, which provide more accurate readings than convergence monitoring or extensometers installed on the rock surface (Milner, 1969). Because FROSTS are more compliant than the rock mass, they act as a passive element in the system and accurately measure *in situ* strain, unlike instrumented rock bolts, which underestimate deformation because they are stiffer than the rock mass (Farmer, 1975; Signer and Sunderman, 2003). Because the FROSTS are pretensioned prior to installation, they are the only *in situ*

monitoring technique that can measure shortening, which can record the differential loading of discrete fracture-bounded blocks or squeezing in the rock mass resulting in convergence surrounding an underground opening (Seilars, 1968; Franklin, 1977).

The *in situ* modulus of deformation measurements not only add data to a relatively sparse dataset (see Gokceoglu et al., 2003 for a recent review), but they also improve the current understanding of how and why deformation moduli vary from the cm^3 to m^3-scale. It is well documented that the damaged zone surrounding an underground opening significantly effects rock mass stiffness (Vovk et al., 1974; Emsley et al., 1997; Palmström and Singh, 2001); however, previous work has not quantified the extent of the damaged zone. My work quantifies both the depth of the damaged zone, and how the stiffness of the rock mass increases from the surface to the undisturbed rock mass. This stiffness gradient will impact how underground spaces are constructed and how ground control is approached, which will improve the safety and longevity of these spaces.

5.3 Future work

In my dissertation, I have developed and validated installation techniques for fiber-optic strain gages. The next step for *in situ* strain monitoring with fiber-optic sensors is designing effective monitoring arrays. How should these tools be used to monitor geological features? The FROSTS is segmented into six sections along its length. A single FROSTS could be installed across a feature, such as a fault, joint set, lithologic contact, etc., and strain at different sensor locations along the FROSTS could be used to monitor relative movement in the system. Also, because the fiber-optic sensors used in my dissertation measure one-

dimensional strain, it will be important to design sensor arrays that can measure strain in three dimensions to fully understand the deformation of geologic features.

Fiber-optic strain gage arrays can also be used to examine elastic strain partitioning during deformation in a lithologically heterogeneous system. Experimental results on constituent members of a heterogeneous system are often used in theoretical approaches to describe the mechanical properties of composite systems (e.g. Jordan, 1998; Ji and Zhao, 1994). The most widely used methods assume that either the average stress or the average strain is the same in each phase in the system (e.g. Hashin and Shtrikman, 1962; Hill, 1963). This works best when the material properties of the different elements in the composite are similar, but breaks down when the composite system has very disparate elements (Willis, 1981). By instrumenting adjacent rock types and litholoigc contacts with fiber-optic strain gages, and performing point-loading tests, strain partitioning in a lithologically heterogeneous system could be analyzed on the 10s of meter scale. This *in situ* measurement of strain partitioning is important to accurately project laboratory measurements of mechanical properties from the cm^3-scale to m^3 and 10s of meter-scales.

In order to gain a better understanding of the damaged zone surrounding underground excavations and rock mass deformability, similar *in situ* deformability tests should be performed in different rock types. Lithology controls not only rock mass stiffness (Hoek and Brown, 1997), but also deformation mechanisms in a rock mass (Agharazi et al., 2012). With a bigger data set, it could be possible to develop a new method for the empirical estimation of rock mass moduli (e.g. Bieniawski, 1973; Hoek and Diederichs, 2006) using the results of *in situ* tests that determine a stiffness gradient in the rock mass. A new geotechnical

classification system based on these types of *in situ* measurements could quantitatively predict a typical damaged zone in different rock types.

In order to further examine the effect of scale on rock properties, it would be useful to move from the m^3-scale up to the km^3- scale. By coupling local strain and rock properties measurements, such as those in my dissertation, with large-scale deformation monitoring, with GPS or InSAR measurements, it would be possible to look at rock mass deformability on the km^3-scale or larger.

References

Agharazi, A., Tannant, D.D., and Martin, C.D. (2012) Characterizing rock mass deformation mechanisms during plate loading tests at the Bakhtiary dam project. *International Journal of Rock Mechanics & Mining Sciences*. 49: 1-11.

Bhalla, S., Yang, Y.W., Zhao, J., and Soh, C.K. (2005) Structural health monitoring of underground facilities – Technological issues and challenges. *Tunnelling and Underground Space Technology*. 20:487-500.

Bieniawski, Z.T. (1973) Engineering Classification of rock masses. *Transactions of the Society of African Institute for Civil Engineers*. 15: 335-344.

Emsley, S., Olsson, O., Steinberg, L., Alheid, H.J., and Falls, S. (1997) ZEDEX – A study of damage and disturbance from tunnel excavation by blasting and tunnel boring. *SKB Technical Report.* 97-30: 1-198.

Farmer, I.W. (1975) Stress distribution along a resin grouted anchor. *International Journal of Rock Mechanics, Mining Sciences & Geomechanics*. 12: 347-351.

Franklin, J.A. (1977) The monitoring of structures in rock. *International Journal of Rock Mechanics Mining Sciences & Geomechics Abstracts*. 14:163-192.

Glisic, B. and Inaudi, D. (2007) *Fibre Optic Methods for Structural Health Monitoring.* 1st ed. Sussex: Chinchester. 276 pp.

Gokceoglu, C., Sonmez, H., and Kayabasi, A. (2003) Predicting the deformation moduli of rock masses. *International Journal of Rock Mechanics & Mining Sciences*. 40: 701-710.

Hashin, Z. and Shtrikman, S. (1962) A variational approach to the theory of the elastic behavior of polycrystals. *Journal of the Mechanics & Physics of Solids.* 10: 343-352.

Hill, R. (1963) Elastic properties of reinforced solids: some theoretical principles. *Journal of the Mechanics & Physics of Solids.* 11: 357-372.

Hoek, E. and Brown, E.T. (1997) Practical estimates of rock mass strength. *International Journal of Rock Mechanics & Mining Sciences*. 34: 1165-1186.

Hoek, E. and Diederichs, M.S. (2006) Empirical Estimation of rock mass modulus. *International Journal of Rock Mechanics & Mining Sciences*. 43: 203-215.

Ji, S. and Zhao, P. (1994) Layered rheological structure of subducting oceanic lithosphere. *Earth andPlanetary Science Letters*. 124: 75-94.

Jordan, P.G. (1988) The rheology of polymineralic rocks – an approach. *Geologische Rundschau.* 77: 285-294.

Milner, R.M. (1969) Accuracy of measurements with steel tapes. *Building Research*. Station. CP51/69.

Palmström, A. and Singh, R. (2001) The deformation modulus of rock masses – comparisons between in situ tests and indirect measurements. *Tunneling and Underground Space Technology*. 16: 115-131.

Seilars J. B. (1968) Rock instrumentation in tunnels. *ASCE Water Power,* 1-7.

Signer, S.J. and Sunderman, C. (2003) New tools for roof support evaluation and design. *In Proceedings of the 22nd International Conference on Ground Control in Mining, Morgantown, August 5-7*.

Vovk, A.A., Mikhalyuk, A.V., and Belinski, I.V. (1974) Development of fracture zones in rocks during camouflet blasting. *Soviet Mining Science*. 9: 383-387.

Willis, J.R. (1981) Variational and related methods for the overall properties of composites. *Advanced Applied Mechanics*. 21: 1-78.